TECHNISCHE UNIVERSITÄT MÜNCHEN

Fakultät für Informatik
I–16 / Computer Aided Medical Procedures & Augmented Reality

Challenges and opportunities in PET/MR image reconstruction

Dipl.-Math. Rebekka Löb

Vollständiger Abdruck der von der Fakultät für Informatik der Technischen Universität München zur Erlangung des akademischen Grades eines

Doktors der Naturwissenschaften (Dr. rer. nat.)

genehmigten Dissertation.

Vorsitzender:	Prof. Dr.–Ing. Darius Burschka
Prüfer der Dissertation:	
1.	Prof. Dr. Nassir Navab
2.	apl. Prof. Dr. Sibylle Ziegler
3.	Prof. Dr. Julia Herzen

Die Dissertation wurde am 04.09.2019 bei der Technischen Universität München eingereicht und durch die Fakultät für Informatik am 01.03.2020 angenommen.

Für Johann und Friedrich.

Abstract

Technological advancements and innovations in healthcare play a major role in improving quality of life today. Especially multimodal imaging combining complementary data from different modalities has become indispensable. Combining the high-resolution capabilities of *magnetic resonance imaging (MRI)*, which compared to *computed tomography (CT)* does not expose patients to ionizing radiation, with the functional, yet resolution-limited capabilities of molecular imaging such as *positron emission tomography (PET)* is a promising approach.

Only recently, integrated devices such as the Biograph mMR PET/MR scanner (Siemens) have become available. These integrated devices deliver high-quality, simultaneously acquired data, which opens new opportunities in imaging. At the same time, these devices come with unique obstacles. We show how mathematical methods and algorithms can be used to address some of these challenges.

Positron range, i.e., the distance positrons travel before they annihilate and can be detected, is impairing PET resolution. It is known to be tissue dependent and affected by magnetic fields as used in MRI. We investigated positron range and its effect on imaging in the Biograph mMR for ^{82}Rb and ^{68}Ga using Monte-Carlo simulation. Annihilation events were concentrated in the direction of the scanner's 3 T magnetic field. This led to a significant loss in resolution in that direction and to misplacement artifacts at tissue boundaries (up to 24 % of activity was wrongly attributed to the denser tissue at a boundary). Therefore, a 3D reconstruction framework was extended to incorporate a novel, simulation-based correction kernel that leverages structural information from the MR scan. The novel method improved resolution by over 50 % and removed virtually all misplacement artifacts, with only 7 % of activity wrongly attributed.

Parametric imaging is an extension of PET that models physiological processes. It relies on pharmacokinetic analysis of dynamic PET imaging data to map the measured time activity curves to a set of model-specific parameters. Especially voxel-based parameter estimation is promising, but traditional indirect methods relying on independently reconstructed PET images suffer from high variance and bias. We developed a direct parametric reconstruction algorithm that leverages optimization transfer and can incorporate structural information from the MR image for regularization of activity or parametric images, or both simultaneously. The algorithm was evaluated on simulated [^{18}F]FDG data, for which the direct method reduced the total normalized root mean square error in K_1, k_2 and K_i images by 27 %, and by 45 % when structural information was added. Simultaneous regularization generally yielded significantly lower variance than activity regularization alone at comparable bias levels. High quality images from clinical [^{18}F]FET brain data could be derived that

showed 140 % increase in tumor contrast compared to the indirect method at comparable noise levels.

For the evaluations, a reconstruction framework was developed that supports the Biograph scanner, that has comprehensive means to prototype and analyze imaging algorithms, and that addresses the unique requirements of PET/MR.

Zusammenfassung

Technologischer Fortschritt auf dem Feld der Medizintechnik ist heutzutage ein wichtiger Faktor für die Verbesserung von Lebensqualität und Lebenserwartung. Vor allem multimodale Bildgebung, welche komplementäre Daten aus verschiedenen Quellen kombiniert, spielt dabei eine entscheidende Rolle. Die Kombination von hochauflösender *Magnetresonanztomographie (MRT)*, welche im Gegensatz zur *Computertomographie (CT)* Patienten nicht ionisierender Strahlung aussetzt, mit der funktionalen aber auflösungsbegrenzten molekularen Bildgebung, wie zum Beispiel der *Positronen-Emissions-Tomographie (PET)*, ist dabei besonders viel versprechend.

Erst seit kurzem existieren integrierte Geräte wie etwa der Biograph mMR PET/MRT Scanner (Siemens). Diese integrierten Geräte liefern qualitativ hochwertige und gleichzeitig aufgenommene Daten, was einerseits neue Möglichkeiten eröffnet, aber andererseits auch neue Herausforderungen mit sich bringt. Im Rahmen dieser Arbeit wird gezeigt, wie mathematische Methoden und Algorithmen entscheidend dazu beitragen, das Potential dieser neuen Geräte besser auszuschöpfen.

Die Distanz, welche Positronen im Gewebe zurücklegen bevor sie annihilieren und detektiert werden können, wird Positronenreichweite genannt. Sie führt bei der PET zu einer Verschlechterung der Auflösung. Es ist bekannt, dass dieser Effekt von Gewebe und auch von Magnetfeldern, wie sie in MR Tomographen vorzufinden sind, beeinflusst wird. Wir haben den Effekt der Positronenreichweite auf die Bildgebung mit dem Biograph mMR Scanner für ^{82}Rb und ^{68}Ga untersucht. Dabei zeigte sich, dass Annihilationsereignisse gehäuft entlang der Richtung des 3 T Magnetfelds des Scanners auftraten, was zu einer erheblichen Verschlechterung der Auflösung führte. Ausserdem traten Artefakte auf, welche bis zu 24 % der Aktivität fälschlicherweise im dichteren Gewebe darstellten. Daher wurde von uns ein Framework zur 3D-Rekonstruktion von PET Daten dahingehend erweitert, dass in einem neuartigen, simulationsbasierten Ansatz die Positronenreichweite mit Strukturinformation von der MRT rechnerisch korrigiert werden kann. Diese neuartige Methode verbesserte die Auflösung um mehr als 50 %, zeigte so gut wie keine Artefakte und lokalisierte nur 7 % der Aktivität fälschlich.

Parametrische Bildgebung ist eine Erweiterung der PET, welche physiologische Prozesse mittels pharmakokinetischer Analysis modelliert. Dabei werden dynamische PET Daten und die daraus resultierenden Aktivitätsverläufe auf modellspezifische Parameter abgebildet. Insbesondere voxel-basierte Parameterschätzungen sind diagnostisch vielversprechend, allerdings leiden herkömmliche, indirekte Verfahren unter systematischen Fehlern und hoher Varianz, da sie auf unabhängig voneinander rekonstruierten Bildern mit entsprechend

schlechter Statistik aufbauen. Daher wurde ein direkter parametrischer Rekonstruktionsalgorithmus entwickelt, welcher die strukturelle Information der MRT zur Regularisierung von Aktivitätsbildern, Parameterbildern, oder beiden gleichzeitig verwenden kann. Der Algorithmus zeigte für simulierte [^{18}F]FDG Daten eine Reduzierung des totalen normalisierten mittleren quadratischen Fehlers um 27 %, und sogar um 45 % bei der zusätzlichen Verwendung von struktureller Information. Es konnte gezeigt werden, dass gleichzeitige Regularisierung in allen Fällen die Varianz bei gleichem Fehler gegenüber der einzelnen Regularisierung reduziert. Für klinische [^{18}F]FET Daten konnte das Kontrastverhältnis in einem Gehirntumor um 140 % gegenüber dem indirekten Verfahren verbessert werden.

Als Grundlage wurde ein Framework zur Bildrekonstruktion entwickelt, welches den Biograph mMR Scanner und die besonderen Anforderung von PET/MR voll unterstützt und ausserdem umfangreiche Möglichkeiten zum schnellen Entwickeln von Bildverarbeitungsalgorithmen und deren Analyse bietet.

Acknowledgements

First of all I would like to thank Prof. Alexander Drzezga for accepting me as a Ph.D. student at the Klinikum Rechts der Isar. Under his supervision in the first year I gained knowledge in PET tracer kinetic modeling. In the following year I became a member of Prof. Sibylle Ziegler's medical imaging research group, where I could work on image reconstruction and kinetic modeling. I am deeply grateful to her for making this change possible. She has always shared her knowledge and experience in PET imaging with me and guided me through all my research projects. I would like to thank Prof. Nassir Navab from CAMP for his supervision of this thesis, and Dr. Gaspar Delso for his scientific advice and support in image reconstruction.

I would also like to thankfully mention Dr. Stefan Förster for providing clinical scans and fruitful discussions, as well as the MTAs Sylvia Schachoff and Anna Winter for their time and support in making patient data available to me. And the management team of the GSISH Graduate School for organizing interesting seminars and workshops beyond this thesis work.

My time at the department would not have been the same without fun activities and lunch dates with my colleagues Isabel, Shelley, Johanna, Manoj, Jan, Franz, Mathias, Jorge, Xiaoyin, Axel, ... thank you. A very special thank you goes to my office mates and friends Claudia and Frank. Thanks for all the cheerful moments during coffee breaks, you were a big emotional support especially in the last year of my thesis.

Lastly, it remains to thank my parents, and most importantly my husband Hans-Peter for his selfless support and encouragement throughout the time of this thesis. I dedicate this thesis to our wonderful children Johann and Friedrich.

The conducted research in this thesis was based on a PET/MR system that was funded through the Deutsche Forschungsgemeinschaft (DFG) Großgeräteinitiative 2010.

Contents

Abstract v

Zusammenfassung vii

Acknowledgements ix

Contents x

Abbreviations xv

Symbols xvii

1 Introduction 1
- 1.1 Multimodal Imaging . . . 1
- 1.2 Opportunities and obstacles in PET/MR image reconstruction . . . 5
- 1.3 Contribution and outline of this work . . . 8

2 Positron Emission Tomography 11
- 2.1 Fundamentals of PET and System Description . . . 11
  - 2.1.1 Positron Annihilation in PET . . . 11
  - 2.1.2 Synthesis of PET radiotracers . . . 12
  - 2.1.3 Detection system in PET . . . 14
  - 2.1.4 Coincidence detection . . . 15
- 2.2 Data Organization and Storage . . . 15
  - 2.2.1 Sinogram . . . 15
  - 2.2.2 Listmode . . . 15
  - 2.2.3 PET acquisition mode: 2D vs 3D . . . 16
- 2.3 Image degrading effects . . . 19
  - 2.3.1 Random and Scattered Events . . . 19
    - 2.3.1.1 Random events . . . 19
    - 2.3.1.2 Scattered events . . . 21
  - 2.3.2 Attenuation . . . 21
  - 2.3.3 Normalization . . . 23
  - 2.3.4 Spatial resolution in PET . . . 24
    - 2.3.4.1 Positron Range . . . 24

2.3.4.2 Noncolinearity . . . 26
2.3.4.3 Detector width . . . 26
2.3.4.4 Depth of interaction . . . 27
2.3.4.5 Additional effects . . . 27
2.4 Reconstruction Algorithms in PET . . . 28
2.4.1 Statistical Iterative Reconstruction Algorithms . . . 29
2.4.2 MLEM algorithm . . . 31
2.4.3 OSEM algorithm . . . 33
2.4.4 Maximum a posteriori algorithms . . . 33
2.4.4.1 One-Step-Late (OSL) algorithm . . . 34
2.4.4.2 De Pierro's MAP-EM . . . 35
2.4.5 Anatomically guided PET reconstruction . . . 36
2.5 Dynamic PET reconstruction . . . 38
2.5.1 Tracer kinetic modeling . . . 39
2.5.1.1 Two-tissue compartment model . . . 39
2.5.1.2 Parameter estimation . . . 41
2.5.2 Parametric image reconstruction . . . 41

3 Study of positron range and spatially-variant resolution recovery for the Biograph mMR Scanner 43
3.1 Positron Range in an integrated PET/MR scanner . . . 44
3.2 Related Work . . . 46
3.3 Materials and Methods . . . 47
3.3.1 Positron Range Simulations . . . 47
3.3.2 Reconstruction Framework with Positron Range Correction . . . 50
3.3.3 Positron Range Correction Kernels . . . 52
3.3.4 GATE Simulation and Phantom Studies . . . 55
3.4 Results . . . 57
3.4.1 Reconstruction With and Without Positron Range Correction For Homogeneous Tissue . . . 57
3.4.2 Positron Range Correction at Tissue Borders . . . 58
3.4.3 Extended Simulation Study for ^{82}Rb and ^{68}Ga . . . 60
3.5 Discussion . . . 61
3.6 Conclusion . . . 64

4 Maximum a posteriori direct parametric reconstruction using simultaneously acquired PET/MR information 65
4.1 Related Work . . . 66
4.2 Developing and evaluating a direct parametric reconstruction framework . . . 68
4.3 Theory . . . 69
4.3.1 Direct parametric PET reconstruction . . . 69
4.3.2 MAP reconstruction framework for parametric imaging . . . 70
4.3.2.1 Activity vs. parametric regularization . . . 70
4.3.2.2 Anatomically weighted Markov prior . . . 71
4.3.3 Optimization Transfer . . . 72
4.3.3.1 Separable Surrogate for Log-likelihood . . . 72
4.3.3.2 Separable Surrogate for Penalty . . . 73

4.3.3.3 Algorithm for MAP direct reconstruction. 75
4.3.4 Scaling Parameter Estimation 76
4.3.5 Analytical Tissue Compartment Modeling using Feng's input function model 77
4.4 Methods 78
4.4.1 Simulation study for [^{18}F]FDG 78
4.4.2 Algorithm Implementation 79
4.4.3 Quantitative Analysis 81
4.4.4 Evaluation on clinical [^{18}F]FET PET/MR data 82
4.5 Results 82
4.5.1 Simulation study for [^{18}F]FDG 82
4.5.1.1 Distance-weighted vs. Bowsher-weighted regularization . . . 82
4.5.1.2 Activity vs. parametric regularization 86
4.5.1.3 Impact of statistics 89
4.5.2 Clinical [^{18}F]FET PET/MR data 90
4.6 Discussion 92
4.7 Conclusion 97

5 Development of a Reconstruction Framework for the Siemens Biograph mMR PET/MR Scanner 99
5.1 Requirements 99
5.2 Framework Overview 101
5.2.1 Key features 101
5.2.2 Architecture 102
5.2.3 Implementation Details 104
5.3 Examples and Results 106
5.3.1 Framework Results 106
5.3.2 Dynamic reconstruction using spectral basis functions 107
5.3.3 Non-local anatomical regularization and anatomical mismatch 109
5.4 Discussion 117

6 Conclusion 119

Bibliography 123

Abbreviations

PET	**P**ositron **E**mission **T**omography
MR(I)	**M**agnetic **R**esonance (**I**maging)
CT	**C**omputed **T**omography
FDG	**F**luoro**D**eoxy**G**lucose
FET	**F**luoro**E**thyl**T**yrosine
MPRAGE	**M**agnetization-**p**repared **r**apid **g**radient **e**cho
APD	**a**valanche **p**hoto**d**iodes
PMT	**p**hoto**m**ultiplier **t**ubes
MLEM	**m**aximum **l**ikelihood **e**xpectation **m**aximization
OSEM	**o**rdered **s**ubset **e**xpectation **m**aximization
MAP	**m**aximum **a** **p**osteriori
OSL	**o**ne-**s**tep-**l**ate
NNLS	**n**one-**n**egative **l**east **s**quares
PL	**p**enalized **l**ikelihood
DPIR	**d**irect **p**arametric **i**mage **r**econstruction
ROI	**r**egion **o**f **i**nterest
LOR	**l**ine **o**f **r**esponse
FOV	**f**ield **o**f **v**iew
2TC	two-**t**issue **c**ompartment model
TAC	**t**ime **a**ctivity **c**urve
AIF	**a**rterial **i**nput **f**unction
IRF	**i**mpulse **r**esponse **f**unction
1D/2D/3D/4D	one-/ two-/ three-/ four-**d**imensional
MF	**m**agnetic **f**ield
3 T	three **T**esla
$\mathbf{T_{1/2}}$	half life
$\mathbf{R_{max}}$	maximum positron range
MRD	**m**aximum **r**ing **d**ifference
DOI	**d**epth **o**f **i**nteraction
μ**-map**	attenuation map
ACF	**a**ttenuation **c**orrection **f**actor
PSF	**p**oint **s**pread **f**unction

FWHM	**f**ull **w**idth at **h**alf **m**aximum
FWTM	**f**ull **w**idth at **t**enth **m**aximum
nRMSE	**n**ormalized **r**oot **m**ean **s**quared **e**rror
NSD	**n**ormalized **s**tandard **d**eviation
STD	**st**andard **d**eviation
SNR	**s**ignal to **n**oise **r**atio

Symbols

$A = (a_{ij}) \in \mathbb{R}^{I \times J}$	system matrix
$y = (y_1, \ldots, y_I)$	measurements
$x = (x_1, \ldots, x_J)$	activity image
$r = (r_1, \ldots, r_I)$	random events
$s = (s_1, \ldots, s_I)$	scattered events
$n = (n_1, \ldots, n_I)$	background (random + scattered) events
$\hat{x}$	ML image estimate
j	index of voxel
J	number of voxels
i	index of sinogram bin / LOR
I	number of LORs
m	index of time frame
M	number of time frames
α	regularization parameter
n	iteration index
N_j	neighborhood of voxel j
$L(x)$	log-likelihood function
$\Psi(\cdot)$	MAP objective function
$\psi(\cdot)$	potential function
$S(\cdot)$	surrogate function
$R(\cdot)$	prior function
$C_p(t)$	arterial input function
$C_T(t)$	tissue time activity curve
$\theta^p \in \mathbb{R}^J$	p-th parameter image
K_1, k_2, k_3, k_4	2TC rate constants
Z_n^m	Zernike polynomial of order n and repetition m
R_n^m	Radial polynomial of order n and repetition m
A_n^m	Zernike moments of order n and repetition m

Chapter 1

Introduction

Multimodal imaging provides great opportunities but comes with its own set of challenges. We motivate how advanced imaging algorithms can both leverage the great potential as well as overcome obstacles.

1.1 Multimodal Imaging

Technological advancements and innovations in healthcare play a major role in improving quality of life today, and there has been a steady increase in life expectancy over the years. Medical imaging devices have an integral part in this development and have become irreplaceable tools for diagnosis and treatment of many diseases [78]. Today, a large variety of different diagnostic imaging modalities is available, including *ultrasound imaging*, *magnetic resonance (MR) imaging (MRI)*, *computed tomography (CT)*, *single photon emission computed tomography (SPECT)*, and *positron emission tomography (PET)*. While MR and CT images reveal mostly anatomical information, molecular imaging procedures such as SPECT and PET are able to visualize and quantify functional processes such as glucose metabolism, blood flow or oxygen use. Fig. 1.1 shows examples of PET and MR images that provide information on metabolic activity and anatomical structure inside the human body.

Multimodal imaging combines such complementary data from different modalities for improved diagnostics, and may be able to overcome inherent weaknesses present in some modalities. For example, molecular imaging such as PET offers unparalleled sensitivity with respect to lesion detection in oncology, but suffers from low resolution and the lack of anatomical landmarks. It is therefore usually combined with high-resolution anatomical information from CT or MRI. Software-based multimodal imaging virtually combines images acquired on separate devices on a computer via sophisticated alignment and registration

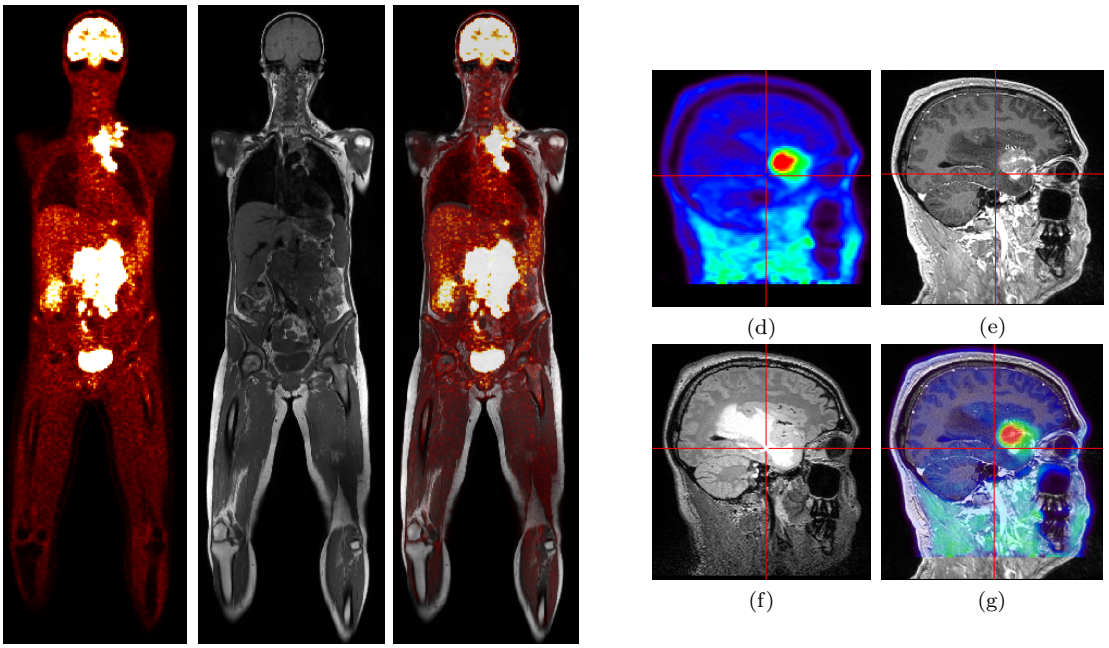

Figure 1.1: Examples of PET and MR images acquired with a Siemens Biograph mMR scanner. The images show cancer patients who underwent a whole-body (a)-(c) and a brain only (d)-(g) scan. (a) Coronal PET image that maps the distribution of [^{18}F]FDG, i.e., glucose consumption in the human body thus highlighting metabolically active areas. Normal high [^{18}F]FDG uptake is found in the brain, the kidneys and the bladder. Lesions showing abnormal high [^{18}F]FDG uptake are visible in the abdomen and thorax of the patient. (b) Corresponding T1-weighted MR image (MPRAGE) after contrast agent injection. It provides high-resolution anatomical detail. (c) Fused view with the PET image overlaid on top of the MR image. The MR image provides precise anatomic localization and delineation of PET abnormalities. (d) Sagittal PET image of the brain using [^{18}F]FET, an amino acid PET tracer, clearly showing a tumor in the patient's head. [^{18}F]FET imaging provides better tumor to normal tissue contrast than [^{18}F]FDG imaging. (e) Corresponding MR image of the patient's head using a T1-weighted (MPRAGE) sequence and (f) a T2-weighted sequence that shows brain anatomy also revealing structural changes in the patient's brain. (g) Fused view with the PET image overlaid on top of the MPRAGE image.

algorithms. Even though registration software has significantly improved in alignment accuracy in the past few years, only hardware fusion into a single multimodal imaging device allows to acquire images in close temporal and spatial proximity in a single scan session. Although more costly, hardware fusion minimizes the potential of misregistration in the multimodal data set and provides for a deeper and more comprehensive insight into an underlying disease.

The hardware fusion of PET and CT (PET/CT) imaging has been a key milestone in the era of multimodal imaging. It combines two complementary imaging modalities providing high-resolution anatomical information from CT that is accurately aligned with functional information from PET [173]. In 1998, Townsend *et al.* [30] presented the first combined PET/CT prototype. The results from this prototype has shown that adding anatomical

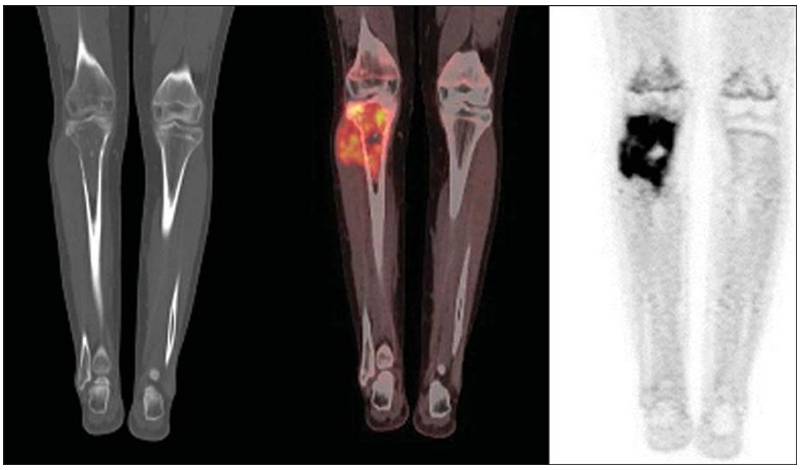

Figure 1.2: PET/CT image (middle) of patient diagnosed with Ewing's sarcoma. The CT image excels in delineating bone structure but provides only limited contrast in soft tissue parts. Image from [88] under CC-BY-NC.

landmarks from CT to PET findings leads to improved diagnostic accuracy. An example is given in Figure 1.2. Another important advantage of PET/CT is that the CT images can be used to correct the PET data for attenuation that occurs due to photon absorption and scatter in human tissue along the way from origin of the photon to the end of the detector and leads to a loss of coincident events. Whereas in standalone PET devices a lengthy transmission scan is needed where an external positron-emitting radionuclide source, typically ^{68}Ge/^{68}Ga, producing 511 keV photons, rotates around the patient measuring the attenuation of the transmitted photons, PET/CT devices can make direct use of the CT image to perform attenuation correction. This significantly reduces the total scanning time. Shortly after its introduction, PET/CT scanners became commercially available in 2001 with the release of the Biograph (Siemens Medical) and the Discovery LS (GE Healthcare). Nowadays, all major vendors for medical imaging equipment, including GE Healthcare, Hitachi Medical, Philips Medical Systems, Toshiba Medical Corporation and Siemens Medical Solutions offer PET/CT solutions. Though the individual design and performance of the scanners is vendor specific, all PET/CT devices share the same sequential design: A commercial PET scanner is placed in tandem with a commercial CT scanner and connected by a moving patient bed that allows sequential acquisitions of both modalities in short time intervals. In the past few years, the performance of PET/CT scanners has steadily improved due to independent advances in CT and PET technology, making them a very powerful and versatile tool for the assessment of many diseases today. Particularly in oncology, PET/CT has emerged as an indispensable tool for diagnosing, staging and evaluating treatments over the years. Presently, PET is no longer commercially available in a standalone unit, but only in combination with CT [135].

Combining PET with MR instead of CT into a PET/MR scanner also has great potential to improve PET images and can be of tremendous clinical use [194] [200]. Since MRI does not expose the patient to radiation, the overall exposure is significantly reduced, which is particularly important in pediatric oncology and long term follow-up studies. Due to the high soft tissue contrast provided by MRI, PET/MR has promising applications in the brain, breast, prostate and abdomen, where CT only provides limited contrast. Another strength of MRI that PET/MR benefits from is the tremendous flexibility of MRI with respect to different pulse sequences (such as T1, T2) and variable imaging parameters. These sequences and parameters determine tissue contrast, e.g., when contrast agents are used that changes T1 and T2 relaxation times, and enable functional imaging options (such as BOLD-fMRI, DWI, DCE).

Consequently, a big effort has been made in the past years to merge PET and MR technology [64] [179]. Similar to PET/CT systems, the scanner architecture for whole body PET/MR can be a sequential configuration that combines two well established and independently operating PET and MR subsystems. The subsystems are spaced sufficiently apart from each other to minimize interference. This sequential design concept has been realized in the commercial tri-modality GE PET/CT+MR scanner and the Philips Ingenuity TF PET/MR scanner. Such systems are comparably easy to design, as the engineering work for sequential scanners mainly consists in designing a dedicated shuttle system that moves the patient from one scanner to the other. However, the sequential design suffers from drawbacks similar to the ones encountered in sequential PET/CT systems, aggravated by the fact that MR scans are generally more time consuming than CT.

These drawbacks are overcome by a fully integrated scanner architecture that allows simultaneous acquisition of PET and MR data. However, such an architecture also presents a much greater technological challenge, as it requires the construction of a PET scanner inside an MR scanner, essentially complicating the design of each one. A PET scanner must detect gamma ray annihilation photons emitted from positrons to infer the distribution of a radioactive tracer in the body, but conventional PET detectors based on photomultiplier tubes (PMTs) are highly sensitive to magnetic fields. The key technology towards realizing a fully-integrated solution was a new detector technology based on avalanche photodiodes (APD) with lutetium oxyorthosilicate (LSO) crystals and more recently silicon photomultipliers (SiPMs) that both can operate in the presence of high magnetic field strengths.

With the Biograph mMR Siemens was the first to present a combined whole-body PET/MR scanner with a fully-integrated architectural design [63]. It became operational for clinical-use evaluation at the university hospital Klinikum rechts der Isar of Technische Universität München in November 2010. The mMR architecture is based on a clinical 3 T MR system (Verio) that has been modified to incorporate an APD based PET detector ring that is placed

Figure 1.3: The Siemens Biograph mMR fully-integrated PET/MR scanner. Image courtesy of www.siemens.com/press.

inside the magnet between the radiofrequency (RF) body and gradient coils as sketched in Fig. 1.3.

1.2 Opportunities and obstacles in PET/MR image reconstruction

Given the availability of high-quality, simultaneously acquired PET/MR data from such integrated devices opens another challenge: Yet-to-be designed image reconstruction techniques, mathematical models, algorithms, and software that fully leverage the potential of such data while overcoming the obstacles introduced by the integrated architecture or the limitations of each modality. The primary focus of a PET/MR scanner is to obtain high-quality PET images that must be timely generated, artifact free, and quantitative for full acceptance in clinical routine. Opportunities and obstacles arising from PET and combined PET/MR imaging include:

- **Resolution** in PET images is limited [126], e.g., by statistical and geometrical effects and generally much lower than that of an MR scan. Constraining the PET images appropriately with anatomical information from the MR images therefore has great potential to improve the resolution and overall quality of PET images. This is best achieved with accurately aligned PET and MR images that are simultaneously

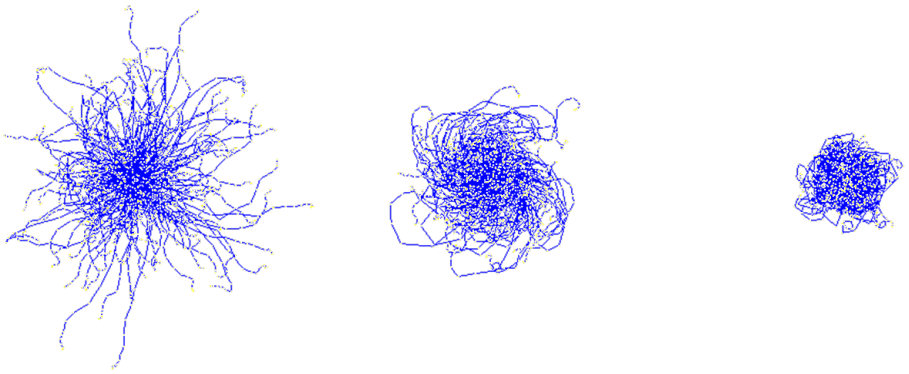

(a) 0 T (b) 3 T (c) 7 T

Figure 1.4: Influence of a magnetic field on annihilation distribution illustrated in transaxial view. ^{82}Rb in soft-tissue was simulated using Geant4 in the presence of a (a) 0 T, (b) 3 T, and (c) 7 T magnetic field.

acquired as provided by an integrated scanner. Active research includes the development of mathematical frameworks to incorporate such anatomical data, but also to investigate the correlation of PET and MR images and to develop algorithms that are resilient in parts of the image where there is no such correlation.

- **Positron range**, i.e., the distance between the positron's origin and its point of annihilation is a physical factor that limits resolution in PET. The effect of a magnetic field on positrons has been investigated and partially also motivated the combination of PET and MR technology: Since the Lorenz force exerted by the magnetic field of an MR scanner reduces the range of positrons in directions transverse to the magnetic field, the transaxial spatial resolution of PET is improved. The higher the magnetic field strength, the stronger the effect, as is illustrated in Fig. 1.4 using simulated data. However, positron range in a magnetic field is not only reduced, but also anisotropically distributed, leading to a more concentrated distribution along the direction of the magnetic field, which needs to be corrected by appropriate methods [115]. Furthermore, since positron range is also tissue specific and, e.g., much higher in lung than in soft tissue, this can cause artifacts at tissue boundaries.

- **Parametric Imaging** is a quantitative, voxel-based analysis technique of PET data to visualize physiologically relevant parameters representing the behavior of the radiotracer inside the body [40]. Parametric images are generated by fitting the tracer activity over time as captured by dynamic PET acquisition to an appropriate tracer-kinetic model. Existing approaches that fit an independently reconstructed sequence of PET frames over time severely suffer from noise, because shorter time frames for PET result in less detectable photons and poorer statistics. Thus, noise-robust parametric imaging techniques that directly incorporate the kinetic model together with

anatomical information from the MR image into the reconstruction process are an active research area.

- **Attenuation correction** information can be acquired by a transmission scan, which is usually considered too time consuming. Therefore, attenuation images must be derived from the other modality. This works well for PET/CT, where Hounsfield units can be converted to linear attenuation coefficients at 511 keV, but there is no direct relation between MR signal intensity and attenuation of 511 keV photons in PET/MR. Bone and air for example as extreme cases for tissue attenuation, do not produce a signal in MRI and thus appear both black. In addition, attenuation caused by MR hardware such as MR coils needs to be corrected, but they are not visible on either PET or MR images. Different approaches have been developed for MR-based attenuation correction [183], including template and atlas based approaches, but also segmentation approaches that directly work on an acquired patient MR image.

- **Motion correction** can improve PET image quality, especially for thorax or cardiac scans but also brain studies that may be affected due to lengthy acquisition times in the range of 10s of minutes for PET. Specialized MR sequences are developed that allow continuous tracking of movement, which in turn can be incorporated into the PET reconstruction process [177].

A brief example of how algorithms can be used to overcome an obstacle in integrated PET/MR scanners is given in the following [5]. The field-of-view of the MR system in a whole-body PET/MR scanner is limited due to the spatial constraint imposed by the design of the device [8]. This can cause holes in the MR-derived attenuation map, as shown in Fig. 1.5a, which leads to artifacts in the PET image. For a synthetically generated case with sinusoidal cropping areas as shown in Fig. 1.5c, we found that missing attenuation information even at the boundary of the image can lead to severe reconstruction errors not only locally but also in the interior of the patient with up to 30 % underestimation (see Fig. 1.6a). Filling the gaps in the MR image therefore has the potential to improve image quality significantly. Image inpainting is an established general-purpose image correction technique typically used, e.g., to remove tears from images by extrapolating missing information from the data located at the neighborhood of the missing image parts. We implemented a multi-resolution, partial differential equation-based anisotropic diffusion algorithm that diffuses boundary pixels until the holes are completely filled while structure of the image is preserved. The algorithm requires a mask of the missing regions as input that was automatically computed by means of an image carving algorithm that uses thresholded maximum-intensity projection images. When the inpainted CT image as shown in Fig. 1.5d was used for attenuation correction, the reconstruction error was reduced to a clinically acceptable value of 2 % (see Fig. 1.6b).

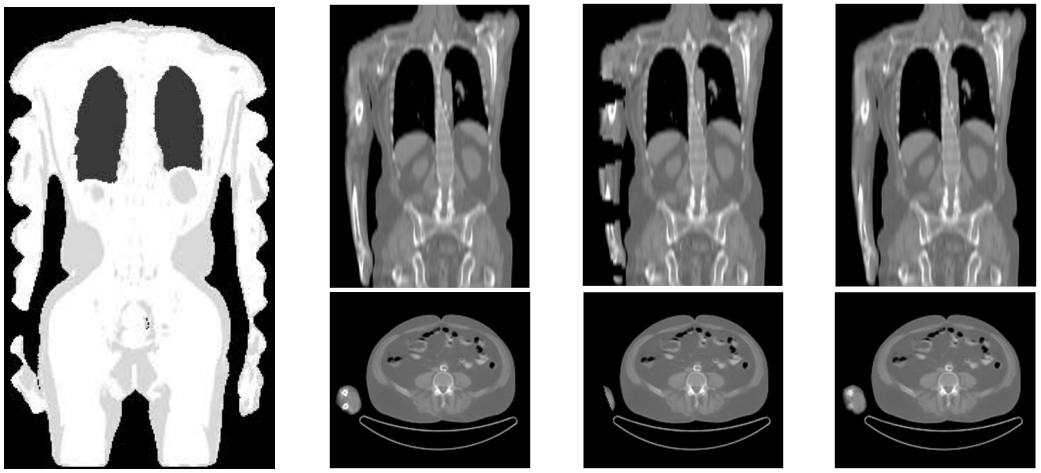

(a) (b) (c) (d)

Figure 1.5: (a) Sagittal slice of a patient's truncated attenuation map (μ-map) generated by the mMR showing missing attenuation information in parts of the arms and shoulders. Emulated limitation of MR FOV based on CT data (b) that were cropped with a sinusoidal mask (c). Inpainting restores attenuation information (d), as patient contours are prolonged, fine structures are continued, and surroundings are filled with soft tissue.

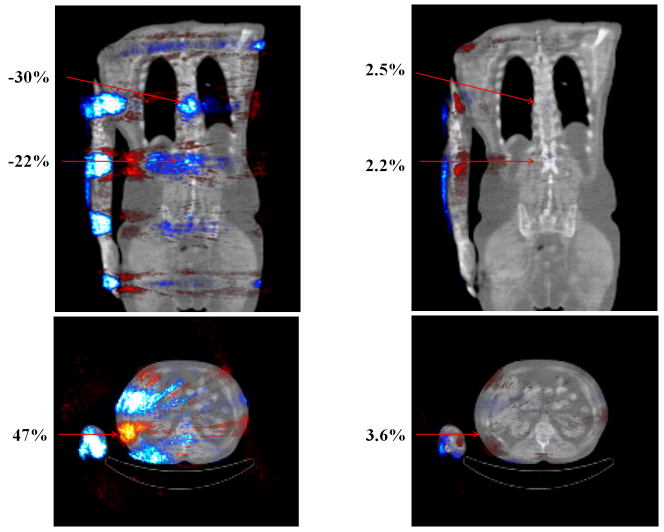

(a) (b)

Figure 1.6: Reconstruction bias overlaid on the original CT attenuation map. PET-reconstruction using the truncated attenuation map (a) and the inpainted attenuation map (b).

1.3 Contribution and outline of this work

The aim of this work is to develop and quantitatively evaluate novel PET image generation algorithms for the Siemens Biograph mMR scanner that either address an obstacle imposed by the integrated design or take advantage of simultaneously acquired PET and MR data.

Chapter 2 of this thesis introduces PET imaging in greater depth, describing physical foundations, data acquisition, correction methods, reconstruction algorithms, quantitative analysis, and direct reconstruction.

In Chapter 3 we identify the spatial resolution degrading effects due to positron range in PET under the influence of the 3 T magnetic field as an obstacle for PET/MR scanners and propose a correction method [1] [3]. For the first time, the occurrence of artifacts due to the anisotropic distribution of positron range in a magnetic field and its tissue dependency was evaluated quantitatively. Therefore, simulations were performed using the GATE Monte-Carlo simulation toolkit with an accurate model of the scanner, as well as with the Geant4 toolkit. A novel resolution recovery algorithm was developed that leverages pre-simulated data and the underlying tissue information that is available from the simultaneously acquired MR-based attenuation map. The algorithm was tested on simulation data using high-energetic ^{82}Rb and ^{68}Ga radioisotopes.

In Chapter 4 a dynamic PET reconstruction algorithm is presented that takes advantage of high-quality MR-based anatomical information in order to improve the quality and resolution of dynamic (4D) PET reconstruction and parametric images [2]. Voxel-wise tracer-kinetic modeling is very susceptible to noise, and even state-of-the-art direct reconstruction methods must sacrifice resolution to obtain stable results. Our approach is novel in that it provides in itself a framework for incorporating anatomical information within the reconstruction process, either to the activity image, the resulting parametric image, or both. Optimization transfer using an expectation-maximization surrogate and a new Bowsher-like penalty surrogate was applied to obtain a voxel-separable algorithm that interleaves a reconstruction with a fitting step. We present a quantitative analysis based on simulated data and, for the first time, high-quality 3D parameteric images from a clinical PET/MR scanner.

As a prerequisite effort described in Chapter 5, a reconstruction library was developed that is able to work with the clinical data provided by the new integrated scanner as well as simulated data. Rapid prototyping of reconstruction and image-enhancing algorithms for a newly-introduced PET/MR scanner such as the Biograph mMR requires a complex, readily available, and extensible software infrastructure that did not exist at the time the research presented in this work was conducted. Our framework satisfies all requirements toward that end and follows well-established software engineering principles. It covers all facets from Biograph mMR data import or generation, data correction, algorithm implementation, image synthesis, to analysis. The framework was used to prototype the algorithms presented in Chapters 3 and 4, and in addition was applied to work on input function estimation, anatomically-constraint images, and correcting for misalignment between PET and MR images.

The work concludes in Chapter 6, summarizing the main findings and discussing opportunities for future work based on our research.

Chapter 2

Positron Emission Tomography

Positron emission tomography (PET) is an imaging modality that visualizes functional processes in the human body by use of radioactive labeled molecules. These molecules are often referred to as radioisotopes and are administered to the patient as a radiotracer passing through their body during the scanning process. The radiation emitted by the radiotracer is detected by a PET camera and used to generate a *three-dimensional (3D)* image of the radiotracer's distribution. The type of radiotracer depends on the intended purpose of the scan.

After introducing the physics of PET imaging and describing the detection system, we summarize PET data acquisition and organization. A more detailed overview is given on PET reconstruction algorithms and especially reconstruction approaches that use anatomical information. At the end of this chapter, dynamic reconstruction methods are presented with a focus on direct parametric imaging based on kinetic modeling.

2.1 Fundamentals of PET and System Description

2.1.1 Positron Annihilation in PET

PET uses radioisotopes that decay by positron emission, also known as beta plus (β^+) decay. This form of decay corrects the imbalance in the ratio of protons to neutrons that results from an excess number of protons, by converting a proton (p) into a neutron (n) and releasing a positron (β^+) and a neutrino (v) from the nucleus:

$$p \rightarrow n + \beta^+ + v$$

Table 2.1: Clinically used PET radiotracers

Radiotracer	**Target**
^{18}F Fluorodeoxyglucose (FDG)	Glucose Metabolism
^{18}F Fluoride	Bone Cancer
^{18}F Fluorothymidine (FLT)	Cancer Cell Proliferation
^{18}F Fluoromisonidazole (FMISO)	Tumor Hypoxia
^{18}F Fluoroethyltyrosine (FET)	Brain Tumor Amino Acid Metabolism
^{18}F Fluoro-DOPA (FDOPA)	Brain Tumor Amino Acid Metabolism
^{11}C Raclopride	D2 dopamine receptor binding (Parkinson)
^{11}C Methionine (MET)	Brain Tumor Amino Acid Metabolism
^{11}C Choline	Cell Membrane Metabolism (Prostate Cancer)
^{11}C Pittsburgh compound B (PIB)	β Amyloid Plaques (Alzheimer)
^{13}N Ammonia	Myocardial Perfusion
^{68}Ga DOTATOC	Neuroendocrine Tumors
^{82}Rb	Myocardial Perfusion

An example of β^+ decay is the unstable element fluorine-18 (^{18}F) that decays into a new element, the stable isotope of Oxygen (^{18}O) that has an unchanged mass number but an atomic number that is decreased by one unit:

$$^{18}_{9}F \rightarrow ^{18}_{8}O + \beta^+ + v$$

The positron is emitted from the nucleus and then undergoes interactions with the surrounding matter: Inelastic collisions with nearby atomic electrons mostly lead to a loss of energy, while elastic collisions with atomic nuclei cause large-angle deflections that make the positron's path through tissue tortuous [115] [26]. When almost at rest, the positron combines with an electron and annihilates, emitting electromagnetic radiation in the form of two 511 keV gamma photons that travel in precisely opposite directions. These annihilation photons can subsequently be detected by PET detectors that surround the patient. The principle of PET imaging is schematically illustrated in Figure 2.1.

2.1.2 Synthesis of PET radiotracers

Most radioisotopes used for PET imaging are artificially manufactured by a charged particle accelerator, called a cyclotron, that transforms a stable target isotope into an unstable radioactive isotope by high-energy proton bombardment. For example, using ^{18}O enriched water as a target, the most common ^{18}F isotope is produced after emission of a neutron from the nucleus:

$$^{18}_{8}O + \beta^+ \rightarrow ^{18}_{9}F + v$$

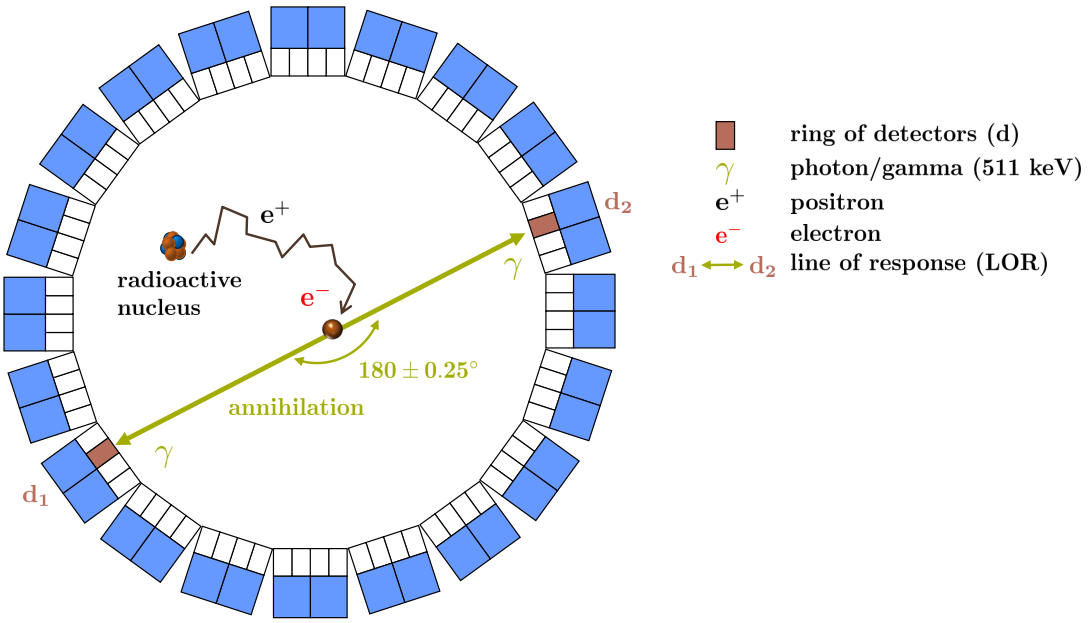

Figure 2.1: Principle of PET imaging.

Other relevant PET radioisotopes generated by a cyclotron include ^{11}C, ^{15}O and ^{13}N. Due to the relatively short half-life of most PET radioisotopes (see Tab. 2.1), on-side production is often required. An exception is ^{18}F, which allows for distribution over a limited distance thanks to its long half-life of 109.8 minutes in comparison to 20.4 minutes or 122 seconds for ^{11}C and ^{15}O, respectively [137]. In a subsequent production process, the radioisotope is incorporated into a biological molecule by chemical synthesis to produce the final radiotracer, which can then be injected into a patient. Among the many PET radiotracers that have been developed for specific imaging targets (see Table 2.1), ^{18}F radioactively labeled *fluorodeoxyglucose (FDG)* [77] is by far the most commonly used oncologic PET tracer [62]. [^{18}F]FDG imaging takes advantage of an elevated level of glucose consumption in cancer cells that has has been discovered by Warburg [191] [190] in the early 1930s. It is a valuable tool for the study of different types of cancers including breast cancer, colorectal cancer, esophageal cancer, head and neck cancer, non-small cell lung cancers, melanoma, and lymphoma [195] [76] [151].

In addition to its prominent role in oncology, PET also has important applications in cardiology and neurology: Myocardial perfusion imaging using ^{82}Rb, ^{13}N-Ammonia or ^{15}O water PET tracers [155] and myocardial viability scans [153], mostly using [^{18}F]FDG, are the main clinical procedures for the assessment of coronary artery diseases. In neurology PET has emerged as a powerful research and diagnostic tool, covering a wide range of neurological conditions including brain tumors, epilepsy, dementia, movement disorders, and stroke [166] [131].

2.1.3 Detection system in PET

A PET scanner is built from thousands of scintillation detectors that are typically organized in multiple adjacent rings surrounding the patient as illustrated in Figure 2.1. A scintillation detector converts the incident high energy photon into scintillation light. This light can be detected by a photo-detector that is optically coupled to the scintillator and that converts the light into an electrical signal. Usually a block detector design where crystals are grouped together into blocks is used, e.g., an 8×8 array of crystals paired with 4 photo-detectors. The output signal from all photo-detectors is used to determine the position of the detecting crystal. The four main requirements for a scintillation material to be used in PET are the following [26]: 1) high stopping power, which determines the mean distance that the incident photon travels before its energy is absorbed by the crystal, 2) short decay time, which indicates the duration of the light pulse generated by the scintillator, 3) high energy resolution in order to distinguish between true and Compton scattered photons that have lost energy, 4) good light output, which determines the number of scintillation photons generated by an incident photon. In the early days of PET, detectors were made of sodium iodide (NaI) crystals. These have been slowly replaced by *bismuth germinate (BGO)* crystals since the late 1970s due to their superior stopping power [47]. Currently, the most widely used scintillation material in modern PET scanners is *lutetium oxyorthosilicate (LSO)* mainly owing to its short decay constant of 40 ns and its light output approaching 30 photons/keV [114]. An alternative scintillator to LSO is *gadolinium ortho-silicate (GSO)*, that is characterized by better energy resolution facilitating scatter discrimination and better light output [26].

The most common type of photo-detectors used in standalone PET scanner are *photomultiplier tubes (PMTs)*. They operate based on the photoelectric effect that causes an emission of electrons in response to the absorption of incident light in the photo-cathode. The emitted electrons are accelerated through a serial chain of dynodes, producing an avalanche of electrons at the anode of the PMT due to electron multiplication down the chain. After further processing a digital pulse is passed to a coincidence circuitry (see 2.1.4). The main advantage of PMTs is their high gain (typically 10^6), resulting in high *signal-to-noise (SNR)* pulses [137]. However, apart from being bulky the biggest disadvantage of PMTs with regard to PET/MR scanners is their high sensitivity to magnetic fields, which leads to an inacceptable loss of gain. Despite some attempts to make PMTs work in a magnetic field for PET/MR devices [139] [179], e.g. by the use of better shielding of PMTs or optical fibers that guide the scintillation light out of the magnetic field, the approach pursued in commercially available PET/MR systems is to replace PMTs by MR-compatible light detectors, such as *avalanche photodiodes (APD)* as, e.g., used in the Biograph mMR [63], or *silicon photomultipliers (SiPMs)* [85].

2.1.4 Coincidence detection

PET relies upon the simultaneous detection of the emitted annihilation photons, termed coincidence detection. If two photons hit opposing detector within a coincidence timing window of typically $4 - 12$ ns, caused by limitations of timing resolution of detectors and electronics, the system registers this event as a coincidence event. It is assigned to the line that connects the pair of detectors, referred to as *line of response (LOR)* assuming that the detected photons originated from the same annihilation event somewhere along that LOR. Over the course of a PET scan, the system collects the number of coincidence events for all valid LORs inside a transverse and axial acceptance angle, which determines the FOV of the scanner. The sum is an approximation of the integrated activity along the LOR. From the collection of line integrals collected over multiple angles an image of the activity distribution can be extrapolated by using dedicated PET image reconstruction algorithms, which will be presented in Section 2.4.

2.2 Data Organization and Storage

In the following section we explain how the acquired raw data are organized and stored either in sinogram or list mode format. Organization into sinogram is first illustrated for a 2D PET acquisition mode for simplicity and then expanded to 3D acquisition mode.

2.2.1 Sinogram

We consider data that are acquired within a single detector ring of a scanner (2D). Each LOR can be parameterized by a radial distance r of the LOR from the center of the detector ring and an angle of orientation ϕ. The set of line integrals along all parallel LORs passing through the object at a fixed angle ϕ is called a 1D projection. As illustrated in Fig. 2.2 it is stored in a horizontal row of the sinogram matrix whose rows and columns correspond to values of ϕ and r, respectively. Finally, all the projections covering a range of angles from 0 to 180 fill up the sinogram matrix for the transaxial image plane defined by the detector ring. The term sinogram stems from the fact that an off-center point source is mapped to a sinusoidal curve in the sinogram matrix.

2.2.2 Listmode

In list mode format the LOR coordinates of all recorded coincidences are stored individually in a sequential data stream. In addition, information about timing, deposited energy

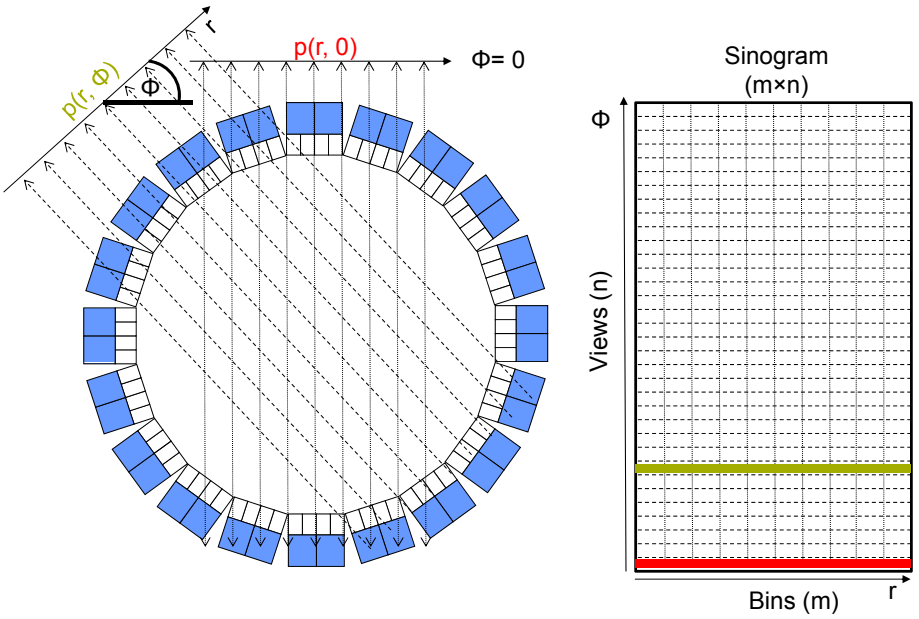

Figure 2.2: Data organization in sinogram: Each parallel 1D projection $p(\cdot, \phi)$ (left) is stored in a row of the sinogram matrix (right) corresponding to its projection angle ϕ.

as well as status information of an external signal (e.g. motion tracking device) can be included. Compared to sinograms, that contain the sum of the coincident events, list mode storage preserves high temporal and spatial information. The data can be flexibly rearranged afterwards, e.g., into a set of dynamic sinograms containing a predefined number of scans (frames) of selected frame durations for further kinetic analysis (see 2.5.1), or into gated sinograms by dividing each respiratory cycle into a selected number of bins and bin durations to handle cardiac and other types of motion [141].

2.2.3 PET acquisition mode: 2D vs 3D

Older generation PET scanners are capable to operate both in 2D and 3D acquisition mode, referred to as 2D and 3D PET. As illustrated in Figure 2.3a, 2D PET records coincidences that occur within the same detector ring, called direct coincidences, and that are organized into direct planes. In addition, so-called cross coincidences occurring between adjacent detector rings are allowed (see Figure 2.3b). Cross coincidences are summed and organized into transverse cross planes that are axially positioned between adjacent detector rings. In order to restrict the number of coincidences, PET scanners are built with retractable inter-ring septas (see Figure 2.3a) that are made of an absorbing material such as tungsten or lead. Assuming an N-ring cylindrical PET scanner with ring indexes $n = 0, \ldots, N-1$ and an axial ring spacing z, a 2D PET data set comprises N direct and $N-1$ cross planes yielding a stack of $2N-1$ sinograms with an axial spacing of $z/2$. Each sinogram is independently

reconstructed using 2D reconstruction algorithms and the reconstructed slices can be stacked together to obtain a 3D image volume.

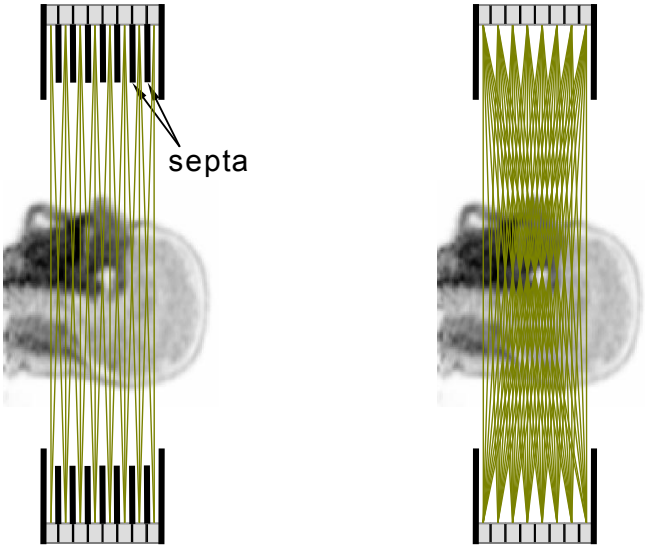

(a) 2D (b) 3D

Figure 2.3: Two-dimensional (2D) acquisition mode including septa between axial detectors (a) vs. a fully three-dimensional (3D) mode (b). Coincident events detected along the green lines are accepted during acquisition.

Modern PET scanners no longer use inter-plane septa to allow coincidences between any pair of detector ring (3D) up to a maximum axial acceptance angle (oblique angle) that is defined by the *maximum ring difference (MRD)* parameter of the scanner's specifications (see Figure 2.3b). The main advantage of 3D PET is a substantial increase in sensitivity over 2D by a factor of around $\times 5$ to $\times 7$ [137]. However, this comes at the cost of a considerable increase in background random and scattered events (scatter fraction as high as 40–60 % in 3D vs 10–20 % in 2D for whole-body imaging [49]). Accurate scatter and random correction methods are therefore required for 3D PET (c.f. Sec. 2.3.1).

In order to reduce the amount of data that needs to be stored in 3D PET (N^2 singrams), individual planes are combined axially. The so-called Michelogram named after its inventor Christian Michel [60] provides a graphical representation for data handling in 2D and 3D PET. As illustrated in 2.4 showing Michelograms for different acquisition modes, it is a square plot, where each cell represents the coincidence data (sinogram) between two detector rings plotted on the x- and y-axis. Asterisks in cells indicate that coincidences are allowed and included in the data set. Data from cells, that are connected by a line are combined into a single plane. A Michelogram is defined by the MRD and an odd integer, called span, that determines the extent of axial compression and is defined as the sum of the number of sinograms combined into odd-and even-numbered planes. As examples, in the Michelogram of a 2D mode with only direct coincidences allowed (see Fig. 2.4a) no planes are combined

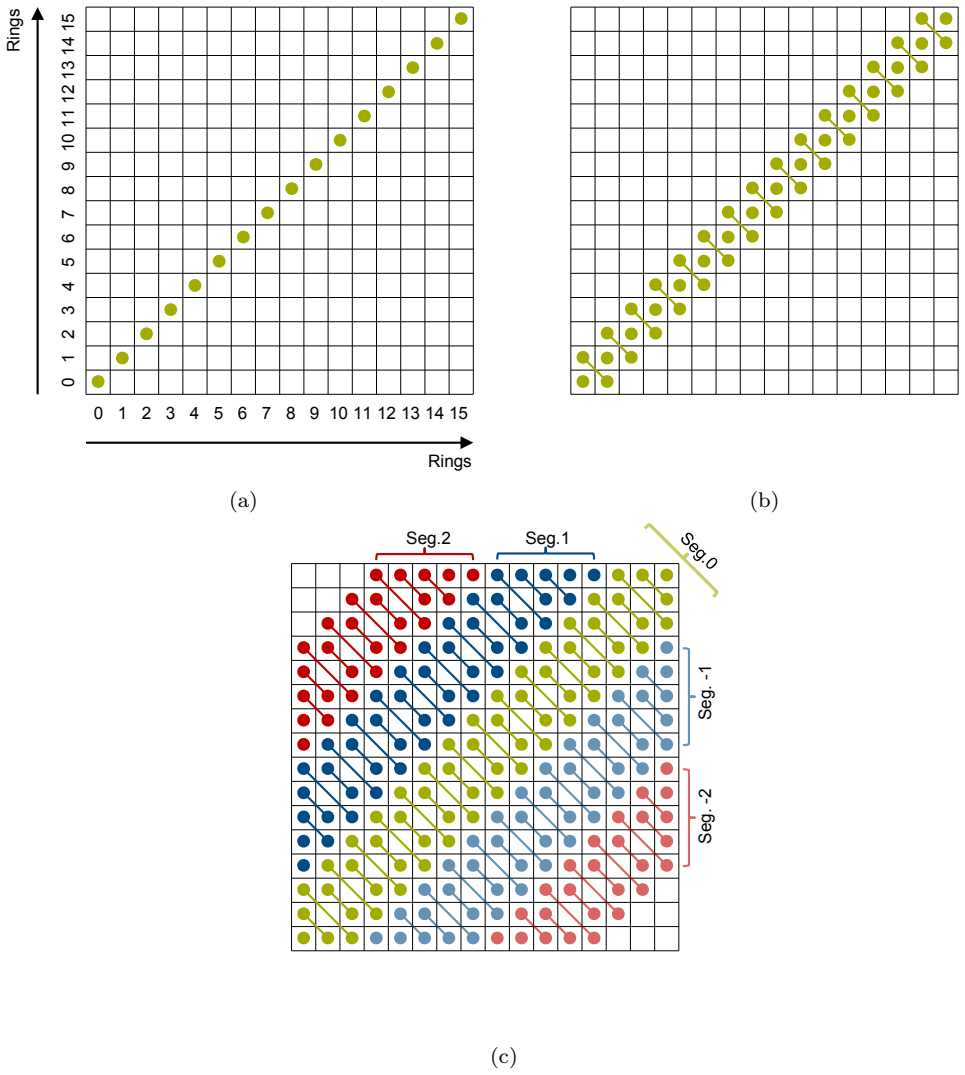

Figure 2.4: Three examples of Michelograms representing different acquisitions for a 16-ring PET scanner: (a) 2D acquisition with only direct planes (16), (b) 2D acquisition with cross planes, (c) 3D acquisition with an axial span of 5 and a maximum allowed ring difference of 12 resulting in 5 segments.

and the span equals to 1. When cross coincidences are added (see Figure 2.4b), the two off-diagonal planes right above and below of the main diagonal are included in the data and combined, resulting in a span of 3 (1+2). In 3D PET for a span of 5 and an MRD of 12, the Michelogram gets populated further away from the main diagonal (see Figure 2.4c). Data are grouped into sets of sinograms called segments that are numbered $0, -1, +1, -2, +2$ and so on. Whereas segment 0 contains transverse sinograms (direct and cross planes), all other segments contain oblique sinograms. With increasing segment index the sinograms become more oblique and fewer sinograms are in each segment. The data in Figure 2.4c, for example, are grouped into 5 segments.

Since reconstructions from 3D sinograms with multiple segments represent a significant computational burden, 3D data are often transformed into a stack of 2D transverse sinograms using a rebinning algorithm. The advantage is that efficient 2D reconstruction algorithms can be applied. Ideally, the improved sensitivity of 3D PET is maintained during the rebinning process. Single-slice rebinning [58] is the simplest approach at the expense of potentially reduced quantitative accuracy. More sophisticated but also more accurate is the Fourier rebinning algorithm [61], yielding quality of reconstruction close to true 3D reconstruction.

2.3 Image degrading effects

PET raw data are affected by numerous factors that can have a degrading effect on reconstructed image quality. These factors include undesired random and scattered background events, count loss due to attenuation, and varying detection sensitivities between pairs of detectors causing non-uniformity in the data. In addition, spatial resolution in PET is impacted by positron range, noncolinearity, detector size, depth of interaction, and more. All these factors need to be corrected to guarantee quantitative accuracy. Correction is either performed prior to reconstruction on the data as a pre-processing step or included in the system model that is used during reconstruction. In the following section, these degrading factors are explained along with corresponding correction methods.

2.3.1 Random and Scattered Events

The ideal signal in PET are true coincidence events that derive from a single annihilation event whose photons have not changed direction or lost energy on their way to the detectors [137] (see Figure 2.5a). However, due to PET detector limitations and possible photon interactions in human tissue, undesired events are also recorded that fall within the coincidence timing or energy window of the detectors. Measured coincidence events in PET, termed prompts, are categorized into true, random, and scattered events.

2.3.1.1 Random events

A random event, also called accidental event, occurs when two photons that originate from two separate, unrelated annihilation events (see Figure 2.5b) fall within the coincidence timing window of the scanner. The resulting LORs contain false local information about the tracer distribution. Randoms appear as a uniform background in reconstructed images

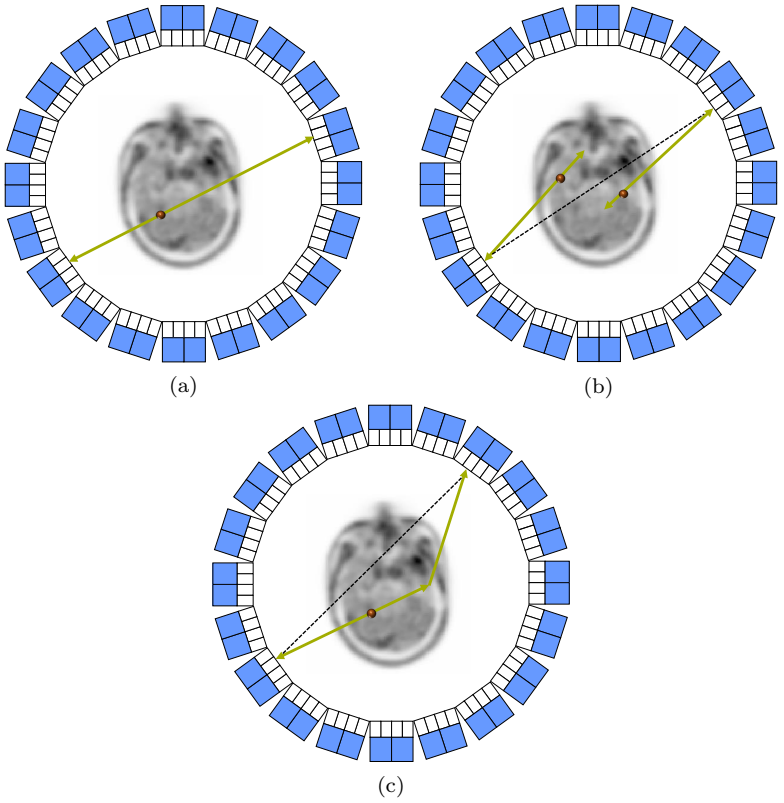

Figure 2.5: Illustration of three different coincidence events included in the PET prompt data: (a) true, (b) random, and (c) scattered coincidences. The green solid lines represent the path of the two single photons emitted by an annihilation event (marked by the red dot). The dashed black line represents the LOR of the coincidence event. Whereas in (a) the dashed and and solid lines coincide, the lines of the random (b) and scattered (c) events differ from each other leading to false positioning.

leading to a loss of contrast and artifacts in PET images if no correction is made. To obtain an estimate of random coincidences two methods have been proposed:

The singles-based correction method relies on the measurement of the single event rates S_a and S_b to obtain an estimate of the random coincidence count rate R_{ab} between a detector pair ab that is given by [37]

$$R_{ab} = 2\tau S_a S_b \tag{2.1}$$

where τ is the width of the coincidence timing window. As can be seen from 2.1, randoms increase quadratically with tracer activity and linearly with τ.

A more common method to correct for randoms is the delayed window approach. It uses a second coincidence window that has the same width as the coincidence timing window, but is delayed in time. The delayed window can be assumed to contain only random coincidences.

Given an estimate of the random coincidences, correction is often applied as a pre-correction step that subtracts the delayed coincidences from the measured prompt data. Alternatively,

if stored in a separate sinogram, randoms can be compensated for during image reconstruction using an extended system model.

2.3.1.2 Scattered events

A scattered event occurs, when at least one of the photons originating from the same annihilation event undergoes Compton scattering, i.e., it interacts with a loosely bound electron in the surrounding medium. A scattered photon looses energy and changes direction (see Figure 2.5c), which leads to incorrectly assigned LORs. Compton scattering results in diffuse background counts causing decreased image contrast. Various techniques have been proposed to estimate and correct for scattered coincidences in PET data.

A simple scatter correction method is the tail-fitting approach that estimates the scatter component by fitting an analytical function (e.g., a 1D Gaussian) to the measured prompts at the edges of the sinogram, known as scatter tails. The estimated scatter component is then subtracted from the measured data that have been pre-corrected for randoms. This method is mainly used for scatter correction in brain imaging, where pronounced scatter tails are present [48].

The most widely used class of scatter correction techniques are analytic model-based correction methods. The most successful scatter correction algorithm, implemented in most of today's software packages, is the *single-scatter simulation (SSS)* algorithm by Watson [192] [193]. This algorithm takes as input a preliminary emission estimate and an attenuation map that is used to define a set of scatter points. For each scatter point the single-scatter contribution to a given LOR is calculated based on the Klein-Nishina formula for Compton scattering. This is repeated for all LORs and the resulting scatter sinogram is then subtracted from the measured sinogram to yield a scatter corrected sinogram.

Alternative correction approaches include methods based on multiple energy windows, e.g., dual energy window [87], and convolution or deconvolution-based methods [29] [25].

2.3.2 Attenuation

Attenuation describes the loss of detection of photon annihilation pairs, which is mainly caused by Compton scatter of photons out of the detector ring. It leads to increased image noise and introduces image artifacts, e.g., in whole-body imaging, falsely elevated uptake in the lungs and skin or non-uniform distributions in organs such as heart and liver may occur.

In order to correct for attenuation, so-called *attenuation correction factors (ACFs)* for all measured LORs are required. They are defined as the reciprocal of the survival probability

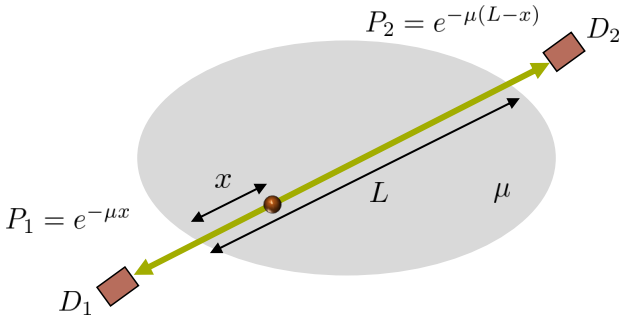

Figure 2.6: Coincidence detection in an attenuating medium. P_1 and P_2 denote the probability that a single photons emitted at depth x inside an attenuating medium with attenuation coefficient μ and dimension L reaches the detectors D_1 and D_2, respectively. The probability for both photons is $P_1 P_2$.

that a photon pair traverses the attenuating medium without interactions and reaches the detectors. In case of a uniform attenuation medium with attenuation coefficient μ (see Figure 2.6), the survival probability can be calculated as follows:

$$P = P_1 \times P_2 = e^{-\mu x} \times e^{-\mu(L-x)} = e^{-\mu L},$$

where L denotes the length of the medium along the annihilation path and x is the distance of the photon to the detector. For a more realistic, heterogeneous attenuating medium, P is given by

$$P = P_1 \times P_2 = e^{-\int_0^x \mu(x)dx} \times e^{-\int_x^{L-x} \mu(x)dx} = e^{-\int_0^L \mu(x)dx}.$$

The resulting ACFs are then multiplied to the measured data for all LORs to correct for attenuation. The challenge in attenuation correction (AC) is to accurately determine the ACFs. Most common approaches are based on transmissions scans or CT-or MR-derived attenuation images.

Transmission scans have been the method of choice in standalone PET scanners to measure the actual attenuation. They require an external positron-emitting source, typically ^{68}Ge, to rotate around the object inside the scanner. A blank scan using the external source but with no object inside the scanner is also acquired. Then, the ratio between the resulting blank and transmission sinograms produces a sinogram containing the ACFs for each LOR. By multiplying this sinogram with the emission sinogram, an attenuation corrected PET sinogram is obtained.

With the introduction of integrated PET/CT and PET/MR scanners, transmission scans are no longer needed, thus reducing overall scan durations. Instead, CT-or MR-derived attenuation images ($\mu-$maps) can be generated. In PET/CT imaging the CT image values

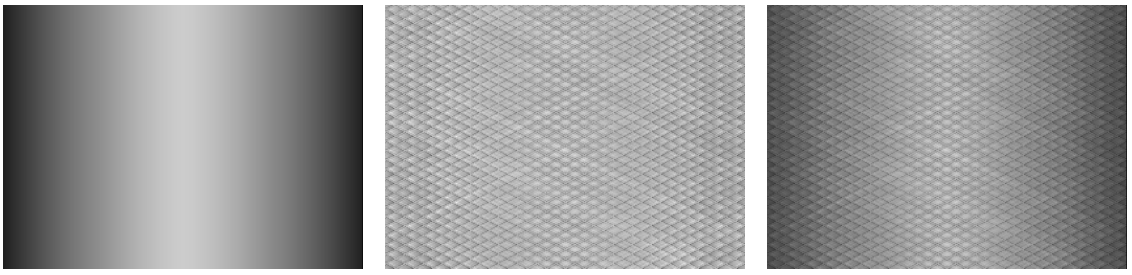

(a) (b) (c)

Figure 2.7: Normalization factors obtained from a normalization file of the Biograph mMR for a given sinogram plane: (a) geometric factors, (b) combination of all the other factors including intrinsic efficiencies, crystal interferences, and (c) final normalization sinogram used for reconstruction.

representing attenuation at CT energies ($\sim$ 80 keV) can be converted to attenuation at PET energies by bilinear scaling [110].

Generating $\mu-$maps from MR images is more challenging, since MR image intensities representing the distribution of hydrogen nuclei are physically unrelated to tissue attenuation properties. Still, various approaches have been developed to derive an MR-based $\mu-$map suitable for PET imaging [179]. Current generation PET/MR systems use segmentation-based approaches that assign PET attenuation coefficients to different tissue regions that are obtained by segmentation of MR images derived from dedicated MR sequences. Either three-tissue segmented $\mu-$maps (soft tissue, lung, and air) [154] or four-tissue segmented $\mu-$maps (water, fat, lung, and air) [121] are used, which are calculated from a T1-weighted MR sequence or the Dixon sequence (water-fat separation) [55] [69], respectively. Dedicated *Ultrashort EchoTime (UTE)* sequences that are capable to visualize cortical bone and facilitate its differentiation from air [41] [109] are acquired for brain imaging.

Alternative approaches for MR-based AC correction include atlas and machine learning-based techniques [112] [94] as well as joint estimation methods that simultaneously estimate activity and attenuation within an iterative PET reconstruction algorithm. Examples include the *maximum likelihood activity and attenuation (MLAA)* algorithm [133] [152].

2.3.3 Normalization

Normalization is another essential correction step required for quantitative PET data. It compensates for non-uniform detector efficiencies in PET scanners, arising from several factors such as: different locations of the detectors in the detector blocks, physical variations in crystals, variations in gain of PMTs, as well as geometric factors. Individual *normalization factors (NF)* for each LOR can be computed using a direct or component-based normalization approach. The resulting NFs are incorporated in the data model used for

reconstruction. In the direct approach, a normalization scan is acquired using a uniform planar or rotating line source (typically ^{68}Ge) that illuminates all possible LORs. The NF for each LOR is then calculated as the ratio of the measured number of counts in the LOR and the average counts for all LORs. In the component-based normalization approach the NF is decomposed into multiple normalization components. For the Biograph mMR the NF N for each sinogram bin i is modeled as [28]

$$N(i) = \varphi_r \times \epsilon_{d1} \times \epsilon_{d2} \times ci_{r,\theta} \times ap_z \times d_{d1} \times d_{d2},$$

where φ_r is a geometric factor, ϵ_{d1} and ϵ_{d2} are the intrinsic efficiencies of the two LOR crystals $d1$ and $d2$, $ci_{r,\theta}$ denote crystal interferences, ap_z is an axial factor, and d_{d1} and d_{d2} represent dead-time factors of the two LOR crystals. The components are saved in a normalization file of the scanner. Figure 2.7 shows exemplary normalization sinograms derived from an mMR normalization file containing geometric effects only (see Figure 2.7a) and intrinsic efficiencies and crystal interferences (see Figure 2.7b), as well as the final sinogram used during reconstruction (see Figure 2.7c).

2.3.4 Spatial resolution in PET

Spatial resolution is a major performance characteristic of a PET scanner. It indicates the smallest distance at which two points can be distinguished after image reconstruction. The system's response to a point is known as the *point spread function (PSF)*. Knowledge of the scanner's PSF can be used to partially recover the loss of resolution, e.g., by considering it in an iterative reconstruction algorithm, as was done for positron range correction in Chapter 3. Spatial resolution is affected by several factors related to the physics of PET, the detector design, the geometry of the scanner, as well as specific parameters used during reconstruction such as filter kernels. The following sections explain these factors in more detail.

2.3.4.1 Positron Range

Positron range poses a physical limit to spatial resolution in PET that results from the nature of positron emissions. After being emitted from the radioactive nucleus, a positron's initial energy is gradually reduced by interactions with electrons. At the end of a tortuous journey, it forms a bond with an electron, a state called positronium, that annihilates into two 511 keV gamma photons moving in exactly opposite directions. The point of origin of the positron, which is to be imaged, therefore differs from the point of annihilation (which ideally can be observed by the scanner's detectors) causing a blurring effect in the final images. The

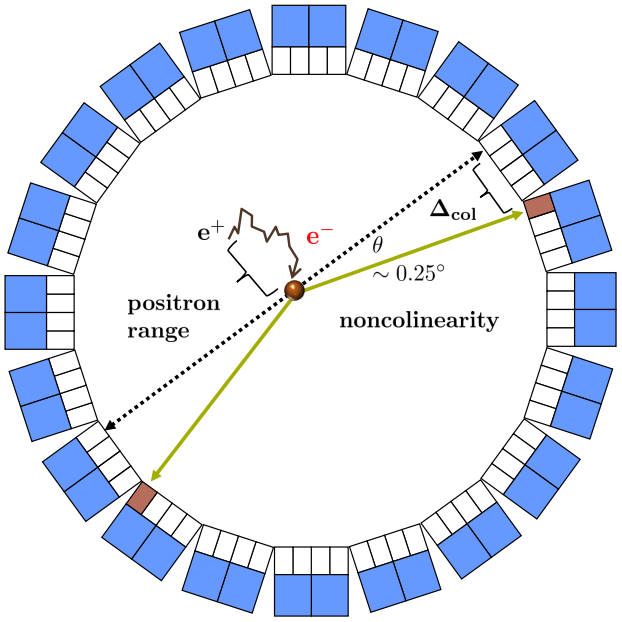

Figure 2.8: Illustration of two image degrading effects: positron range describes the distance that the positron travels prior to annihilation with an electron; the path of the annihilation photons deviates from 180° (noncolinearity).

effective positron range, as illustrated in Figure 2.8, is defined as the perpendicular distance of the positron's point of origin and the LOR along which the annihilation event occurred.

Positron range increases with the initial energy of the positron. Emitted positrons have an energy spectrum that is a characteristic of the emitting radioisotope and ranges from 0 MeV to a maximum (endpoint) energy E_{max}. E_{max} can be comparatively low, e.g., for ^{18}F with $E_{max} = 0.64$ MeV or high, e.g., for ^{82}Rb with $E_{max} = 3.4$ MeV. Table 2.2 shows a list of common radioisotopes and their associated E_{max}, maximum positron range R_{max}, and root mean square positron range R_{rms} in water. This means that positron range depends on the radionuclide being used. In addition, positron range also depends on the surrounding tissue type: it is larger in low density tissue such as the lungs than it is in higher density tissues such as soft-tissue or bone.

Positron range distributions have a cusp-like shape with long tails that can be fitted by exponentials or Gaussians. The resolution loss is typically described by the *full width at half maximum (FWHM)* from a Gaussian fit. Positron range is negligible for ^{18}F but it can become a concern in clinical scanners for high-energy radioisotopes such as ^{82}Rb or ^{68}Ga, particularly in low density mediums such as lung. In addition, the magnetic field as it is present in a PET/MR scanner influences the positron range: it is reduced in directions transverse to the magnetic field, and the overall distribution becomes anisotropic. This can cause image artifacts that need to be corrected appropriately (see Chapter 3).

Table 2.2: Physical properties of radionuclides used in PET (values taken from [203])

Radionuclide	$T_{1/2}$ **(min)**	E_{max} **(MeV)**	R_{max} **in water (mm)**	R_{rms} **in water (mm)**
^{11}C	20.4	0.96	3.9	0.4
^{13}N	9.96	1.2	5.1	0.6
^{15}O	2.05	1.7	8.0	0.9
^{18}F	109.8	0.64	2.3	0.2
^{68}Ga	68.4	1.9	9.0	1.2
^{84}Rb	1.3	3.4	18	2.6
^{124}I	6019.2	1.5	7.0	0.8

2.3.4.2 Noncolinearity

Another physical limitation stems from the fact that the positron carries a small residual momentum at the time of annihilation. This momentum causes an angular deviation from the 180° angle at which annihilation electrons theoretically travel. This is known as noncolinearity, and also illustrated in Figure 2.8. The angular distribution can be assumed to be Gaussian distributed with a FWHM of 0.5° (i.e., ±0.25° deviation) [137]. Unlike positron range noncolinearity does not depend on the injected radioisotope but only on the diameter D of the scanner. Image blurring caused by noncolinearity is expressed in FWHM and is given by [137]

$$\Delta_{col} = 0.5 \times D \times \tan(0.25^\circ) \approx 0.0022 \times D.$$

The impact of noncolinearity is relatively small: for an 80 cm diameter clinical scanner, Δ_{col} is less than 2 mm.

2.3.4.3 Detector width

The width d of the PET detectors has a significant impact on spatial resolution in PET and determines the intrinsic spatial resolution. Considering an opposing pair of detectors, the coincidence response as the source is moved across the detectors is described by a triangular function with the maximum at the midpoint between the detector and zero at the edges of the detectors. The FWHM of this function is half the detector width ($d/2$). The closer the source is located towards the face of either detector, the wider the coincidence response function becomes, up to a FWHM of d at the face of the detector [137].

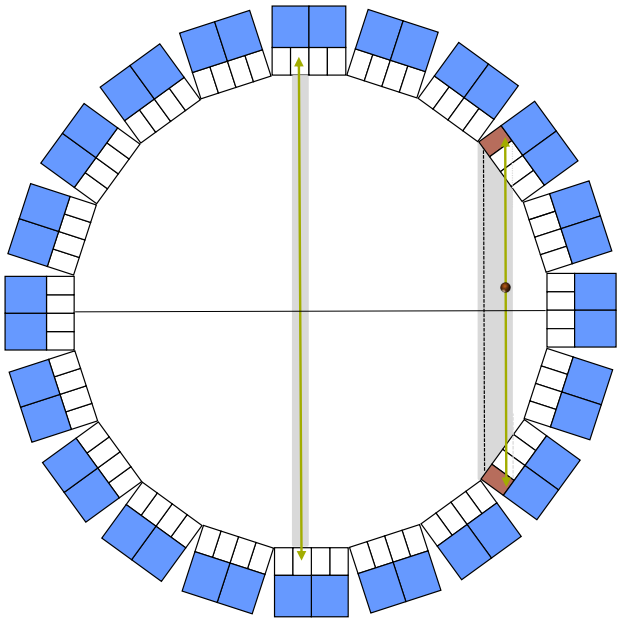

Figure 2.9: DOI effect: The emitted gamma rays from an off-axis source (indicated by the green line) can penetrate through neighboring detectors before being detected by a pair of detectors (marked in red). The falsely assigned LOR is indicated by the dashed black line connecting the detectors. The gray area marks all true annihilation paths that are assigned to the wrong LOR. This leads to poor radial resolution. Sources close to the center of the scanner are not susceptible to this effect.

2.3.4.4 Depth of interaction

Gamma photons can interact at varying depths within the detector. This so-called *depth of interaction (DOI)* effect, also known as radial elongation or parallax effect, poses a limitation on spatial resolution and manifests itself as a radial blur in the reconstructed image. Gamma photons emitted at the center of the FOV directly penetrate the detector's face and interact. Photons originating off axis, however, enter the detector at an oblique angle and can thus penetrate through neighboring detectors before they interact, as illustrated in Figure 2.9. This causes an uncertainty in the location, and the radial detector response becomes broad and asymmetric. The DOI effect depends on the radial offset of the source, the material of the detector, the length and width of the crystals, and the detector ring diameter [137].

2.3.4.5 Additional effects

Due to low count statistics, PET images often require a certain amount of smoothing that is either applied within or after reconstruction. The amount of smoothing is defined by the FWHM of the filter kernel. This causes a blur in the image and thus contributes to resolution loss. The overall resolution therefore also depends on the image reconstruction process.

2.4 Reconstruction Algorithms in PET

Reconstruction algorithms are needed to obtain an image of the tracer's distribution from the raw data generated by the PET scanner. Mathematically speaking, this is an inverse problem, which is commonly solved using analytical or iterative algorithms. In this chapter, we focus specifically on statistical iterative algorithms. They are computationally demanding but have become increasingly important for PET imaging, as computer speeds and memory capacities have increased. Nowadays, they have almost completely replaced simpler analytical inversion techniques such as filtered back projection.

A key characteristic of statistical algorithms is that they account for the statistics of the noisy PET measurement. In addition, they facilitate the use of an accurate model of the imaging process through the use of a system matrix. In theory, the use of an exact system model including all image degrading factors (c.f. Sec. 2.3) is needed for quantitatively accurate PET imaging. But, in practice, computation of all degrading factors can be very challenging, and therefore simplified system models are often used instead at the expense of a certain loss of resolution or precision in the final images.

A large and diverse set of iterative reconstruction techniques for PET exists today. The widely used *maximum likelihood (ML)* estimation approach selects the image that has the highest likelihood to explain the observed data. The likelihood objective function that is to be maximized in the iterative procedure can be derived from Poisson statistics. In the following, we will introduce the most popular algorithm for ML estimation, the *expectation maximization (EM)* algorithm. Since the *maximum likelihood expectation maximization (MLEM)* algorithm converges very slowly, modern scanners use an accelerated version, the *ordered subset expectation maximization (OSEM)* algorithm that is also presented in the following. It uses only a subset of the projection data in each iteration, resulting in a drastic speed-up.

Multiple MLEM/OSEM iterations need to be run for a sufficiently accurate image estimate, but because the ML problem in PET is ill-conditioned, the ML solution tends to get very noisy as the number of iterations increases. One possible solution is to stop the algorithm prematurely after a predefined number of iterations and to post-smooth the reconstructed image in order to make it more visually appealing. A more sophisticated method is to incorporate some form of a priori information about the image into the reconstruction process using the *penalized likelihood (PL)* — also called *maximum a posteriori (MAP)* — optimization approach. The implementation adds a prior function to the likelihood function to enforce the desired properties of the image. For example, if it is a priori assumed that neighboring voxels should have similar intensities, the resulting prior function effectively smooths the reconstructed image. However, smoothing also occurs across boundaries, resulting in a

loss of detail. Mathematical prior functions have been designed that smooth the image but preserve sharp edges. This is further discussed in Section 2.4.4.

Alternatively, priors can be designed to make use of morphological information provided by MR or CT images, assuming that there is a correlation between the underlying anatomy and the tracer distribution. Such anatomical approaches are especially attractive for integrated PET/MR scanners, as discussed in Section 2.4.5.

2.4.1 Statistical Iterative Reconstruction Algorithms

Unlike closed-form analytical inversion techniques, iterative algorithms begin with an initial image guess and successively improve the image estimate over multiple iterations. Often a simple uniform image is used as the starting point, and typical stopping criteria are maximum number of iterations or insufficient change in the objective function in between iterations. As formulated by Fessler [74], an iterative statistical algorithm is defined by the following five components:

1. *A parametrization of the image.* Given a finite set of basis functions $b_j(x,y), j = 1,\dots,J$, the continuous tracer distribution $f\colon V \subset \mathbb{R}^2 \to \mathbb{R}$ is approximated by

$$f(x,y) \approx \bar{f}(x,y) = \sum_{j=1}^{J} x_j b_j(x,y)$$

with parameter/coefficient vector $x = (x_1,...,x_J)$. The goal of image reconstruction is to estimate x. The more basis functions are used, the better the approximation, but also the higher the computational effort. Various choices have been suggested in literature including Fourier Series, Wavelets, and B-splines. Most often, however, the image is split into a fixed regular $(k \times k)$ grid of elements, called pixels (2D) or voxels (3D). In this case, b_j is defined as the indicator function

$$b_j(x,y) = \begin{cases} 1, & \text{if } (x,y) \text{ is inside voxel } j \\ 0, & \text{otherwise} \end{cases}$$

where $j \in S = \{1,\dots,k^2\}$.

2. *A system model matrix* $A \in \mathbb{R}^{I \times J}$. A relates the image vector $x = (x_1, x_2, ..., x_J)$ to the measured data vector $y = (y_1, y_2, ..., y_I)$ via the following set of linear equations

$$\bar{y} = E(y) = Ax, \tag{2.2}$$

where the elements a_{ij} are proportional to the probability that an emission arising from pixel j is detected by the LOR in sinogram bin i. A realistic system matrix comprises a geometric component that is typically based on a line integral or area of intersection model and a physics component that uses analytical models to calculate the effects of positron range, noncolinearity, DOI, and others. The matrix can be prohibitively large and it is therefore essential to exploit symmetries and sparseness. As an alternative to analytical calculations, Monte-Carlo techniques as well as actual measurements of point sources can be used to obtain the system matrix [99]. However, these alternatives are often restricted to small animal scanners due to their high complexity. For clinical whole body scanners, a simple geometric system matrix is often sufficient to obtain images of usable quality.

3. *A statistical model.* The model describes the statistical noise distribution of the count data. Emission data can be reliably modeled by the Poisson distribution, i.e.,

$$y_i \sim \text{Poisson}(\bar{y}_i), \quad \text{where} \quad \bar{y}_i = [Ax]_i = \sum_j a_{ij} x_j.$$

Assuming that the recorded events are statistically independent Poisson random variables, the probability of the data y given the expected value Ax is given by

$$p(y|x) = \prod_{i=1}^{I} p(y_i|x_i) = \prod_{i=1}^{I} e^{-\bar{y}_i} \frac{\bar{y}_i^{y_i}}{y_i!}.$$

The Poisson model only holds if the data are not corrected for background counts (r random and s scatter events). Thus, the mean data should be modeled as

$$\bar{y} = E(y) = Ax + r + s.$$

For pre-corrected data, a (weighted) Gaussian model is often applied instead.

4. *A cost function.* The cost function is integral to the algorithm, as it defines the criterion for an optimal solution vector $\hat{x}$. Most algorithms in PET are based on ML estimation that solve the maximization problem

$$\hat{x} = \arg\max_x L(x) \tag{2.3}$$

where the Poisson log-likelihood function $L(x)$, ignoring constants that are independent of x, is given by

$$L(x) = \log p(y|x) = \sum_{i=1}^{I} y_i \log \bar{y}_i - \bar{y}_i. \tag{2.4}$$

Since the ML estimate in Equation 2.3 can be very noisy due to the ill-conditioning of the inverse problem, a regularization term is often added to the likelihood function that stabilizes the solution. In a Bayesian framework, a prior distribution $p(x)$ that describes knowledge of the unknown image is used to improve the reconstruction, and the image is estimated by maximizing the posterior probability given by

$$p(x|y) = \frac{p(y|x)p(x)}{p(y)}.$$

The cost function of the *maximum a posteriori (MAP)* estimation approach is given by the logarithm of the posterior probability

$$\Psi(x) = \log p(y|x) + \log p(x) = L(x) + \log p(x), \tag{2.5}$$

which is the sum of the likelihood function of Equation 2.4, which evaluates the quality of the fit to the data, and of a prior term, which penalizes image estimates that are unlikely to meet the a priori assumption.

5. *An iterative algorithm.* The algorithm defines an equation how to successively update the image estimate until it maximizes the cost function or a defined stopping condition is reached.

2.4.2 MLEM algorithm

A closed-form solution for the Poisson model-based ML problem in Equation 2.3 does not exist. But the EM technique provides an iterative solution. It was first presented by Dempster *et al.* [65] in 1977 and later introduced to emission tomography by Shepp and Vardi [156].

A key requirement for EM is the definition of a complete but non-observable data set. In PET, the recorded data y_i can be regarded as incomplete as only the total number of events recorded for a given LOR i is known. A natural choice for complete data is therefore the number of events c_{ij} that are emitted from voxel j and recorded by detector pair i, where

$$y_i = \sum_{j \in J_i} c_{ij},$$

with J_i being the set of voxels that are intersected by LOR i. Using c_{ij}, a complete log-likelihood function $L_c(x)$ can be computed as

$$L_c(x) = \sum_{i=1}^{I} \sum_{j \in J_i} \left(c_{ij} \log(a_{ij} x_j) - a_{ij} x_j - \log(c_{ij}!) \right). \tag{2.6}$$

The EM approach can maximize $L_c(x)$ and in turn $L(x)$ relying on a two-step procedure:

- In the *E-step*, the conditional mean of $L_c(x)$ is computed, given the incomplete data y and a current estimate x^n. Inserting Equation 2.6 and exploiting linearity of the expectation value yields

$$\begin{aligned} E\left(L_c(x)|y,x^n\right) &= E[\sum_{i=1}^{I}\sum_{j\in J_i}\left(c_{ij}\log(a_{ij}x_j) - a_{ij}x_j - \log(c_{ij}!)\right)|y,x^n] \\ &= \sum_{i=1}^{I}\sum_{j\in J_i}\left(E[c_{ij}|y,x^n]\log(a_{ij}x_j) - a_{ij}x_j - E[c_{ij}!|y,x^n]\right). \end{aligned}$$

  With the conditional mean of the complete data calculated as

$$E(c_{ij}|y,x^n) = \frac{a_{ij}x_j^n y_i}{\sum_{l\in J_i} a_{il}x_l^n},$$

  the final expression is given by

$$E\left(L_c(x)|y,x^n\right) = \sum_{i=1}^{I}\sum_{j\in J_i}\left(a_{ij}x_j^n\frac{y_i}{\sum_{l\in J_i} a_{il}x_l^n}\log(a_{ij}x_j) - a_{ij}x_j\right).$$

- In the *M-step*, the conditional mean calculated in the E-step is maximized with respect to the image x. Setting the partial derivatives

$$\frac{\partial}{\partial x_j}E(L_c(x)|y,x^n) = \sum_{i\in I_j}\left(a_{ij}x_j^n\frac{y_i}{\sum_{l\in J_i} a_{il}x_l^n}\frac{1}{x_j} - a_{ij}\right)$$

  to zero, the final MLEM equation to compute the new image estimate x^{n+1} can be derived:

$$x_j^{n+1} = \frac{x_j^n}{\sum_{i\in I_j} a_{ij}}\sum_{i\in I_j} a_{ij}\frac{y_i}{\sum_{l\in J_i} a_{il}x_l^n} \tag{2.7}$$

Equation 2.7 can be interpreted as follows: First, given the current image estimate x^n, an estimate for the measurement is computed in a forward projection step $\sum_{l\in J_i} a_{il}x_l^n$. Then, the ratio of this estimate to the actual measurement y_i is calculated. If the ratio sinogram is not equal to 1, it is back projected to the image space. The resulting ratio image is then normalized by the sum $\sum_{i\in I_j} a_{ij}$ and multiplied with the current estimate x_j^n to obtain a new image update x_j^{n+1}. It can be proven that the MLEM algorithm increases the likelihood function in each iteration, i.e. $L_c(x^{n+1}) > L_c(x^n)$, and that x^n converges to $\hat{x}$.

The MLEM update formula 2.7 can be interpreted as a gradient descent algorithm:

$$x_j^{n+1} = \frac{x_j^n}{\sum_{i\in I_j} a_{ij}} \sum_{i\in I_j} a_{ij} \frac{y_i}{\sum_{l\in J_i} a_{il} x_l^n} = x_j^n + \frac{x_j^n}{\sum_{i\in I_j} a_{ij}} \sum_{i\in I_j} a_{ij} \left(\frac{y_i}{\sum_{l\in J_i} a_{il} x_l^n} - 1 \right)$$
$$= x_j^n + \frac{x_j^n}{\sum_{i\in I_j} a_{ij}} \frac{\partial}{\partial x_j} L(x)|_{x=x^n}$$

The MLEM algorithm can also be derived without statistical considerations but based on the optimization transfer principle using surrogate objective functions, as shown by de Pierro. This is further explained in Section 2.4.4.

2.4.3 OSEM algorithm

The OSEM algorithm is a modification of Equation 2.7 that achieves improved convergence by using only a subset of the projection data for each image update. Given a set of N_{Sub} disjoint subsets $S_1, S_2, \ldots, S_{N_{Sub}} \subset [1, 2, \ldots, I]$, the OSEM update equation is given by

$$x_j^{n,i} = \frac{x_j^{n,i-1}}{\sum_{i\in S_i} a_{ij}} \left(\sum_{i\in S_i} \frac{a_{ij} y_i}{\sum_{l\in J_i} a_{il} x_l^{n,i-1}} \right),$$

for $j = 1, \ldots, J$ and $i = 1, \ldots, N_{Sub}$. The variables n and i serve as indices for iterating over a complete OSEM cycle and all subsets, respectively, with $x^{n,0} = x^{n-1}$ and $x^{n,N_{Sub}} = x^n$. If only a single subset — containing all projection data — is used, the OSEM equation is identical to the EM algorithm.

2.4.4 Maximum a posteriori algorithms

Bayesian optimization as in Equation 2.5 requires definition of a prior function that reflects a priori assumptions on reconstructed image properties. The most widely used prior distribution is the Gibbs prior, which takes the following form:

$$p(x, \alpha) = \frac{1}{Z} e^{-\alpha R(x)},$$

where Z is a normalization constant, α is a regularization parameter that controls the strength of the prior term during optimization, and $R(x)$ is called the Gibbs energy function. The energy function $R(x)$ is usually defined as a weighted sum of potential functions ψ of the differences between pixels in a neighborhood N_j. It has the following form:

$$R(x) = \sum_{j=1}^{J} \sum_{k\in N_j} \omega_{jk} \psi(x_j - x_k),$$

where ω_{jk} is the weight of a given pixel k that is within the neighborhood N_j of voxel j. N_j is often chosen to contain the closest four or closest eight neighboring voxels.

Different choices for potential functions have been proposed in literature. A common choice in MAP reconstruction is the quadratic potential function $\psi(x) = \frac{x^2}{2\gamma^2}$ that tends to produce globally smooth images. Alternative choices, so-called edge-preserving priors, try to provide local smoothness but also preserve tissue boundaries, e.g., the Huber prior [127] that is quadratic for small differences in voxel intensities but becomes linear for larger differences, the Green prior [86] with $\psi(x) = \log\cosh(cx)$ and a user-defined parameter c, the Geman prior [83] with $\psi(x) = \frac{x^2}{\gamma^2+x^2}$ and a parameter γ to be specified; the Median root prior [18]. Another class of priors are anatomically guided prior functions, which are presented separately in Section 2.4.5.

In the following, we briefly outline algorithms that can be used to maximize the MAP objective function Ψ resulting from a Gibbs prior distribution, given by

$$\Psi(x) = L(x) - \alpha R(x). \tag{2.8}$$

Applying the EM approach to Equation 2.8, the E-step becomes

$$E\left(\Psi(x)|y, x^n\right) = \sum_{i=1}^{I}\sum_{j\in I_i}\left(a_{ij}x_j^n\frac{y_i}{\sum_{l\in J_i}a_{il}x_l^n}\log(a_{ij}x_j) - a_{ij}x_j\right) - \alpha R(x),$$

which needs to be maximized in the M-step that is written as

$$\frac{\partial}{\partial x_j}E\left(\Psi(x)|y, x^n\right) = 0$$

and results in the MAP-EM estimation formula

$$x_j^{n+1} = \frac{x_j^n}{\sum_{i\in I_j}a_{ij} + \alpha\frac{\partial}{\partial x_j}R(x)}\sum_{i\in I_j}a_{ij}\frac{y_i}{\sum_{l\in J_i}a_{il}x_l^n}. \tag{2.9}$$

2.4.4.1 One-Step-Late (OSL) algorithm

Green *et al.* [86] proposed a heuristic *one-step-late (OSL)* algorithm for computing a solution to Equation 2.9. It evaluates the derivate of the energy function at the current image estimate x^n rather than the unknown x. This results in the following OSL update equation:

$$x_j^{n+1} = \frac{x_j^n}{\sum_{i\in I_j}a_{ij} + \alpha\frac{\partial}{\partial x_j}R(x)|_{x=x^n}}\sum_{i\in I_j}a_{ij}\frac{y_i}{\sum_{l\in J_i}a_{il}x_l^n}$$

In practice, the algorithm works satisfactorily if α is not chosen too large, which would cause numerical problems.

2.4.4.2 De Pierro's MAP-EM

De Pierro proposed an alternative approach to solving Equation 2.9 based on the optimization transfer principle [113]. The basic idea of optimization transfer is to substitute the original objective function Ψ, that is often difficult to optimize, by a more tractable surrogate function $S(x|x^n)$ that approximates Ψ. Maximization of the surrogate function in the n-th iteration yields the new image update

$$x^{n+1} = \arg\max_x S(x|x^n). \tag{2.10}$$

The surrogate function is chosen to ensure that Equation 2.10 leads to a monotonic increase of Ψ and that the iterative scheme converges to the maximizer of Ψ. In De Pierro's work, a separable surrogate function for the likelihood function as well as the prior function was defined. The sum of both surrogate functions is again separable and defines the MAP surrogate for Ψ.

The following equation is used to obtain a surrogate function for the log-likelihood function L:

$$\bar{y}_i = \sum_j a_{ij} x_j = \sum_j \frac{a_{ij} x_j^n}{\sum_l a_{il} x_l^n} \left(\frac{\sum_l a_{il} x_l^n}{x_j^n} x_j \right)$$

By using convexity of $-\log$, the surrogate $S_L(x|x^n)$ can be defined as follows:

$$\begin{aligned} L(x) &= \sum_i \left[y_i \log \sum_j a_{ij} x_j - \sum_j a_{ij} x_j \right] \\ &\geq \sum_i \left[y_i \sum_j \frac{a_{ij} x_j^n}{\sum_l a_{il} x_l^n} \log \left(\frac{\sum_l a_{il} x_l^n}{x_j^n} x_j \right) - \sum_j a_{ij} x_j \right] \\ &= \underbrace{\sum_i y_i \sum_j \frac{a_{ij} x_j^n}{\sum_l a_{il} x_l^n} \log x_j - \sum_i \sum_j a_{ij} x_j}_{=:S_L(x|x^n)} + C \end{aligned}$$

By replacing L in Equation 2.3 with the separable surrogate function $S(x|x^n)$, the optimization problem becomes:

$$x_j^{n+1} = \arg\max_{x_j} \left(x_j^n \sum_i \frac{a_{ij} y_i}{\sum_l a_{il} x_l^n} \log x_j - x_j \sum_i a_{ij} \right)$$

It can easily be solved analytically and results in the MLEM update equation (c.f. Eq. 2.7).

Optimization transfer can also be applied to the prior term $R(x)$ of the MAP objective function. For example, for the quadratic prior function given by

$$R(x) = \frac{1}{2}\sum_{j=1}^{J}\sum_{k\in N_j}\frac{1}{2}\omega_{jk}(x_j - x_k)^2,$$

the separable surrogate function $S_P(x|x^n)$ can be defined as follows:

$$\begin{aligned} R(x) &= \frac{1}{2}\sum_{j=1}^{J}\sum_{k\in N_j}\frac{1}{2}\omega_{jk}(x_j + \frac{x_j^n - x_k^n}{2} - \frac{x_j^n - x_k^n}{2} - x_k)^2 \\ &\leq \underbrace{\frac{1}{2}\sum_{j=1}^{J}\sum_{k\in N_j}\frac{1}{2}\omega_{jk}(2x_j - x_j^n - x_k^n)^2}_{S_P(x|x^n)}. \end{aligned}$$

The resulting surrogate function $S(x|x^n) := S_L(x|x^n) + S_P(x|x^n)$ is again separable and defines a surrogate function for Ψ in 2.8 that can be maximized analytically.

2.4.5 Anatomically guided PET reconstruction

In the context of simultaneous PET/MR imaging, the PET reconstruction can be guided with a prior function that makes use of the simultaneously acquired, structural MR information. This potentially improves PET resolution and reduces noise. In the following a brief overview of different classes of such anatomical priors is given: approaches based on segmentation or edge detection of the anatomical image, information-based similarity measures, and local intensity-based approaches. The reader is referred to related work [24][142][71] for more extensive reviews of resolution modeling and anatomical priors.

Many early methods relied on a well-aligned anatomical image that often needs to be segmented in order to create tissue labels or extract boundary information. These methods include the work of Fessler *et al.* [75], Gindi *et al.* [84], Ouyang *et al.* [134], Lipinski *et al.* [116], and Baete *et al.* [21], who all restrict smoothing to within anatomical regions. However, identifying such regions through segmentation can be sensitive to noise, error prone, or even impossible in highly inhomogeneous areas such as many brain tumors. In order to deal with signal mismatches between the PET and MR image, the use of blurred weighting factors [75] or blurred anatomical label maps have been proposed [54][27]. Most of these methods use a quadratic regularization term with a weight that is determined based on the anatomical information.

More recent work obviates the need for anatomical image segmentation and, e.g., uses information theoretic functionals as a means to assess image correspondence between PET

and MR instead. Prior functions based on mutual information and joint entropy have been successfully incorporated into PET reconstruction [161][132][169][170], and more recently [162][178][182][171][120]. Such approaches do not exploit locality but merely correlate histogram intensities, which can introduce bias.

Local intensity-based approaches also avoid image segmentation. A prominent example is the so-called Bowsher prior as presented by Bowsher *et al.* [35], which is also used in parts of this work (especially in Chap. 4). In contrast to, e.g., the joint entropy prior, the Bowsher prior acts locally on the image and has been shown to be superior to other anatomical priors [182]. It is a position-dependent smoothing prior operating on a subset B_j of voxels within a given neighborhood N_j. Given a similarity measure and a fixed number of voxels $B < |N_j|$, a subset $N_j(a, B)$ for each voxel j of the B most similar voxels is selected, where similarity is according to the voxel's value in the anatomical image, $a_k, k \in N_j$. Conventionally, the absolute intensity differences are used as a similarity measure, and $N_j(a, B)$ contains all voxels fulfilling

$$|a_j - a_{k_1}| \leq \cdots |a_j - a_{k_B}|$$

and $|a_j - a_k| \geq |a_j - a_{k_B}| \; \forall k \in N_j \backslash N_j(a, B)$. Bousse *et al.* [33] presented a generalization of the Bowsher prior, which uses anatomical weighting functions instead of the original prior's binary neighborhood selection. Kazantsev *et al.* [107] proposed a non-locally weighted Bowsher prior that was shown to be more robust in case of signal mismatch between PET and MR information.

Recently published segmentation-free approaches suggest the use of *non-local means (NLM)* filters. These filters are recognized as effective image denoising filters in other applications and have been introduced originally by Buades *et al* [38]. In medical applications, NLM filters have been successfully applied post reconstruction [52]. When applied as a regularizer during image reconstruction [45][51], image quality has been found to be superior to traditional Gaussian filtering techniques. NLM methods that use anatomical side information such as CT or MR data have been demonstrated to improve image quality even further [44]. This is also true with respect to robustness to mismatch between the PET and the anatomical data set [129]. Alternative methods have been proposed that are based on anisotropic diffusion [106][43][108], level sets [46][70], or kernel functions [189].

Another question that arises, is how the anatomical image and the radiotracer's distribution relate. MRI in this context is a powerful and highly flexible instrument. A plethora of pulse sequences combined with various contrast agents can produce a wide range of images, revealing anatomical information for different types of tissue but also, for example, information on blood flow or diffusion and perfusion-based information. Some of the most commonly

found image types are shown in Figure 2.10, but both the development of new sequences as well as their relation to PET are subject to active research.

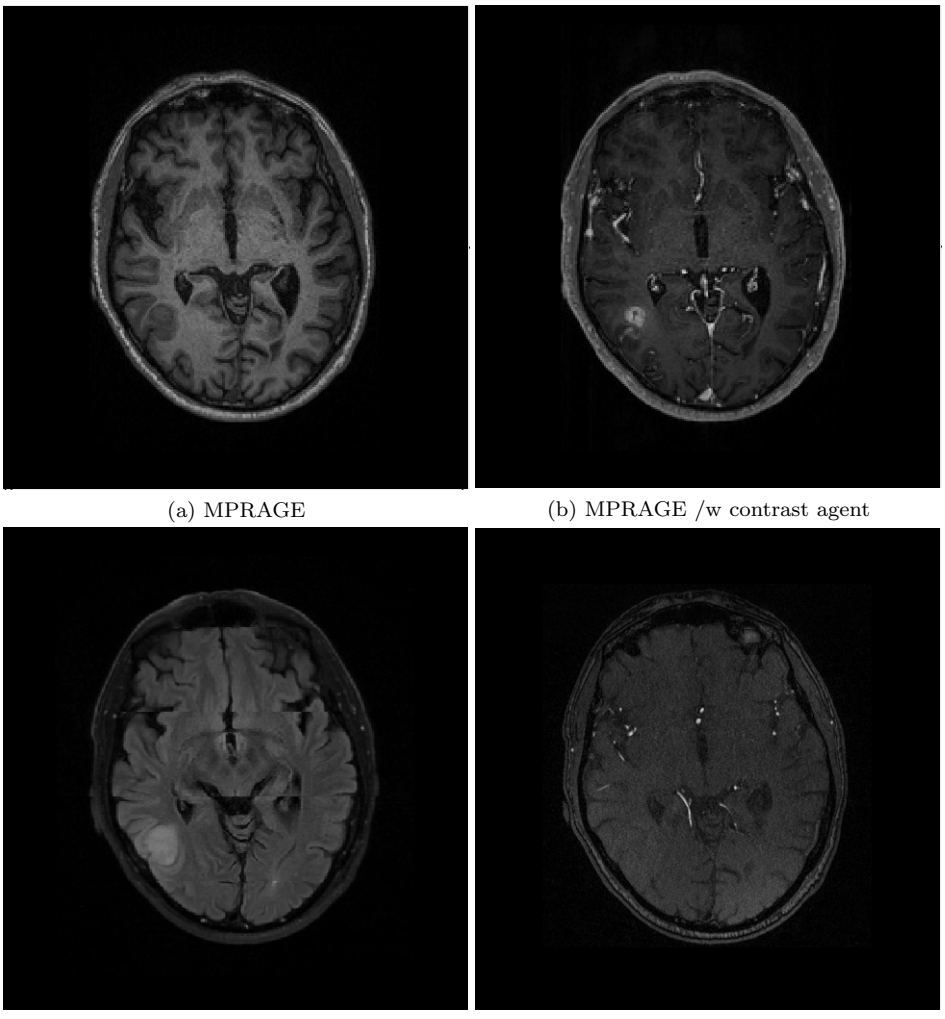

(a) MPRAGE (b) MPRAGE /w contrast agent

(c) T2 dark fluid (d) TOF

Figure 2.10: Examples of different MR images: (a) magnetization-prepared pulses and rapid gradient-echo (MPRAGE) T1-weighted sequence, yielding good tissue contrast; (b) MPRAGE with contrast agent, improving contrast in lesion; (c) T2-weighted image, fluid is dark; (d) time-of-flight (TOF) image revealing angiographic detail.

2.5 Dynamic PET reconstruction

Dynamic acquisition of PET data opens possibilities for quantitative data analysis beyond those of static PET images, where the acquired data are averaged over the whole scan duration and quantification is based on a single static image. Dynamic PET acquisition can produce a sequence of images, which are typically obtained by independent reconstruction of data binned into frames (e.g., 10 frames of 5 minutes for a 50 minute scan). This captures the dynamics of the tracer as it is injected into the body and yields *time activity curves*

(TACs), either per voxel or for larger *regions of interest (ROIs)*. These dynamics can be analyzed and quantified via tracer kinetic modeling, which extracts informative pharmacological parameters that can lead to improved diagnosis and treatment of different types of cancer [167]. The kinetic analysis requires an appropriate, parameterized kinetic model that a curve fitting procedure fits to a given TAC in a post-reconstruction step. However, due to poor count statistics in independent, short duration frames, TACs are often very noisy, which in turn leads to a high level of noise in the fitted parameters.

Several approaches have been developed to handle the noise better and to obtain high quality parametric images from voxel-wise curve fitting. Many dynamic methods seek to reduce noise in the dynamic image sequence and can be classified by the temporal basis functions they use, e.g., B-splines [148], [149], [130], [180], wavelets [181], principle component analysis [196]. In recent years the incorporation of the pharmacokinetic model directly into the reconstruction model, referred to as *direct parametric image reconstruction (DPIR)*, has drawn much attention [176]. Direct reconstruction combines reconstruction and model fitting in a single step, enabling direct reconstruction of static parametric images that are superior in bias-variance characteristics to the classical post-reconstruction fitting approach [187].

In the following we give a brief introduction into kinetic modeling and present one of the most widely used pharmacokinetic models, the *two-tissue compartment (2TC)* model, as well as standard fitting procedures. For a more extensive introduction into tracer kinetic modeling in PET, we refer to [40]. We conclude this chapter with a brief presentation of the dynamic data model and the resulting objective function in DPIR.

2.5.1 Tracer kinetic modeling

Tracer kinetic modeling uses a mathematical model in order to describe the kinetics of the radiotracer inside the patient's body. A special class of models are so-called compartment models that comprise one or more compartments that each relate to a different anatomical, physiological, or biochemical state of the radiotracer. The transition of the radiotracer between these compartments is described by rate constants, the kinetic parameters. The parameters are estimated using a fitting procedure based on mathematical fitting algorithms.

2.5.1.1 Two-tissue compartment model

The *two-tissue compartment (2TC)* pharmacokinetic model is suitable for a wide range of radiotracers, e.g., [^{18}F]FDG, [^{18}F]FET, or [^{18}F]FLT. As illustrated in Figure 2.11, it consists of a free blood compartment and two tissue compartments, where the function $C_p(t)$, the *arterial input function (AIF)*, represents the concentration of tracer in blood, and $C_1(t)$ and

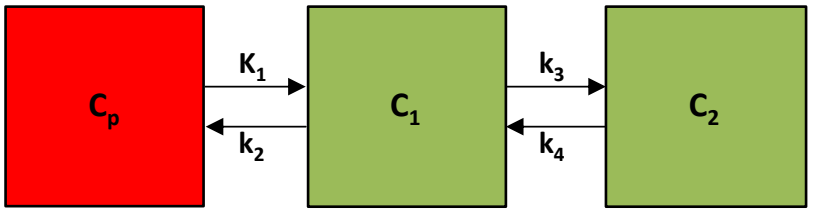

Figure 2.11: 2TC model with rate constants K_1, k_2, k_3, k_4 describing the exchange of tracer between the blood, and the tissue compartments C_1 and C_2.

$C_2(t)$ the concentration in tissue over time. The exchange of tracer is described by the rate constants K_1, k_2, k_3, k_4: the arterial blood enters the first compartment at a forward rate K_1, from where a fraction of the tracer diffuses back to the blood (k_2); another fraction enters into the second tissue compartment at a forward rate k_3, where again a portion of the tracer is either transported back at a rate k_4, or remains trapped (i.e., $k_4 = 0$).

Mathematically, the 2TC model can be represented by the following set of differential equations:

$$\frac{dC_1(t)}{dt} = K_1 Cp(t) - (k_2 + k_3)C_1(t) + k_4 C_2(t)$$
$$\frac{dC_2(t)}{dt} = k_3 C_1(t) - k_4 C_2(t)$$

The analytical solution to this set of differential equations can be derived, e.g., using the Laplace transform and is given by

$$C_1(t) = \frac{K_1}{\alpha_2 - \alpha_1}\left((k_4 - \alpha_1)e^{-\alpha_1 t} + (\alpha_2 - k_4)e^{-\alpha_2 t}\right) \otimes C_p(t)$$
$$C_2(t) = \frac{K_1}{\alpha_2 - \alpha_1}\left(k_3 e^{-\alpha_1 t} - k_3 e^{-\alpha_2 t}\right) \otimes C_p(t)$$

with $\alpha_{1,2} = \frac{1}{2}(k_2 + k_3 + k_4 \mp \sqrt{(k_2 + k_3 + k_4)^2 - 4k_2 k_4})$.

The signal that is measured by PET is the total concentration of the radiotracer in both compartments $(C_1(t) + C_2(t))$ and the fractional blood volume in the tissue V_B. Thus, the predicted model curve $C_T(t)$ is given by

$$C_T(t) = \frac{K_1}{\alpha_2 - \alpha_1}\left((k_4 - \alpha_1 + k_3)e^{-\alpha_1 t} + (\alpha_2 - k_4 - k_3)e^{-\alpha_2 t}\right) \otimes C_p(t) + V_B C_p(t)$$

that is the convolution of the AIF $C_p(t)$ with the system's *impulse response function (IRF)*, where

$$IRF(t) = \frac{K_1}{\alpha_2 - \alpha_1}\left((k_4 - \alpha_1 + k_3)e^{-\alpha_1 t} + (\alpha_2 - k_4 - k_3)e^{-\alpha_2 t}\right).$$

Conventionally, the AIF is obtained by measurement using arterial catheterization. Because this procedure can be tedious, time-consuming, and uncomfortable for patients, noninvasive, image-based alternatives to estimate the arterial input function have been investigated extensively [202]. PET/MR imaging can facilitate this task, as MR images can be generated (such as the angiographic image in Fig. 2.10d) that readily allow segmentation of blood pool regions such as the aorta or the carotid arteries [150] [79] [164] [102].

2.5.1.2 Parameter estimation

The kinetic model $C_T(t)$ is determined by a set of parameters, e.g., $\{K_1, k_2, k_3, k_4, V_B\}$ for the 2TC model. Given the AIF and the measured data C_i sampled at N time points $t_i, i = 1, \ldots, N$, the model parameters that best explain, or fit, the data need to be estimated. In order to evaluate the quality of the fit, a criterion, also called objective function, must be selected. The most commonly used criterion is the least squared criterion that minimizes the sum of squared residuals

$$\sum_{i=1}^{N} (C_T(t_i) - C_i)^2$$

between the model's predicted values $C_T(t)$ and the actual measurements C_i. Often a weighted sum of the residuals

$$\sum_{i=1}^{N} w_i (C_T(t_i) - C_i)^2$$

is minimized instead by assigning weighting factors w_i to each residual. This allows to control the relevance of each data point for the final parameter estimation. It can be shown that weights chosen to be inversely proportional to the variance of the measurement error are optimal.

2.5.2 Parametric image reconstruction

Direct parametric image reconstruction methods incorporate a pharmacokinetic model C_T directly into the reconstruction process. This enables the reconstruction of parametric images directly from the dynamic sinogram data $\{y_m,\ m = 1, \ldots, M\}$ that are binned into M time frames. The image intensity $x_m(\theta_j)$ in voxel j at time frame m is predicted by the model curve $C_T(t, \theta_j)$ evaluated for the parameter vector $\theta_j \in \mathbb{R}^P$ at voxel j. The kinetic parameters are then related directly to the predicted mean sinogram data $\bar{y}_m(\theta) = (\bar{y}_{1m}, \ldots, \bar{y}_{Im})^T \in \mathbb{R}^I$ using the system model in 2.2 by the following equation:

$$\bar{y}_{im}(\theta) = \sum_{j=1}^{J} a_{ij} x_m(\theta_j) + n_{im}$$

ML estimation finds the solution $\hat{\theta}$ by solving the following optimization problem

$$\hat{\theta} = \arg\max_{\theta} L(y|\theta),$$

where the dynamic log-likelihood function $L(y|\theta)$, ignoring constants that are independent of θ, is given by

$$L(y|\theta) = \sum_{m=1}^{M} \sum_{i=1}^{I} y_{im} \log \bar{y}_{im}(\theta) - \bar{y}_{im}(\theta).$$

DPIR has been developed for various pharmacokinetic models, including linear models such as the Patlak model [184], [175] and, more recently, more complex indirect models such as the 2TC model [104], [185], [187]. DPIR has proven to be successful in reducing noise in parametric images, clearly outperforming indirect post-reconstruction kinetic modeling results [188]. However, little research is available on the use of anatomical information to increase the quality of parametric images even further. In Chapter 4 of this thesis, we develop a new DPIR reconstruction approach that leverages anatomical MR data for an anatomically-driven smoothing prior.

Chapter 3

Study of positron range and spatially-variant resolution recovery for the Biograph mMR Scanner

This chapter is based on work previously published in the IEEE Transactions on Nuclear Science [1] (© 2012 IEEE. Reprinted, with permission, from R. Kraus *et al.*, IEEE Trans Nucl Sci 2012; 59(5):1900 - 1909). The author of this thesis is the main contributor to that publication and has conducted all relevant research.

—

Positron range is a factor that limits the spatial resolution of PET in general. In a PET/MR scanner, the impact of the *magnetic field (MF)* on positron range must be considered in addition. The Lorentz force acts perpendicular to the MF and therefore limits the range of positrons flying in this direction (x-y plane). This has two effects:

- The positron range in the x-y plane is reduced, effectively improving spatial resolution.
- The positron range in the z plane is unaffected. However, due to the reduced range in the x-y plane, higher concentrations occur in the z direction, especially at tissue borders.

We investigated positron range and its effect on imaging with the new Biograph mMR 3 T whole-body PET/MR system quantitatively and with respect to different underlying tissue

types. Positron range simulations were performed for ^{82}Rb and ^{68}Ga in homogeneous and non-homogeneous configurations of soft and lung tissue using Geant4. It is shown that existing positron range correction methods are insufficient and that artifacts can occur.

We consequently present an algorithm that addresses these additional challenges imposed by PET/MR and that reduces artifacts. It is part of our 3D MLEM reconstruction framework (c.f. Chap. 5) and incorporates novel correction kernels that compensate for the effect of positron range. We developed new methods for selecting and adapting such correction kernels based on the MR-derived attenuation map and pre-simulated positron range data. The methods were evaluated using *Monte Carlo (MC)* simulation data on a model of the mMR system including the 3 T MF and the MR body coil.

3.1 Positron Range in an integrated PET/MR scanner

Positron range can be a significant factor that limits PET image resolution, independently of other physical effects such as inter-crystal scattering and non-collinearity – as well as size of the PET detectors, and patient motion [115]. Emitted positrons follow a tortuous path through human tissue, on which they lose their kinetic energy through Coulomb interactions with electrons. Eventually they annihilate with an electron. In earlier works, experiments have been conducted to measure positron range for different medically relevant positron emitters in water [50, 66, 136]. More recently, MC simulations were employed to estimate the annihilation distribution of positrons [42, 115, 163].

The effect of positron range appears as a blurring in the reconstructed image. The extent of the blurring depends on the distance positrons travel, i.e., mainly the following three factors:

- Positron range depends on the emitted positron energy spectrum of the administered radioisotope. The higher the energy of the emitted positrons, the longer the path length prior to annihilation. The energy spectrum of a radioisotope with a maximum kinetic energy E_{max} of the emitted positron and an atomic number Z can be calculated analytically by

$$N(E)dE = (E_{max} - E)^2 W p F(Z, W) \tag{3.1}$$

with $N(E)$ representing the number of positron decays at a certain emission energy E in MeV and the following definitions for

$$W = 1 + E/0.511$$
$$p = \sqrt{(W^2 - 1)}$$
$$\eta = \frac{-ZW}{137p}$$
$$F(Z, W) = \frac{2\pi\eta}{1 - \exp(-2\pi\eta).}$$

The range of positron is larger for ^{82}Rb with $E_{max} = 3.34$ MeV than for ^{68}Ga with $E_{max} = 1.89$ MeV. The theoretical energy spectra computed from eq. (3.1) for a selection of most common radioisotopes, e.g., ^{68}Ga, ^{82}Rb and ^{18}F are plotted in Figure 3.1. As can be seen, positron range is most significant for ^{82}Rb, which is used clinically for cardiac imaging, and ^{68}Ga, which is used for tumor imaging.

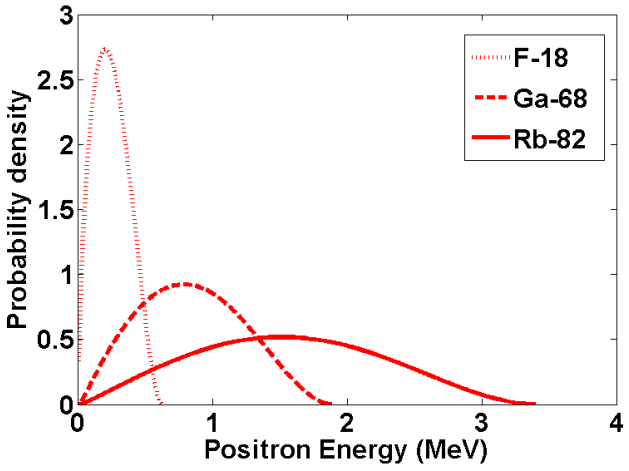

Figure 3.1: Energy distribution for ^{18}F, ^{68}Ga, and ^{82}Rb.

- Positron range also depends on the composition of the tissue that the positron transverses [159, 163]. It varies depending on the electron density of the tissue medium. The higher the density the shorter is the range of the positron. As such, positron range in air or lung tissue with a mass density of 0.3 g/cm^3 is more pronounced than in bone or soft tissue with a mass density of 1.0 g/cm^3.

- Positron range varies with the existence and strength of a MF, as is the case for integrated devices that combine PET with MR imaging [138], [201] such as the Siemens Biograph mMR [63]. This is due to the Lorenz force that any homogeneous MF exerts on charged particles given by

$$\vec{F}_{LOR} = q\vec{V} \times \vec{B}$$

as the cross product of the velocity $\vec{V}$ of the charged particle and the MF $\vec{B}$ where q denotes the charge of the particle. It is proportional to the charge q and and the velocity $\vec{V}$ and always perpendicular to both $\vec{V}$ and $\vec{B}$. Thus, the formula implies hat the force on a stationary charged particle or a charge moving parallel or anti-parallel to the direction of the MF is zero. The force is maximal if the velocity of the charged particle is perpendicular to the MF. This results in reduced positron range in the transverse (x-y) plane and potentially in improved PET image resolution.

3.2 Related Work

It is the seemingly positive effect of the MF on PET resolution explained in the preceding section that partially motivated the design of combined PET/MR scanners in the first place. Raylman *et al.* [145] investigated the percentage of improvement of different MF strengths varying from 0 T, 3 T and 10 T, on PET by MC simulation. In accordance with other works [91, 98, 163, 197], they found that the higher the MF strength, the stronger the gain in resolution becomes. For ^{120}I, Herzog *et al.* recently proved a reduced positron range due to the presence of a MF based on measured brain phantom data from the 9.4 T MR-BrainPET [93]. However, according to [163] and to our own findings, positron range is unaffected or even enlarged slightly along the direction of the MF. Severe misplacement artifacts along the direction of the MF can be observed in low density mediums [111]. This necessitates new correction approaches for PET/MR scanners.

Several correction approaches have been proposed to remove the blurring due to positron range in standalone PET devices. Fourier-deconvolution techniques have been applied in [67] and [90]. Bai *et al.* [23] corrected for positron range during iterative MAP reconstruction. In [117] the authors consider positron range in the system matrix. In this work, a positron range correction kernel is applied within 3D MLEM reconstruction.

Comprehensive correction must address tissue dependency. In our approach, this translates to the application of positron range correction kernels that depend on the underlying tissue for each voxel. In PET/MR imaging the tissue information can be derived from the MR-attenuation map, which is segmented into fat, lung, soft tissue, and air. Related approaches have obtained the underlying tissue type from a segmented CT image [19, 39].

Especially relevant are inhomogeneous regions along tissue boundaries, e.g., between lung and soft tissue. Here, inappropriate correction kernels can decrease image quality and cause artifacts. But the design of positron range correction kernels is more difficult in this case.

Ideally, the local tissue configuration would be considered for each voxel individually, generating the appropriate kernel by simulation. Unfortunately, this is too demanding for practical applications. The problem was addressed analytically by [19] and [22]. Alessio *et al.* [19] used an analytical tissue-dependent model and computed positron range in inhomogeneous media based on averaged fit parameters. Bai *et al.* [22] modeled the annihilation distribution at tissue borders by convolution of homogeneous tissue-dependent range kernels. However, neither approach considers the effect of the MF and leverages precise positron range data derived from MC simulations.

3.3 Materials and Methods

We investigated positron range and its effect on image resolution for the Biograph mMR both in homogeneous soft tissue and lung regions as well as near tissue boundaries. Since other resolution-degrading effects (e.g., motion) are independent of positron range, we assumed otherwise corrected data and focused entirely on positron range and its correction.

Positron range was determined and analyzed for two exemplary high-energy nuclides (^{82}Rb and ^{68}Ga) using MC simulation. The effect of the 3 T MF as it is present in the hybrid PET/MR system was considered for all configurations. A 3D MLEM algorithm was used to determine the impact on image resolution. The algorithm was modified to correct for positron range, especially along the MF in the z-direction. It was used to assess the potential of positron range correction for homogeneous and inhomogeneous tissue regions. In addition, tissue-specific kernel selection and generation was examined. We used a reduced set of pre-simulated positron range distributions to generate positron range kernels for arbitrary local tissue configurations, as given by MR-derived attenuation maps in PET/MR.

3.3.1 Positron Range Simulations

The Geant4 Monte Carlo simulation package [17, 82] was used to calculate the annihilation distribution of positrons in different tissue media. The developed simulation model includes the following physical processes: positron decay, multiple scattering, ionization, Bremsstrahlung, and electron annihilation. In addition, the static 3 T MF along the z-direction of the Biograph mMR was considered using the MF class provided in Geant4. As a reference, the simulations were also conducted with the MF switched off.

Positron range simulations were performed for the high energy positron emitters ^{82}Rb and ^{68}Ga in lung and soft tissue media. The different chemical compositions of lung (mass density 0.3 g/cm^3) and soft tissue (mass density 1.0 g/cm^3) were chosen according to the

International Commission on Radiological Protection (ICRP) [97] as defined in the *National Institute of Standards and Technology (NIST)* database [15].

Knowledge of the positron energy spectrum is required for the calculation of the positron annihilation distribution of specific radioisotopes. It can be calculated from the maximum kinetic energy E_{max} of the emitted positrons. Given E_{max} and the atomic number Z of the positron emitter, the energy distribution can be described by the following analytical expression [57, 92]:

$$N(E)dE = (E_{max} - E)^2 WpF(Z, W)$$

where $N(E)$ represents the number of positron decays at a certain emission energy E in MeV. The energy $E_{max} = 3.34$ MeV was used for ^{82}Rb and $E_{max} = 1.89$ MeV for ^{68}Ga. The resulting energy distribution is shown in Figure 3.1. It was sampled and included in the model using the Geant4 G4 *GeneralParticleSource (GPS)* with linear interpolation.

The simulation traces the trajectory of the emitted positrons until the positron annihilates with an electron or escapes from the world volume. In total, 5 million annihilation events were simulated per configuration. The annihilation end point coordinates x, y, z of each event were saved to a file.

Both homogeneous and inhomogeneous tissue regions were modeled in Geant4:

- *Homogeneous region* Spherical soft and lung tissue phantoms were created with $r = 8$ cm, chosen sufficiently large as to cover the maximal positron range of ^{82}Rb. A point source was placed in the center of the phantom.
- *Inhomogeneous regions* The region comprised two adjacent cubes of $10 \times 10 \times 10$ cm^3 filled with lung and soft tissue. The regular, solid tissue border appears in the center, perpendicular to the z-axis. Positron annihilations were simulated for different off-border positions of the source along the z-axis. The sources were set at $x = 0$ mm, $y = 0$ mm, and $z \in \{\pm 1, \pm 3, \pm 5, \pm 7, \ldots, \pm 23 \text{ mm}\}$.

Figs. 3.2a and 3.2b show the spatial distribution of positron annihilation for ^{82}Rb without a MF (0 T) in a homogeneous region. The annihilation endpoint coordinates are visualized as a 3D point cloud centered in the figures. In addition, the 2D histograms on each plane, x-y, y-z, and z-x, are plotted. It can be observed that both media show an isotropic distribution with increased density towards the center. However, positron range is significantly dependent on the underlying tissue: Positrons in lung may cover a longer path than in soft tissue because of the lower material density, resulting in a more widespread distribution. Figure 3.3 demonstrates the influence of the mMR's static 3 T MF in z-direction. The mean distance of the positrons is reduced in the x/y plane. This is due to the fact that the MF exerts Lorentz

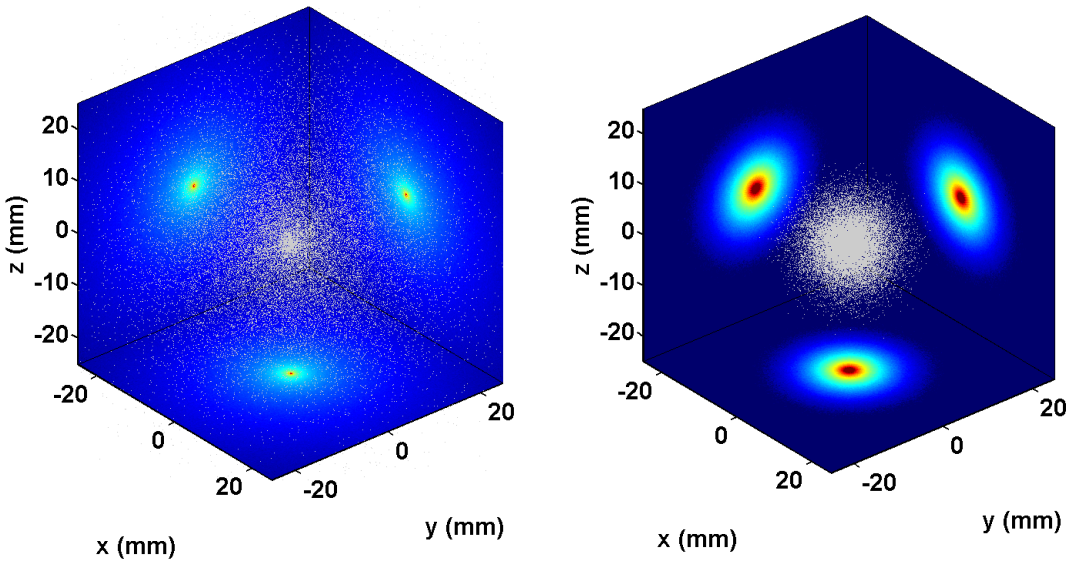

Figure 3.2: Simulated annihilation endpoint coordinates for a ^{82}Rb point source placed in homogeneous (a) lung tissue and (b) soft tissue at 0 T static MF in z-direction.

forces on charged moving particles such as positrons, and this force is directed orthogonally to the MF. The result is a narrower and more concentrated point cloud.

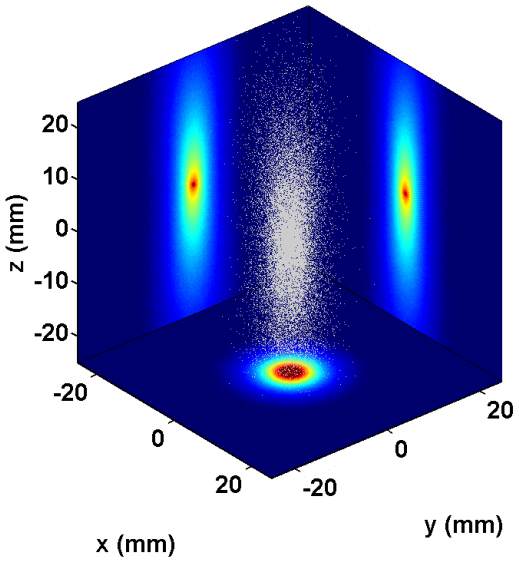

Figure 3.3: Simulated annihilation endpoint coordinates for a ^{82}Rb point source placed in homogeneous lung tissue at 3 T static MF in z-direction.

However, the influence of the MF makes the positron range along the z-axis much more prominent. A histogram of the annihilation endpoint coordinates within a 1×1 mm^2 neighborhood along the z-axis is shown in Figure 3.4. Both the curves for 0 T and 3 T are cusp shaped, but the number of annihilation events per sample increase throughout the curve as the 3 T MF is applied. This increase is due to the additional events moving

into the profile from the x-y plane, where the range of particles is limited by the MF. The result is an increased peak and a slower decay of the curve; the *full width at half maximum (FWHM)* increases by 31%. As the z-movement of the particles is unaffected by the MF, the maximum range and maximum extension of the cloud in z-direction remains unchanged.

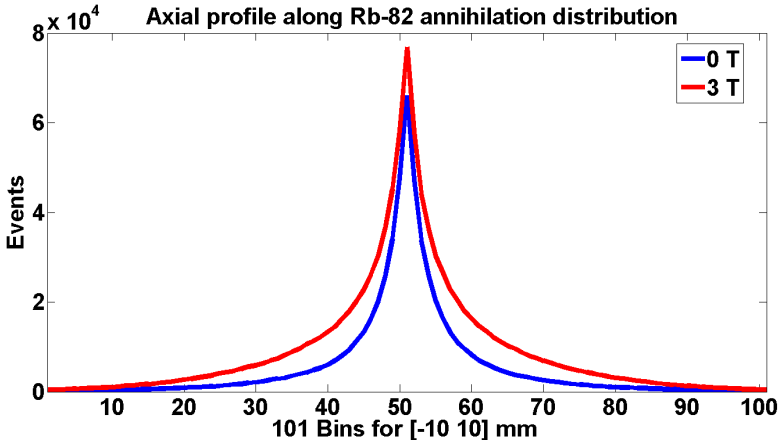

Figure 3.4: Axial profile of the annihilation endpoint coordinates within a 1×1 mm^2 neighborhood along the z-axis for ^{82}Rb at 0 T and 3 T in soft tissue.

Positron range exhibits a complex behavior at tissue borders, e.g., between lung and soft tissue, and especially for high energy radioisotopes. The inhomogeneous nature of the positron range kernel at 3 T becomes apparent in Figure 3.5, where a ^{82}Rb point source was placed in lung tissue with a soft tissue border at 9 mm distance from the source position in z-direction. Due to the increased positron range in z-direction in the presence of the MF and the large positron range in lung tissue, annihilation events concentrate at the distant soft tissue border, where higher material density is slowing down the positrons.

Table 3.1 summarizes the mean positron range in total for all three dimensions (3D) and in single dimensions orthogonal to (x/y-directions) and along (z-direction) the 3 T MF. Our simulated values are in agreement with the 3 T simulation results presented in [163]. It can be observed that positron range is much more relevant in z-direction, namely more than four times the range in x/y-direction for lung and ^{82}Rb and almost four times for lung and ^{68}Ga. Also, the dependency on the tissue type is much more relevant in z-direction. Moving from soft tissue to lung, e.g., for ^{82}Rb, the mean range increases by only 23 % in x/y-directions, but by 226 % in z-direction.

3.3.2 Reconstruction Framework with Positron Range Correction

Positron range correction was introduced into a 3D MLEM reconstruction framework. The effect of positron range was modeled as a local diffusion of the estimated activity image.

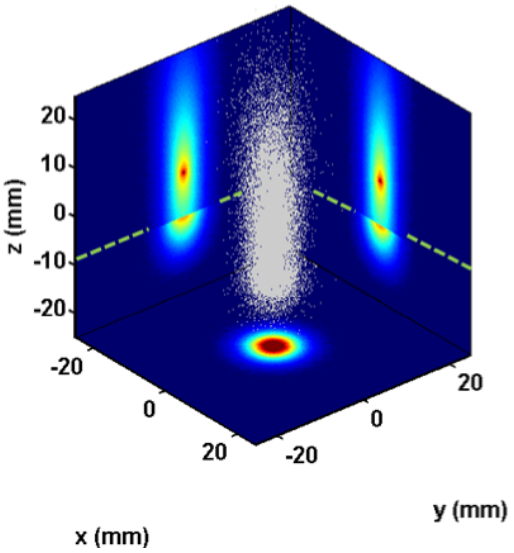

Figure 3.5: Simulated annihilation endpoint coordinates for an ^{82}Rb point source set at the origin in lung tissue (above dashed green line) with a 9 mm distant soft tissue region in z-direction (below dashed line) at 3 T static MF in z-direction.

Table 3.1: Mean Positron Range for different Tissues and Nuclides at 3 T

	Mean 3D range (mm)		**Mean 1D range at x (or y) (mm)**		**Mean 1D range at z (mm)**	
	Soft	**Lung**	**Soft**	**Lung**	**Soft**	**Lung**
^{68}Ga	2.12	4.93	0.94	1.24	1.28	4.23
^{82}Rb	4.01	9.86	1.58	1.95	2.73	8.90

Given a sinogram, storing measured events along all *lines of response (LORs)* of the scanner, and given a geometric system probability matrix containing the probability of an event in voxel being detected in LOR, the activity in voxel j was iteratively estimated as follows:

$$x_j^{n+1} = x_j^n \sum_{i=1}^{I} \left(\frac{a_{ij}}{\sum_{i'=1}^{I} a_{i'j}} \right) \frac{y_i}{\left(\sum_{j'=1}^{J} a_{ij'} \tilde{x}_{j'}^n \right)}$$

A local diffusion operation was applied to the estimated activity image x given by

$$\tilde{x}_{j'} = \sum_{h \in \mathcal{N}_{j'}} x_h g_{hj'}$$

where $g_{hj'}$ are the diffusion weights from the voxels in the neighborhood $\mathcal{N}_{j'}$ towards the current voxel j'. Here, the diffusion kernel g was chosen to reflect the effect of positron range on the activity image, i.e., it must represent the localized annihilation distribution for each

voxel in the imaged object. In each iteration, the algorithm spreads the activity estimate in voxel j' towards the neighboring voxels by weighting the voxel's activity value with the corresponding diffusion weights defined in its kernel. It applies this operation prior to forward projection, i.e., multiplication of the image estimate with the system matrix. This leads to a more accurate description of the expected measurement in relation to the real, measured sinogram y. Thus, the algorithm can update the reconstructed image more accurately. We note that the algorithm only applies positron range modeling in the projection operation. Such an approach was successfully used in [39].

Alternatively, the effect of positron range could be included directly in the system matrix. However, our chosen approach allows to flexibly selecting appropriate, localized kernels depending on the properties of the underlying tissue. Since reconstruction is thus decoupled from the choice of the correction kernels, different kernel generation and selection methods can be implemented and assessed in the following.

3.3.3 Positron Range Correction Kernels

The positron range annihilation distribution is tissue-specific and can easily extend over several voxels even in medium-resolution clinical scanners. Thus the proper selection of the correction kernel must take into account surrounding tissue configuration. Ideally, the correction kernels are determined via precise simulations for each voxel of the phantom. However, this is not practical for phantoms of relevant size.

Instead we propose to select pre-simulated kernels or to construct kernels from pre-simulated data, depending on the tissue type of each voxel and of its neighbors. The advantage of using MC simulated kernels is that the anisotropic effect of the MF can be incorporated. In addition, the complex behavior of the positrons at tissue borders can be more precisely described.

The required information on the underlying tissue type can be obtained from an MR-based attenuation map, e.g., as it is available in the mMR software. It is generated based on a Dixon chemical shift sequence and contains four segmented tissue regions: fat, lung, soft tissue, and air [121]. Therefore, it can be directly used as a look-up table for the underlying tissue of each image voxel. The accuracy of the attenuation map is assumed to be sufficient, as approaches to improve segmentation [121] and co-registration [89] for PET/MR are available but out of the focus of this work.

Pre-simulation of all possible tissue configurations is not feasible even for moderately sized kernels and few different tissue types. As a consequence, exact pre-simulation is only practical for a limited number of homogeneous or regular areas. In this context, we implemented and evaluated two correction strategies for positron range based on MC simulations.

Spatially-Variant Approach: This method selects between pre-simulated kernels for different homogeneous tissue regions, e.g. lung and soft tissue. The choice for each image voxel is dependent on the underlying tissue type as specified in the attenuation map. The approach is illustrated in Figure 3.6 for a given tissue distribution. It is ideal for homogeneous areas, but inaccurate at tissue borders. For the generation of the kernels, the simulated annihilation end-point coordinates for a point source (see Section 3.3.1) were binned into a 3D histogram with bin size equal to the reconstructed image's voxel size and normalized.

Generalized Approach: Realistic phantoms exhibit borders with arbitrary tissue configuration and, consequently, a complex annihilation distribution. This approach approximates the ideal correction kernel by generalizing from a limited number of pre-simulated reference data sets that incorporate tissue borders. These data sets were binned as in the spatially-variant approach. The kernels are parametrized with tissue information from the attenuation map, and (for each voxel in the image) each of the kernel's coefficients is composed individually.

The focus is put on correcting for inhomogeneities in z-direction, where both positron range and tissue specifics are most relevant. The main assumption is that the positron range distribution in inhomogeneous parts foremostly depends on the distance and on the relative position of the respective coefficient to the source and to the tissue border. The algorithm is prepared as follows: 1) Pre-simulate and bin positron range distributions for regions with regular, solid tissue borders perpendicular to the z axis for varying distances (z-offset) for a point source (see Fig. 3.7 (middle)). 2) Pre-determine all possible line connections from the kernel's center to the coefficients located on the surface of the kernel. The determination of the positron range distribution kernel at an image voxel at runtime is sketched in Figure 3.7 (left) and as follows:

- Evaluate all line connections for tissue changes starting from the kernel's center.
- If a border is found along a line, calculate the corresponding z-offset and propagate it to all coefficients of that line.
- Once all lines are evaluated, use the averaged z-offset at each coefficient as a lookup index into the pre-simulated data sets and use the value corresponding to the coefficient's position.

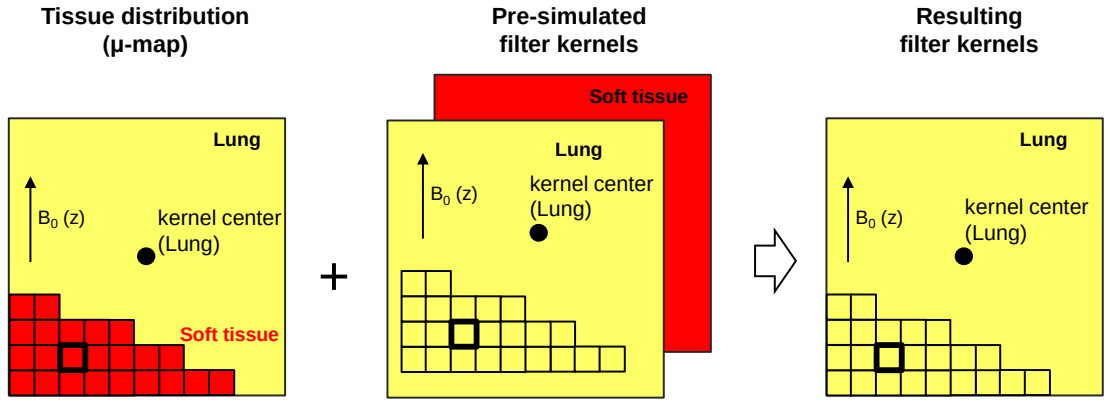

Figure 3.6: Spatially-Variant Approach: a pre-simulated homogeneous tissue kernel is selected according to the underlying tissue type of the current voxel.

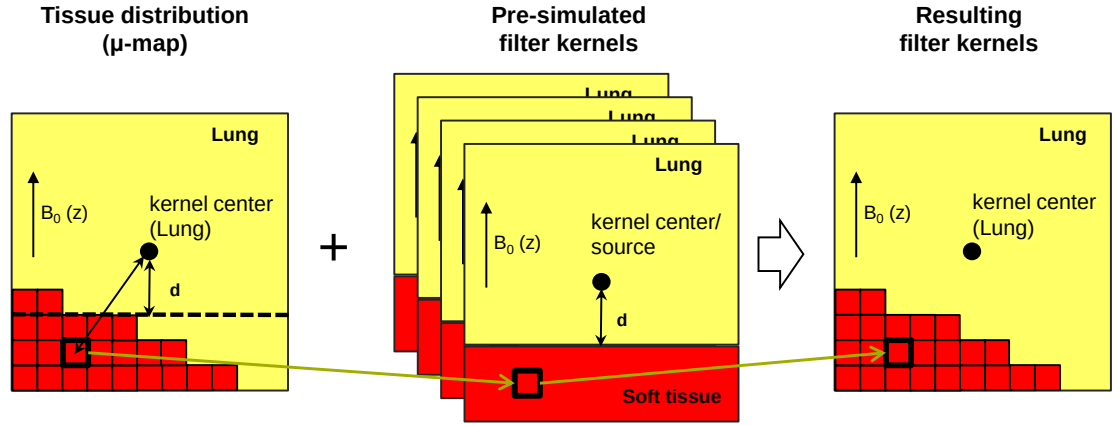

Figure 3.7: Generalized Approach: For each voxel within the filter matrix the distance d is calculated (left) and a corresponding kernel is selected from a pool of pre-simulated kernels with varying distances from the source voxel to the tissue border (middle). The corresponding voxel value in the resulting filter kernel (right) is then determined by the corresponding relative voxel value within the pre-simulated filter kernel.

The algorithm can be extended to reflect more than one tissue border per line and for more tissue types. Also, more tissue borders, e.g., perpendicular or diagonal to the x/y-plane could be added to the data set. The process of pre-simulation can be completely automated, and the kernels may be pre-calculated and buffered for the whole image prior to iterative reconstruction.

The resulting kernels for both approaches were exemplarily compared with the actual, Geant4-simulated distribution in Figure 3.8 for an image voxel near a cylindrically shaped soft tissue border. Only the generalized kernel is able to reflect both the increase in positron range distribution at the border and the decreased overall range into the denser tissue properly. This is also indicated in the line profile, where the generalized kernel matches the true distribution and only underestimates slightly near the tissue border.

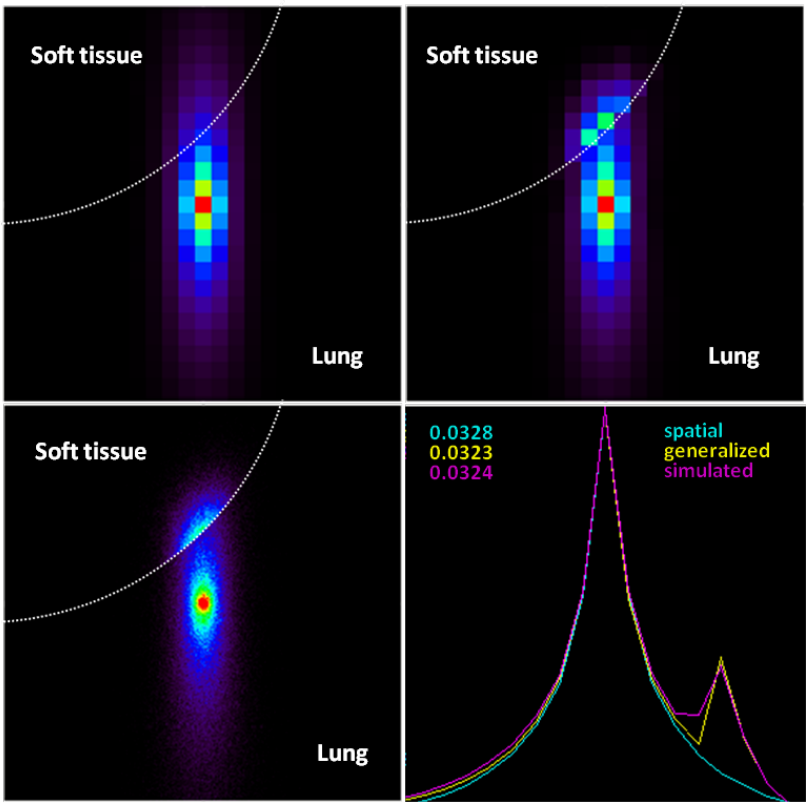

Figure 3.8: Comparison of positron range correction kernels for ^{82}Rb in lung tissue with cylindrically shaped border (dashed line) to soft tissue: spatial correction kernel (top row, left), generalized kernel (top row, right), Geant4 simulated kernel (bottom left), and line profile (bottom, right).

3.3.4 GATE Simulation and Phantom Studies

For this study, reconstruction was based on simulated PET/MR data using the *Geant4 Application for Tomographic Emission (GATE)* [101]. A GATE model of the Biograph mMR (see Fig. 3.9) was built according to the system's specifications [63]: The mMR has an axial field of view of 258 mm and a ring diameter of 656 mm. It consists of 64 LSO-crystal rings. The crystals are organized into 448 blocks, 56 blocks in transverse (x-y) and 8 blocks in axial (z) direction. Each block contains 64 (8×8) crystals. This leads to a total number of 28 672 crystals, and 448 crystals per crystal ring. The dimension of the crystal is $4 \times 4 \times 20$ mm^3. The energy resolution is 14.5 % and the energy window 430-610 keV. The time resolution is 3.6 ns and the coincidence window 5.86 ns [3]. The model also included the MR body coil with a length of 320 mm and a thickness of 10 mm. In addition, the 3 T MF was included in the simulation. GATE reliably models the presence of a MF [117, 163].

Data were generated using the mMR's model for a number of phantoms:

a) *Homogeneous phantoms* – These phantoms mimic the simulation setup in Section 3.3.1 with point sources. The source is set at (x,y,z) = (0.1, 1.0, 0.1) cm off the scanner's center in the center of a voxel.

b) *Inhomogeneous phantom (straight tissue border)* – The phantom consists of a $12 \times 12 \times 12$ cm^3 lung and an inner soft tissue region shown in Figure 3.10. Uniform activity regions (planar source) were simulated in a) lung tissue with a 9 mm distant soft tissue border in z-direction and in b) soft tissue with an adjacent lung region.

c) *Extended phantom (lung/liver)* – The phantom consists of an outer $14 \times 14 \times 20$ cm^3 soft tissue box and an inner $10 \times 10 \times 10$ cm^3 lung tissue box both centered. The inner box contains a cylinder with soft tissue rotated 90° around the x-axis with a radius of 50 mm. An ellipsoidal source with half-lengths of 8 mm (x/y) and 4 mm (z) was placed in lung close to soft tissue, reflecting, e.g., a lesion in lung right above the liver.

d) *Extended phantom (heart)* – The phantom consists of a solid ball of soft tissue with radius 4 cm embedded in a $16 \times 16 \times 16$ cm^3 lung tissue box. A spherical shell of 1 cm at the surface of the ball was simulated reflecting activity in the myocardium.

The simulated data were recorded as coincidences and binned into 3D sinograms for reconstruction. All data were reconstructed using the algorithm described in Section 3.3.2.

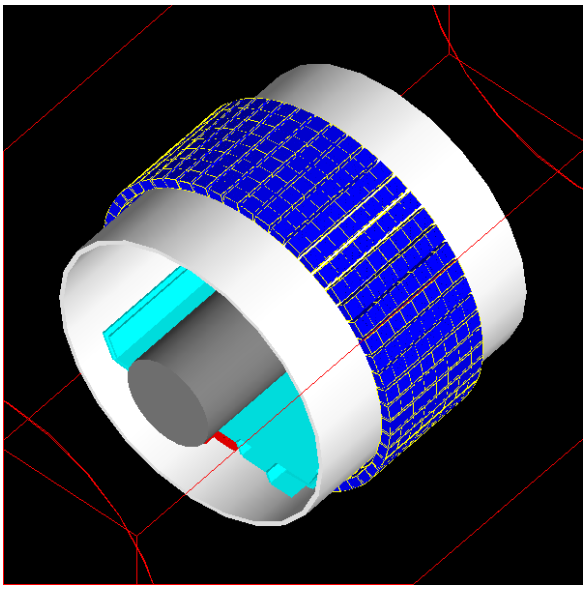

Figure 3.9: GATE-model of the 3 T Biograph mMR including the patient bed (green) and the MR-body coil (white) with a cylindrical phantom (grey).

3.4 Results

3.4.1 Reconstruction With and Without Positron Range Correction For Homogeneous Tissue

The effect of positron range and of the MF on the quality of PET reconstructed ^{82}Rb point sources was evaluated based on simulated mMR data for the homogeneous soft and lung tissue phantoms. The point spread after 10 MLEM iterations is summarized in Table 3.2. These results give a relative indication on how positron range influences the reconstructed scenarios. The point spread is stated in terms of FWHM and *full width at tenth maximum (FWTM)*, which was determined by linear interpolation with respect to the maximum value of the response obtained by a parabolic fit as in the *National Electrical Manufacturers Association (NEMA)* protocol [128]. The voxel size of the reconstruction was $1 \times 1 \times 2$ mm^3, also in accordance with the protocol.

At 0 T, lung tissue showed larger values than soft tissue in all directions, as can be expected from Fig 3.2. The difference becomes more apparent for the FWTM, 14.9 mm versus 11.3 mm on average. The presence of the 3 T MF in the scanner improved the average transversal point spread. The improvement was larger for lung, with 9 % in FWHM and 34 % in FWTM compared to soft tissue with 2 % and 15 %, respectively.

However, in agreement with the discussion in Section 3.3.1, the observed axial resolution as indicated by FWHM increased in the presence of the 3 T MF. This effect was more prominent in lung. A consistent increase could be observed for higher MF strengths, as in [117].

Adding our correction method using pre-simulated positron range kernels to the reconstruction algorithm, the potential for resolution improvement could be assessed. The kernel obtained from the annihilation distributions of Figure 3.3 reflects the 3 T MF and can be assumed ideal for the homogeneous phantoms. From Table 3.2 it can be seen that the correction was effective in all directions. The point source reconstruction became again approximately isotropic. In soft tissue, a significant average transversal improvement of 21 % from 4.3 mm to 3.4 mm (3 T) in FWHM was achieved. The same percentage of average transversal improvement was obtained for lung tissue.

The correction kernels' size had to be be chosen to cover the positron range adequately. Especially in z-direction, 25 mm in each direction from the kernel's center proved necessary for lung, whereas x/y-dimensions and soft tissue kernels could be chosen smaller. Overly truncated or wrongly chosen kernels led to visual artifacts, see also the discussion in [165] and [160].

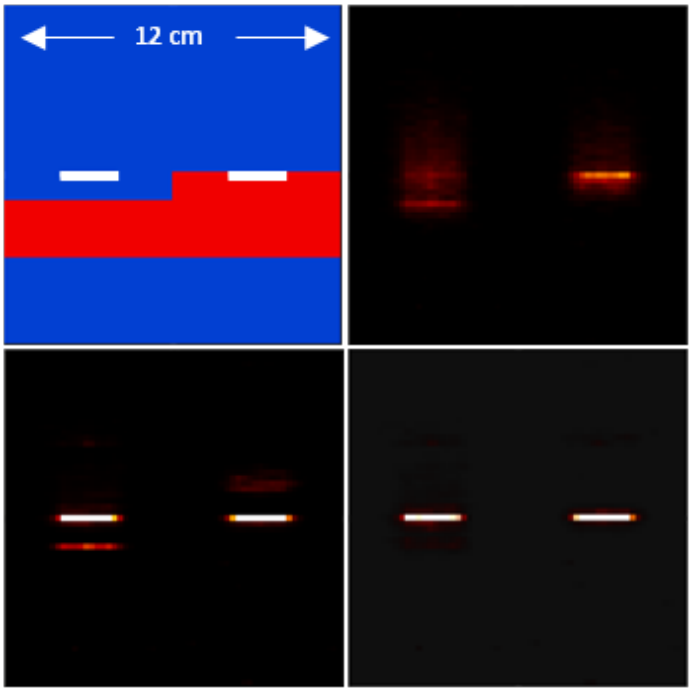

Figure 3.10: Phantom (upper left) used in GATE simulations with lung (blue) and soft tissue (red). Uniform activity ($20 \times 20 \times 2$ mm^3) was simulated (white regions). Reconstruction in coronal view using no correction (upper right), spatial (bottom left), and generalized (bottom right) correction kernels.

Table 3.2: Point spread of a reconstructed ^{82}Rb point source in homogeneous tissue

Tissue	**MF**	**Correction Kernel**	**Average transv. FWHM (mm)**	**Axial FWHM (mm)**	**Average transv. FWTM (mm)**
Soft	0.0 T	None	4.4	4.2	11.3
	3.0 T	None	4.3	4.9	9.6
Lung	0.0 T	None	4.7	4.6	14.9
	3.0 T	None	4.3	7.6	9.8
Soft	3.0 T	Spatial	3.4	3.1	7.2
Lung	3.0 T	Spatial	3.4	3.7	7.3

3.4.2 Positron Range Correction at Tissue Borders

In Section 3.3.1 we observed a strong variation of positron range distribution between lung and soft tissue as well as a larger range along the MF (z-direction). Especially at tissue borders, a concentration appeared at the border inside the denser material. Failure to correct for this effect led to visual and quantitative errors in the reconstruction.

This is shown in Figure 3.11 for a phantom with straight tissue borders (see Section 3.3.4 and Figure 3.10). Reconstruction of two plane sources from GATE simulation was done with clinically relevant voxel size of $2 \times 2 \times 2$ mm^3. Table 3.3 quantifies the results in terms of contrast, i.e., activity ratio of a 3 cm region of interest in all directions around the source to the source voxels themselves ($20 \times 20 \times 20$ mm^3). In addition, the relative ratio of activity found in the same tissue as the source and activity found in the other, wrong border tissue is given. The uncorrected image (top row) shows that the activity is largely blurred along the

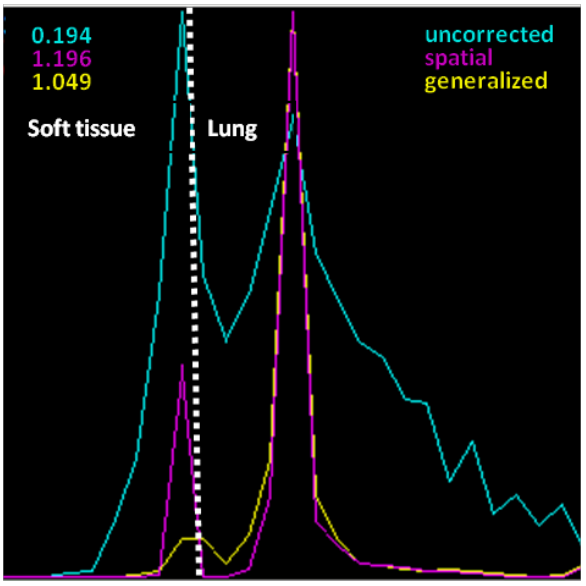

Figure 3.11: Vertical line profile in coronal view of Figure 3.10 through the left-hand source placed in lung for uncorrected and corrected reconstructions. The tissue border is indicated by the dashed line to the left of the source.

z-direction. This is especially the case for the source on the left-hand side of the phantom where activity was placed in lung. Here, contrast was only 7 %. A significant share of activity was concentrated in the soft tissue border 9 mm below the source.

Using spatially variant correction (middle row), the contrast was improved, but activity was still located in the wrong tissue. Even worse, visual artifacts were introduced. For the source in lung, the correction kernel wrongly concentrated 23 % of the activity close to the border in soft tissue. For the source in soft tissue, the homogeneous soft tissue kernel was wrongly applied to the adjacent lung region. This led to overcorrection near the border, and undercorrection at approximately 1 cm away from the border. This undercorrection led to a subtle artifact, which appeared more prominently in the heart phantom (see Section 3.4.3).

The generalized approach (bottom row) predicting the positron range more accurately achieved better contrast (especially for the soft tissue part) and showed no visible artifacts. It was able to reduce the activity allocated in the wrong tissue down to 12 % resp. 7 %. These visual effects are also visible in the line profile (Fig. 3.11) along the z-direction

Table 3.3: Relative Activity and contrast of ^{82}Rb plane sources for the inhomogeneous phantom in Fig 3.10

Source Plane	**Correction Kernel**	**Contrast**	**Relative Activity Source Region (%)**	**Relative Activity Border Region (%)**
Lung	None	7	76	24
	Spatial	41	77	23
	Generalized	43	93	7
Soft	None	21	74	26
	Spatial	54	83	17
	Generalized	60	88	12

for the lung source, where the source is shown in the center and the (wrong) concentration at the tissue border is visible on the left-hand side.

3.4.3 Extended Simulation Study for ^{82}Rb and ^{68}Ga

We also conducted an extended phantom study in a more clinically relevant context. This study focused on positron range and assumed data to be already corrected for other resolution-degrading effects such as motion. All sources were reconstructed at $2 \times 2 \times 2$ mm^3 resolution using a) no correction, b) spatially variant correction, or c) generalized correction. No post-smoothing was applied and images shown are interpolated. Contrast was given in the sense of Section 3.4.2.

The first phantom modeled an ellipsoidal lesion of 16 mm×8 mm×8 mm in lung placed close to a cylindrically shaped body of soft tissue (see Section 3.3.4). The results of all correction approaches are shown in Figs. 3.12 and 3.13 for ^{82}Rb and ^{68}Ga respectively. The contrast remained low in the uncorrected images (20 % and 32 % resp.). It became obvious that positron range correction is beneficial for both nuclides, and contrast was significantly increased (to more than 50 % for ^{82}Rb and to more than 55 % for ^{68}Ga). The uncorrected image and spatially variant correction both showed misplaced concentration in soft tissue that was visibly reduced by generalized correction. The effect was stronger for ^{82}Rb, where contrast was increased by 10 %, but also ^{68}Ga benefitted from generalized correction.

The second phantom modeled a myocardium-like structure and results are shown for ^{82}Rb in Figure 3.14. A moderate increase in contrast from 68 % to 75 % could be observed for the corrected images, and the delineation was improved as can be seen in the line profile. Overcorrection by the spatially variant kernel artificially increased contrast at borders, and subsequent undercorrection led to artifacts at approximately 1 cm above and below the

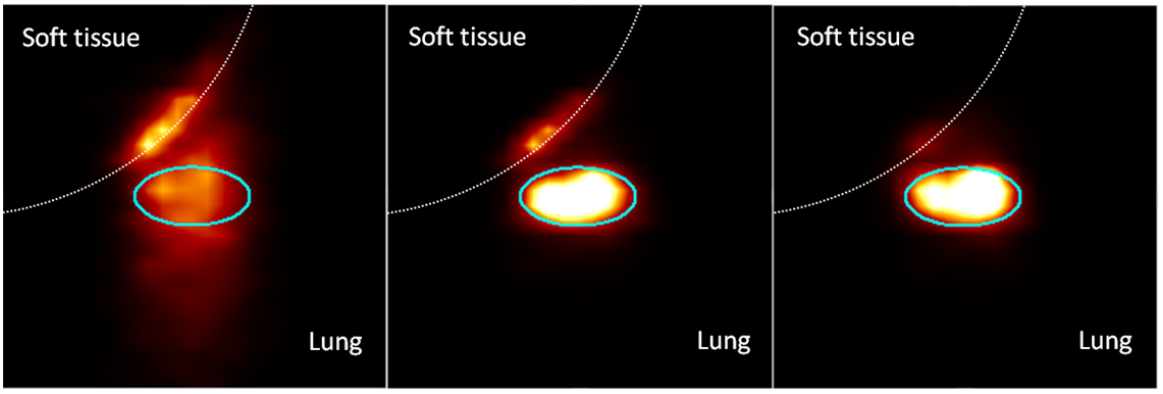

Figure 3.12: Reconstructed elliptical source (^{82}Rb) placed in lung next to a cylindrically shaped border (indicated by dotted line) to soft tissue shown in coronal view: no correction (left), spatial (middle), generalized (right) correction.

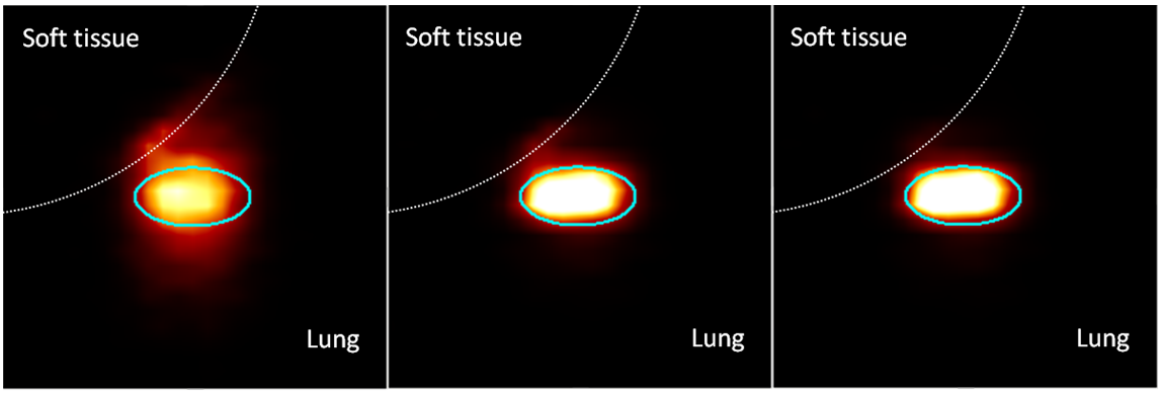

Figure 3.13: Reconstructed elliptical source (^{68}Ga) placed in lung next to a cylindrically shaped border (indicated by dotted line) to soft tissue shown in coronal view: no correction (left), spatial (middle), generalized (right) correction.

phantom. The artifact was mitigated by the generalized approach, as also seen in the line profile.

3.5 Discussion

In this work we have studied positron range and its effect on PET/MR image reconstruction for different tissue types based on MC simulation of high energy positron emitters. Rather than considering positron range in water [42], we focused on clinically relevant tissue types that are directly available from the MR attenuation map in PET/MR imaging, namely lung and soft tissue.

In agreement with previous work [159, 163] we confirmed a strong tissue dependency of positron range. In addition, we found borders between high and low density materials to have a noticeable impact on its distribution, with positrons annihilating along the border in

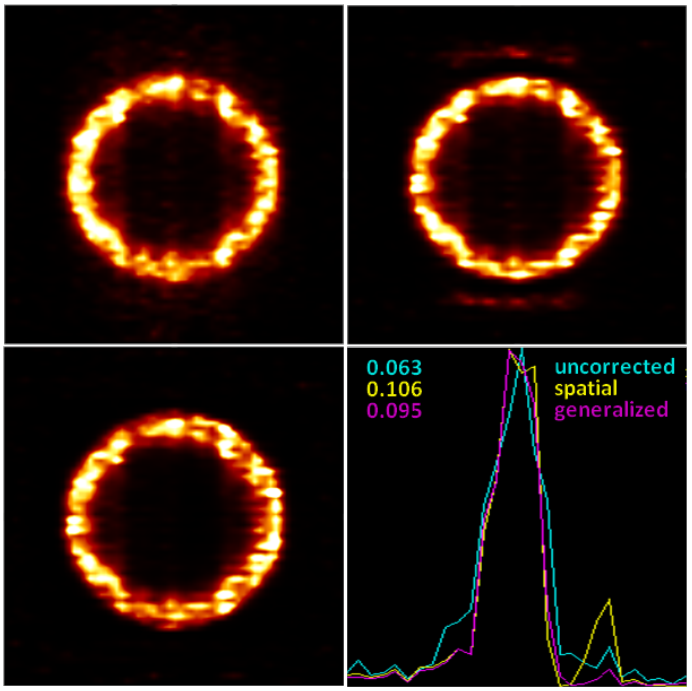

Figure 3.14: Reconstructed spherical shell (^{82}Rb) within soft tissue and surrounding lung tissue in coronal view: no correction (upper left), spatial (upper right), generalized (bottom left) correction. Vertical line profile in coronal view (bottom right).

the denser material. The study was extended to a 3 T MF, reflecting an integrated PET/MR. As expected [145], this strongly reduces positron range in the directions orthogonal to the MF.

However, and as a consequence, we found the mean positron range in the direction of the MF (z-direction) to be unchanged, but the density of the distribution in z-direction is increased significantly. Furthermore, a strong tissue dependency occurs along the z-direction, with mean values increasing by more than 200 % from soft tissue to lung for ^{82}Rb. Altogether, this justifies a re-evaluation of positron range correction in the context of inhomogeneous tissue configurations and in the presence of a MF.

Regarding the impact of positron range on the point spread of the 3 T mMR (see Section 3.4.1), we found relative improvements due to the MF to be moderate in x/y-directions. The improvement would be more significant for a stronger MF as considered in [93]. However, the point spread becomes anisotropic and a relative increase by 65 % in z-direction can be observed for ^{82}Rb.

Assessing the potential of tissue-specific positron range correction in our reconstruction framework, we applied ideal, pre-simulated kernels to homogeneous tissue configurations. It could be shown that the effect of the positron range in the presence of the MF could be almost completely mitigated. The relative improvement was up to 50 % for lung, and the point spread became almost isotropic again.

From our extended phantom studies (see Section 3.4.3), the improvement due to tissue-specific positron range correction could be also verified in more realistic settings. We observed a significant increase of up to 2.5X in contrast for high-energy tracers in a lesion-like structure placed in lung and a much better localization. The benefits for a myocardium-like shell of activity placed in a soft tissue ball in lung were smaller yet noticeable and showed a better structural delineation in the line profile.

As predicted by [159] we confirmed that differing positron range in lung and soft tissue causes artifacts in imaging of activity in the denser material. The effect has been shown in [111] to be even more dramatic if the low density material is air rather than lung. Our studies showed strong concentrations of activity at distances of up to 1.5 cm.

However, extended tissue-specific positron range modeling is required to overcome such artifacts in inhomogeneous regions [117]. Our proposed, generalized method was able to reduce the amount of activity wrongly allocated in the border tissue by up to 70 %. This resulted in a further increase in contrast and a strong reduction of visual misplacement artifacts. Also, artifacts due to undercorrection at tissue borders could be mitigated.

Our correction method is flexible and independent of the correction of other degrading effects such as motion. Rather than modifying the system matrix, it locally applies diffusion kernels representing the impact of positron range on the image estimate, approximating the activity distribution better. The generalized correction kernels are composed for each coefficient individually based on tissue information from the PET/MR's attenuation map and pre-simulated data sets incorporating tissue borders.

Accounting for positron range in inhomogeneous regions was addressed previously in [19] and [22], yet not considering a 3 T MF and a PET/MR system. Compared to the iterative convolution approach of Bai *et al.* [22], our approach directly computes local diffusion kernels depending on the local tissue configuration in one step. The analytical model kernels of Alessio *et al.* [19] differ visually from our pre-simulated distribution at boundaries in that no accumulation in the denser is reflected.

Our proposed method can be extended to more tissue types; support for multiple tissue borders in one line of sight and borders with different alignment can be added. These extensions would increase the database significantly, but the process of pre-simulation can be completely automated, and the kernels may be pre-calculated and buffered for the whole image prior to iterative reconstruction. The computational burden of applying the correction kernels for a medium resolution image (2 mm) remains feasible; all studies were conducted with $25 \times 25 \times 25$ kernels on a standard laptop.

Altogether, there is a potential for positron range correction for high-energy tracers even for medium resolution clinical scanners such as the mMR and at 3 T. Given that PET/MR

promises better co-registration and motion correction [89, 174], tissue-specific approaches may become more feasible and applicable. Furthermore, it is to be expected that the benefits would scale accordingly to high-resolution PET/MR scanners (e.g., small animal), very high energy tracers, and stronger MFs.

3.6 Conclusion

We have investigated positron range for high energy tracers such as ^{82}Rb and its effect on image quality in the new Siemens Biograph mMR hybrid PET/MR scanner using MC simulation. We found positron range to be tissue dependent and especially significant in the direction of the 3 T MF. At inhomogeneous tissue borders, this degrades spatial resolution and can lead to misplacement artifacts. Our 3D-MLEM framework applying positron range diffusion kernels allows for a localized correction depending on underlying tissue. A potential for tissue-specific positron range correction was found for both homogeneous regions and at tissue borders. Especially, our anatomically generalized approach improved image quality for realistic phantoms.

Chapter 4

Maximum a posteriori direct parametric reconstruction using simultaneously acquired PET/MR information

This chapter is based on work previously published in the IEEE Transactions on Medical Imaging [2] (© 2015 IEEE. Reprinted, with permission, from R. Loeb *et al.*, IEEE Trans Med Imaging 2015; 34(11): 2233 - 2247). The author of this thesis is the main contributor to that publication and has conducted all relevant research.

—

Pharmacokinetic analysis of dynamic PET imaging data maps the measured time activity curves to a set of model-specific pharmacokinetic parameters. Voxel-based parameter estimation via curve fitting is conventionally performed indirectly on a sequence of independently reconstructed PET images, leading to high variance and bias in the parametric images. This chapter describes a direct parametric reconstruction algorithm with raw projection data as input that leverages high-resolution anatomical information simultaneously obtained from MRI in a PET/MR scanner for regularization. The associated reconstruction problem was formulated in a flexible Bayesian framework with Gaussian Markov Random field modeling of activity, parameters, or both simultaneously. MR information was incorporated through a Bowsher-like prior function. Optimization transfer using an expectation-maximization surrogate and a new Bowsher-like penalty surrogate was applied to obtain a

voxel-separable algorithm that interleaves a reconstruction with a fitting step to an analytical input function model. The algorithm was evaluated on simulated [^{18}F]FDG and clinical [^{18}F]FET brain data acquired with a Biograph mMR.

This chapter is organized as follows: After discussing related work, we outline our approach in Section 4.2. Theory is presented in Section 4.3, where we develop the reconstruction framework (Sec. 4.3.2) and construct an algorithm based on separable surrogate functions (Sec. 4.3.3). Parameter scaling and analytical compartment modeling are found in Sections 4.3.4 and 4.3.5. Methods are described in Section 4.4. Results for simulated data are in Section 4.5.1 and for clinical data in Section 4.5.2. Section 4.7 concludes the chapter after discussions in Section 4.6.

4.1 Related Work

Dynamic PET (cf. Sec. 2.5) acquires a sequence of 3D images over time that reflects the uptake and washout of an injected radiotracer in the imaged object. Pharmacokinetic analysis as introduced in Section 2.5.1 allows to estimate biologically relevant kinetic parameters from the measured concentration in tissue over time (TAC). These parameters aid the diagnosis of many diseases [68] and can help clinicians better differentiate between malignant and benign tissue, e.g., in brain tumor imaging [140]. Especially in heterogeneous regions, high resolution parametric images are needed, but their generation via voxel-level curve fitting is challenging due to inherent noise.

Conventionally, 4D PET images are obtained from independent reconstructions of PET data that were acquired over the length of consecutive time frames with potentially low count statistics. This results in noisy PET images with widely used iterative MLEM algorithms due to the ill-conditioning of the tomographic problem. Pharmacokinetic modeling is typically applied as a post-reconstruction step and thus sensitive to noise in the PET images, leading to noisy parametric images. Post-processing techniques such as filtering or ROI-based approaches that, e.g., cluster voxels with similar kinetics exist. However, all post-reconstruction modeling approaches are fundamentally limited as they operate only indirectly on the reconstructed images and the parameter estimation process does not accurately model the noise statistics.

Recently proposed approaches directly reconstruct parametric images from sinogram data by maximizing the dynamic Poisson likelihood function, reflecting the noise statistics more accurately. However, sophisticated optimization algorithms are required, especially for compartment models with non-linear relationship of parameters to the expected PET data. We refer to [143] and [176] for detailed reviews.

For linear models, Matthews *et al.* [123] developed in 1997 a direct parametric reconstruction method using temporal basis functions based on the MLEM algorithm. For the Patlak model that applies to irreversibly binding radiotracers, Tsoumpas *et al.* [175] presented a similar algorithm, and Wang *et al.* [184] developed a preconditioned gradient algorithm for MAP reconstruction to achieve faster convergence. For the analysis of reversible radiotracers, e.g., Logan, Rahmim *et al.* [144] developed a direct, bound-constraint algorithm that can cope with negative parameter estimates. In order to overcome the slow convergence of direct reconstruction methods, Wang *et al.* [186] proposed a nested EM algorithm for linear models. It alternates a reconstruction step with linear parameter estimation, effectively decoupling both.

For nonlinear models, the work of Kamasak *et al.* [104] was the first to incorporate a 2TC model into a MAP direct reconstruction framework using a parametric iterative coordinate descent algorithm. Elegant approaches were recently proposed by Wang *et al.* [185] [187] that utilize surrogate functions for optimization transfer and that are independent of the kinetic model. These methods decouple image reconstruction from kinetic fitting in each iteration, allowing to speed up algorithm convergence by running multiple fitting steps in each iteration [186]. Empirical implementations for 2TC parameter estimation using an alternating two step approach have also been proposed [147] [124].

Bayesian methods that incorporate prior information can address the ill-posedness of the reconstruction problem. Markov random field priors are widely used in MAP reconstruction, enforcing local image smoothness. Whereas quadratic priors tend to smooth over edges, more sophisticated priors attempt to smooth locally while maintaining edges such as the Green [86], Geman [83], and Huber [127] priors.

With fully-integrated PET/MR systems, e.g. the Siemens Biograph mMR, additional high-resolution anatomical information becomes available, making anatomical priors highly attractive to increase the quality and resolution of PET images. Anatomical segmentation with regional labeling [54] [21] and information theoretical similarity measures for CT or MR and PET such as mutual information [161] or joint entropy [132] have been proposed as anatomical priors. Bowsher *et al.* [35] proposed a locally operating prior that exploits anatomical similarity of neighboring voxels, and modified versions exist [182].

The application of anatomical priors can be hampered by two types of mismatch between PET and MR images: positional mis-alignment and missing correlation. Mis-alignment is alleviated with simultaneously operating multi-modality systems, but may still be present, for example due to motion. This can be addressed to some extent, e.g., by using blurred anatomical labels [54] or simultaneous estimation of PET/MR alignment parameters and image reconstruction [36]. In this work we leverage a weighted Bowsher anatomical prior [33],

which outperforms the original Bowsher prior [35] in case of mis-alignment. Missing correlation between MR and PET images is not addressed in this work, as we focus on the general feasibility of leveraging matching anatomical information for parametric PET reconstruction. Multimodal imaging including MR and PET has shown promise for brain tumor diagnosis [198], and positive correlations have been found [80]. Since activity, parametric, and MR images are influenced by common underlying pathophysiological factors, they are usually not completely independent. This means, even as image intensities and contrast differs between the modalities, local similarity is likely to be valid in many situations. With the ongoing evolution of MR imaging sequences, it is an open question which anatomical information is best suited to enhance PET. In addition, recent methods allow to address missing correlation effectively [129].

Regularization in direct reconstruction methods is often applied to the activity images, e.g., by Wang *et al.* [187], or directly to the parametric images. The latter was done for linear models in [168], and in a tailored approach for a 2TC model in [104]. Anatomically-driven approaches leveraged joint entropy regularization applied to linear Patlak parameters [168] and recently to a single kinetic parameter [34] in a 2TC model. Both anatomically-driven approaches were evaluated on simulated PET/MR data.

4.2 Developing and evaluating a direct parametric reconstruction framework

We developed a direct nonlinear parametric reconstruction algorithm that incorporates simultaneously acquired anatomical MR information via a modified Bowsher prior into a Bayesian framework. The developed Bayesian framework is flexible in that it is not limited to a given compartment model and that it can perform regularization on the dynamic activity images, on the estimated parameters directly, or on both at the same time. We showed the feasibility of such regularization in a MAP reconstruction algorithm that is based on separable surrogate functions. It alternates between a conventional dynamic frame-wise EM reconstruction step and a penalized voxelwise fitting step. The latter is accomplished by a nonlinear preconditioned conjugate gradient algorithm that leverages analytical calculations for the TAC derivatives.

The framework was used to asses the benefits of anatomical regularization and to reveal tradeoffs as regularization was applied to activity and/or parametric images. Both simulated and clinical PET/MR data were used.

- The simulation was performed for an [^{18}F]FDG PET study from literature [187] of the human brain with a matching realistic MR image.

- The clinical study investigated the feasibility of compartment modeling to dynamic [^{18}F]FET brain imaging with the Biograph mMR using our method. The patient considered was diagnosed with glioblastoma.

To our knowledge, there is little work so far on kinetic modeling of dynamic [^{18}F]FET that could support tumor grading. Since brain tumors are often heterogeneous, reliable voxelwise kinetic information would be valuable in clinical practice.

4.3 Theory

4.3.1 Direct parametric PET reconstruction

The objective of direct parametric PET reconstruction is to generate parametric images $\theta^p \in \mathbb{R}^J$, $p = 1, \ldots, P$, directly from the measured dynamic data. In dynamic PET the measured events recorded over the whole scanning time are divided into multiple consecutive time frames $m, m = 1, \ldots, M$, each containing the events detected between frame start time t_{ms} and frame end time t_{me}. The dynamic data set is given as a sequence of sinograms $\{y_m,\ m = 1, \ldots, M\}$ where each $y_m = (y_{1m}, \ldots, y_{Im})^T \in \mathbb{R}^I$ stores the coincidence events detected in the ith detector pair during the mth time frame. The components y_{im} can be modeled as realizations of independent Poisson random variables with mean values $\bar{y}_{im}(\theta)$ for $i = 1, \ldots, I$ and related to the dynamic activity volume through the scanner's system matrix $A \in \mathbb{R}^{I \times J}$: Let $\theta_j \in \mathbb{R}^P$ contain the P parameters at voxel j and $x_m(\theta) = (x_m(\theta_1), \ldots, x_m(\theta_J)) \in \mathbb{R}^J$ denote the dynamic activity vector at frame m where the transformation

$$x_m\ :\ \mathbb{R}^P \to \mathbb{R}^+\ :\ \theta_j \to \int_{t_{ms}}^{t_{me}} C_T(t, \theta_j) dt$$

maps the parameter vector at voxel j to the average activity using a kinetic model describing the time activity distribution $C_T(t, \theta_j)$ dependent on its parameter vector θ_j for each voxel. The direct relation between the kinetic parameters and the estimated PET data is given by the affine transformation

$$\bar{y}_{im}(\theta) = \sum_{j=1}^{J} a_{ij} x_m(\theta_j) + n_{im}$$

where the (i, j)th element a_{ij} of A contains the probability of an emitted event in voxel j being detected in detector pair i. Background events including random and scattered events are denoted by n_{im}. Given a complete dynamic data vector $y = (y_1, \ldots, y_M)$ direct reconstruction of parametric images can be achieved by solving the maximum likelihood maximization problem

$$\hat{\theta} = \arg\max_{\theta} L(y|\theta)$$

that maximizes the dynamic Poisson log-likelihood function

$$L(y|\theta) = \sum_{m=1}^{M} \sum_{i=1}^{I} y_{im} \log \bar{y}_{im}(\theta) - \bar{y}_{im}(\theta). \tag{4.1}$$

4.3.2 MAP reconstruction framework for parametric imaging

4.3.2.1 Activity vs. parametric regularization

Due to the ill-posedness of the tomographic problem in PET, the solution of the log-likelihood function (4.1) results in noisy images at convergence. Thus, regularization is added to (4.1) through a penalty function R, and the MAP estimator $\hat{\theta}$ maximizes the penalized log-likelihood function

$$\arg\max_{\theta} \Psi(\theta), \quad \Psi(\theta) = L(y|\theta) - \alpha R(\theta). \tag{4.2}$$

The regularizing penalty function R typically imposes a smoothness constraint on the reconstructed image and its strength is controlled by the regularization parameter α. A proper choice of α is important to balance the tradeoff between resolution and noise. The larger α is chosen, the more the solution deviates from the unregularized ML solution: it is less noisy but suffers from a loss of resolution. For the work presented in this chapter we considered a general Markov Gibbs prior with quadratic potential of the form

$$R(\theta) = \frac{1}{4} \sum_{q=1}^{Q} \frac{1}{\sigma_q^2} \sum_{j=1}^{J} \sum_{k \in \mathcal{N}_j} \frac{1}{2} \omega_{jk} (T_q(\theta_j) - T_q(\theta_k))^2 \tag{4.3}$$

where σ_q^2 is a positive scaling factor, $\mathcal{N}_j$ denotes the neighboring voxels of the current voxel j with a corresponding weighting factor ω_{jk}. The arbitrary transformation T determines the type of regularization used in the reconstruction and the parameter Q determines the number of terms to be regularized. This framework is generic in nature, and the following regularization types were considered in the context of this thesis:

- *Time activity curve based regularization.* In this case $Q = M$ and the transformation $T_q \colon \mathbb{R}^P \to \mathbb{R}$ is defined by $T_q(\theta_j) = x_q(\theta_j)$. This form of regularization on the dynamic activity was proposed in [187]. There, weights ω_{jk} were chosen as the inverse of the distance in a symmetric neighborhood region, thus reflecting regular spatial smoothing. We extended this approach to take anatomical information into account by choosing the weights for each neighboring pixel to reflect the anatomical similarity present in the MR image.

- *Regularization of a single parametric image.* In this case $Q = 1$ and $T_1 \colon \mathbb{R}^P \to \mathbb{R}$ either selects a component of θ or is a well-behaved transformation on θ. This means that regularization is performed directly on the parametric image or on derived kinetic parameters of interest, instead of on the activity image as above.
- *Regularization of multiple parametric images.* The second approach is extended to regularize more than one kinetic parameter, that is $1 < Q <= P$ and $T_q \colon \mathbb{R}^P \to \mathbb{R}$. In the following, we assume $Q = P$, i.e., regularization is applied to a full set of kinetic parameters uniquely defining the time activity curve.
- *Simultaneous regularization of time activity curve and parametric images.* A combination of approach one with approach two or three from above.

4.3.2.2 Anatomically weighted Markov prior

The distance-weighted smoothing prior suffers from smoothing over edges, which leads to high bias at edges in the image. The situation is worse for parametric images, where smoothing over functionally different physiological regions may lead to artifacts.

In order to retain the edges, we aim to use anatomical prior information from a simultaneously acquired MR image, and have chosen to adopt the anatomically-weighted prior proposed by Bousse *et al.* [33] for this purpose. This prior considers all voxels in a given neighborhood, but the contribution of each voxel is weighted depending on anatomical similarity. In addition, this prior is straightforward to use in our intended optimization transfer framework, if it is slightly modified as follows in order to yield a symmetrical weighting function ω_{jk} to be deployed in the Markov Gibbs prior

$$R(\theta) = \frac{1}{8} \sum_{q=1}^{Q} \frac{1}{\sigma_q^2} \sum_{j=1}^{J} \sum_{k \in \mathcal{N}_j} \underbrace{\eta \left(\frac{|\mu_j - \mu_k|}{\frac{M_j + M_k}{2}} \right)}_{=:\omega_{jk}} (T_q(\theta_j) - T_q(\theta_k))^2 \tag{4.4}$$

where $M_j = \max_{k \in \mathcal{N}_j} |\mu_j - \mu_k|$ and $M_k = \max_{j \in \mathcal{N}_k} |\mu_k - \mu_j|$. Here, we have replaced the denominator in the argument to $\eta(\cdot)$ to be the arithmetic mean of the function M of the two voxels in question rather than their maximum. We refer to regularization using the weighting function (4.4) as *Bowsher weighted* in the following.

As a transfer function $\eta(\cdot)$ the third function proposed in [33] was used, as it showed the best performance and is also defined for $\eta > 1$, as can happen in our case

$$\eta(u) = \arctan((\zeta - u)/\rho)/\pi + 0.5.$$

The parameters ζ and ρ control the turning point location and slope that was set to $\zeta = 0.5$ and $\rho = 0.01$. The function is plotted in Figure 4.1. Smaller values led to a more rigorous selection of neighbors, approximately comparable to reducing the number of neighbors in the original Bowsher prior.

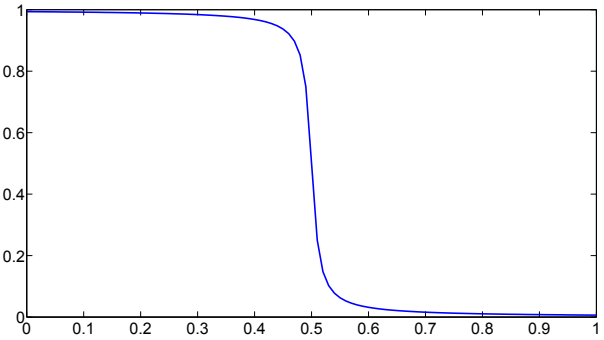

Figure 4.1: Representative curve of η for $\zeta = 0.5$ and $\rho = 0.01$.

4.3.3 Optimization Transfer

An efficient optimization algorithm is needed for the penalized likelihood problem in (4.2) supporting the regularization framework in (4.3) and the anatomical weight in (4.4). Solving the problem directly is nearly impossible due to the high number of variables (proportional to the number of voxels), especially for nonlinear models. Applying the optimization transfer principle, however, the problem can be made separable, i.e., all nonlinear fitting can be performed voxelwise. Maximization of the penalized likelihood function is transferred to the maximization of a separable surrogate function $S(\theta|\theta^n)$ that is constructed in the $n+1$th iteration from θ^n, which denotes the value of θ from the nth iteration. The surrogate function has to fulfill the following monotonicity condition [113]

$$S(\theta|\theta^n) - S(\theta^n|\theta^n) \leq \Psi(\theta) - \Psi(\theta^n)$$

in order to ensure a monotonic increase of $\Psi(\cdot)$. In the following, a combined surrogate function $S(\cdot)$ is designed by constructing separate surrogate function for the log-likelihood function and the penalty function of Ψ.

4.3.3.1 Separable Surrogate for Log-likelihood

A surrogate function of the dynamic likelihood function is taken from the derivation of the MLEM algorithm, which is a special case of optimization transfer algorithm [113]. It

depends on Jensen's inequality $f(\sum_{j=1}^{n} \alpha_j v_j) \leq \sum_j \alpha_j f(v_j)$ where f is a convex function, $\alpha_1, \ldots, \alpha_n \geq 0$ such that $\sum_j \alpha_j = 1$ and on its extension

$$f\left(c^T u\right) \leq \sum_j \frac{c_j v_j}{c^T v} f\left(\frac{c^T v}{v_j} u_j\right) =: g(u|v) \tag{4.5}$$

where $\alpha_j = c_j v_j / c^T v$ and $v_j = c^T v u_j / v_j$ and u, v, c are positive vectors. By application of (4.5) to $\log\left(\bar{y}_{im}(\theta)\right)$ of (4.1) with $u_j = x_m(\theta_j), v_j = x_m(\theta_j^n), c_j := p_{ij}$ the following inequality can be obtained where we ignore constants that are independent from θ

$$\begin{aligned} L(y|\theta) \geq \sum_{m=1}^{M} \sum_{i=1}^{I} \Big(y_{im} \sum_{j=1}^{J} \frac{p_{ij} x_m(\theta_j^n)}{\bar{y}_{im}(\theta^n)} \log\left(x_m(\theta_j)\right) \\ - \sum_{j=1}^{J} p_{ij} x_m(\theta_j) \Big). \end{aligned} \tag{4.6}$$

By rearrangement of the right-hand side of (4.6) as in [187] the following surrogate function for the dynamic likelihood can be derived

$$S_{log}(\theta|\theta^n) = \sum_{j=1}^{J} s_j \left(\sum_{m=1}^{M} x_{jm}^{em,n} \log x_m(\theta_j) - x_m(\theta_j) \right) \tag{4.7}$$

where $s_j = \sum_i p_{ij}$ is the sensitivity and

$$x_{jm}^{em,n} = \frac{x_m(\theta_j^n)}{s_j} \sum_i p_{ij} \frac{y_{im}}{\bar{y}_{im}(\theta^n)}$$

is a static MLEM reconstructed image update for the mth frame in the nth iteration. The first term in (4.7) was derived by introducing a multiplication with $1 = s_j / s_j$. The derived surrogate function is based on the dynamic sequence of statically reconstructed MLEM images that are computed at the start of each iteration.

4.3.3.2 Separable Surrogate for Penalty

Using de Pierro's decoupling rule [59], we have for any convex and even function $\varphi : \mathbb{R} \to \mathbb{R}$, and any $u_j, u_k, u_j^n, u_k^n \in \mathbb{R}$

$$\begin{aligned} \varphi(u_j - u_k) &= \varphi\Big(\frac{1}{2}\left(2u_j - u_j^n - u_k^n\right) + \frac{1}{2}\left(-2u_k + u_j^n + u_k^n\right) \Big) \\ &\leq \frac{1}{2}\varphi\left(2u_j - u_j^n - u_k^n\right) + \frac{1}{2}\varphi\left(2u_k - u_j^n - u_k^n\right). \end{aligned} \tag{4.8}$$

Applying (4.8) to one of the Q scaled summands of (4.3) and keeping $u = T(\theta)$ for simplicity, we get

$$\begin{aligned} U &:= \sum_{j=1}^{J} \sum_{k \in \mathcal{N}_j} \omega_{jk} (u_j - u_k)^2 \\ &\leq 2 \sum_{j=1}^{J} \sum_{k \in \mathcal{N}_j} \omega_{jk} \left([u_j - \bar{u}_{jk}]^2 + [u_l - \bar{u}_{jk}]^2 \right) \end{aligned} \tag{4.9}$$

with $\bar{u}_{jk} = \bar{u}_{kj} = \left(\frac{u_j^n + u_k^n}{2} \right)$. Assuming the neighborhood system satisfies the property $k \in \mathcal{N}_j \Leftrightarrow j \in \mathcal{N}_k$, the sum in (4.9) can be written as the following

$$\begin{aligned} &\cdots + \omega_{j'k'} \left(u_{j'} - \bar{u}_{j'k'} \right)^2 + \omega_{j'k'} \left(u_{k'} - \bar{u}_{j'k'} \right)^2 + \cdots \\ &\cdots + \omega_{k'j'} \left(u_{k'} - \bar{u}_{k'j'} \right)^2 + \omega_{k'j'} \left(u_{j'} - \bar{u}_{k'j'} \right)^2 + \cdots \ . \end{aligned}$$

Combining now the terms involving $u_{j'}$ and assuming symmetric weights, i.e., $\omega_{jk} = \omega_{kj}$, the following surrogate function can be derived from the right hand side of (4.9)

$$\tilde{S}(u|u^n) = 4 \sum_{j=1}^{J} \sum_{k \in \mathcal{N}_j} \omega_{jk} \left(u_j - \bar{u}_{jk} \right)^2 .$$

This formulation makes the original penalty function U separable, as optimization for each voxel j only requires values of neighboring voxels from the previous iteration, $\bar{u}_{jk}$. For a more efficient implementation, $\tilde{S}$ can be reformulated such that the neighborhood operation is precomputed only once per iteration as a smoothing operation, as proposed by Wang [187]. If we define $\omega_j^{reg} = \sum_{k \in \mathcal{N}_j} \omega_{jk}$ and $u_j^{reg,n} = \frac{1}{2\omega_j^{reg}} \sum_{k \in \mathcal{N}_j} \omega_{jk} (u_j^n + u_k^n)$, we can define a surrogate $\bar{S}_{pen}(u|u^n)$ via Jensen's inequality:

$$\begin{aligned} \tilde{S}(u|u^n) &= 4 \sum_{j=1}^{J} \omega_j^{reg} \Big(u_j^2 - 2u_j \frac{\sum_{k \in \mathcal{N}_j} \omega_{jk} (u_j^n + u_k^n)}{2\omega_j^{reg}} \\ &\quad + \frac{\sum_{k \in \mathcal{N}_j} \omega_{jk} (u_j^n + u_k^n)^2}{4\omega_j^{reg}} \Big) \\ &= 4 \sum_{j=1}^{J} \omega_j^{reg} \left(u_j^2 - 2u_j u_j^{reg,n} + (u_j^{reg,n})^2 + \delta(u^n) \right) \\ &= \underbrace{4 \sum_{j=1}^{J} \omega_j^{reg} \left(u_j - u_j^{reg,n} \right)^2}_{=: \bar{S}_{pen}(u|u^n)} + \underbrace{4 \sum_{j=1}^{J} \omega_j^{reg} \delta(u^n)}_{\Delta(u^n)} \end{aligned}$$

where $\delta(u^n)$ is a nonnegative expression that is either constant or only depends on u^n. $\bar{S}_{pen}(u|u^n)$ fulfills the monotonicity condition with respect to the original penalty function U:

$$\begin{aligned}
&\bar{S}_{pen}(u|u^n) - \bar{S}_{pen}(u^n|u^n) \\
&\quad = (\tilde{S}(u|u^n) - \Delta(u^n)) - (\tilde{S}(u^n|u^n) - \Delta(u^n)) \\
&\quad = \tilde{S}(u|u^n) - \tilde{S}(u^n|u^n) \geq U(u) - U(u^n) \qquad (4.10)
\end{aligned}$$

where inequality (4.10) follows directly by construction of $\tilde{S}$.

Since our anatomical weighting scheme (4.4) is based on a regular neighborhood, e.g., $3 \times 3 \times 3$, and the weighting function ω is symmetric, we can construct the surrogate function of the general penalty term $R(\theta)$ as defined in (4.3) by replacing u with a well-behaved transformation $T(\theta)$ as defined in Section 4.3.2 as follows:

$$S_{pen}(\theta|\theta^n) = \frac{1}{2}\sum_{q=1}^{Q}\frac{1}{\sigma_q^2}\sum_{j=1}^{J}\omega_j^{reg}(T_q(\theta_j) - T_{jq}^{reg,n}(\theta^n))^2$$

with $\omega_j^{reg} = \sum_{k\in\mathcal{N}_j}\omega_{jk}$ and

$$T_{jq}^{reg,n}(\theta^n) = \frac{1}{2\omega_j^{reg}}\sum_{k\in\mathcal{N}_j}\omega_{jk}(T_q(\theta_j^n) + T_q(\theta_k^n))$$

is the image generated by ω-weighted smoothing of the corresponding image from the previous iteration.

4.3.3.3 Algorithm for MAP direct reconstruction.

Combining the separately derived surrogate functions from above, the original likelihood optimization problem is transferred to the optimization of the overall surrogate function given by

$$\theta^{n+1} = \arg\max_{\theta}\ S_{log}(\theta|\theta^n) - \alpha S_{pen}(\theta|\theta^n) \qquad (4.11)$$

Since the sum of two separable surrogate functions is again separable this problem can be solved by independent voxel-wise fitting as follows:

$$\begin{aligned}
\theta_j^{n+1} = \arg\max_{\theta_j}\Bigg[& s_j\left(\sum_{m=1}^{M} x_{jm}^{em,n}\log x_m(\theta_j) - x_m(\theta_j)\right) \\
& - \frac{\alpha}{2}\sum_{q=1}^{Q}\frac{1}{\sigma_q^2}\omega_j^{reg}(T_p(\theta_j) - T_{jp}^{reg,n}(\theta^n))^2\Bigg]
\end{aligned} \qquad (4.12)$$

Thus, the algorithm is split into a regular MLEM update $x_j^{em,n} = \{x_{jm}^{em,n}\}_{m=1}^{M}$ that contributes to the S_{log} penalty, followed by a voxelwise fitting step which solves the optimization problem in (4.11).

4.3.4 Scaling Parameter Estimation

When regularization is to be applied to M activity and T parametric images simultaneously (cf. Section 4.3.2.1), the problem of scaling arises in order to penalize each image appropriately. We applied established techniques to reduce this $(M+T)$-dimensional space to two configuration parameters for practical reasons.

Regularization of each kinetic parameter is controlled by the constants σ_p^2, $p = 1, \ldots, P$ as follows [104][105]:

$$\sigma_p^2 = \frac{1}{N} \sum_{j=1}^{J} \sum_{k \in \mathcal{N}} \omega_{jk} |T_p(\theta_j^{orig}) - T_p(\theta_k^{orig})|^2$$

where N is the number of nonzero voxels in the image and θ^{orig} are the original parametric images.

It would be natural to scale regularization for all images equally. However, we found that trading off activity with parametric regularization results in better images. Thus, we split our prior and the parameter α into two parts: regularization of parametric images, each scaled as outlined above and globally controlled by γ, and regularization on the activity, each frame weighted according to its variance σ_m^2 calculated as the ratio of the measured counts divided by the squared frame duration, as also suggested by [119]. The latter is globally controlled by β. The resulting form is

$$\begin{aligned} \theta_j^{n+1} = \arg\max_{\theta_j} \Bigg[& s_j \left(\sum_{m=1}^{M} x_{jm}^{em,n} \log x_m(\theta_j) - x_m(\theta_j) \right) \\ & - \frac{\beta}{2} \sum_{m=1}^{M} \frac{1}{\sigma_m^2} \omega_j^{reg} (x_m(\theta_j) - x_{jm}^{reg,n}(\theta^n))^2 \\ & - \frac{\gamma}{2} \sum_{p=1}^{P} \frac{1}{\sigma_p^2} \omega_j^{reg} (T_p(\theta_j) - T_{jp}^{reg,n}(\theta^n))^2 \Bigg]. \end{aligned} \tag{4.13}$$

4.3.5 Analytical Tissue Compartment Modeling using Feng's input function model

The measured TAC, C_T, can be modeled as the tracer's concentration in the arterial blood, the blood input function C_p, convolved with an *impulse response function (IRF)* h:

$$C_T(t) = (1 - V_B)h(t) \otimes C_p(t) + V_B C_p(t) \tag{4.14}$$

with a blood volume term V_B to account for the contribution of vascular tracer activity in the total tissue concentration. In this work we used a nonlinear 2TC model for data fitting comprising an arterial blood and two tissue compartments each of them related to an anatomical, physiological or biochemical state of the tracer. The IRF of a 2TC model is given by

$$h(t) = B_1 e^{-L_1 t} + B_2 e^{-L_2 t}$$

From the parameter vector $\theta = (B_1, B_2, L_1, L_2, V_B)$ the micro-kinetic parameters K_1, k_2, k_3, k_4 are calculated by [104]

$$\begin{aligned} K_1 &= B_1 + B_2, \qquad k_2 = (B_1 L_1 + B_2 L_2)/(B_1 + B_2), \\ k_3 &= \frac{(B_1 L_2 + B_2 L_1)}{(B_1 + B_2)} - \frac{(L_1 L_2 (B_1 + B_2))}{(B_1 L_1 + B_2 L_2)}, \\ k_4 &= (L_1 L_2 (B_1 + B_2))/(B_1 L_1 + B_2 L_2). \end{aligned}$$

They describe the tracer's exchange between individual compartment, e.g., K_1 is the forward exchange rate from the blood pool into the first tissue compartment. The macro-parameter $K_i = (K_1 k_3)/(k_2 + k_3)$ is also often of interest. The transformations $T_p(\theta) := k_p(\theta)$ can be used for regularization as described in Section 4.3.2.1.

The convolution operation in (4.14) can be computed more efficiently when discretization is avoided. Therefore, we used the analytical Feng input function model [72] given by

$$C_p(t) = (A_1 t - A_2 - A_3)e^{\lambda_1 t} + A_2 e^{\lambda_2 t} + A_3 e^{\lambda_3 t} \tag{4.15}$$

with amplitude vector $A = (A_1, A_2, A_3)^T$ and inverse time constant vector $\lambda = (\lambda_1, \lambda_2, \lambda_3)^T$. This allows us to derive the convolution operation analytically by

$$\begin{aligned} O(t) &= \left[C_p \otimes \sum_{i=1}^{2} B_i e^{-L_i t} \right](t) \\ &= \sum_{i=1}^{2} \frac{A_1 t B_i}{(L_i - \lambda_1)} e^{-\lambda_1 t} + \sum_{i=1}^{2} \sum_{j=1}^{3} \frac{\hat{A}_j B_i}{(L_i - \lambda_j)} \left(e^{-\lambda_j t} - e^{-L_i t} \right) \end{aligned}$$

where $\hat{A} = (-A_2 - A_3 - \frac{A_1}{(\theta_i - \lambda_1)}, A_2, A_3)$. Now, the measured integral over $O(t)$ from start time t_s to end time t_e for each frame with length I can be calculated as

$$\begin{aligned} M(t_s, t_e) &= \frac{1}{I}\int_{t_s}^{t_e} O(t) \\ &= \frac{1}{I}\sum_{i=1}^{2}\left(\sum_{j=1}^{3}\frac{\hat{A}_j B_i}{(L_i - \lambda_j)}\left(\frac{e^{-L_i t_e} - e^{-L_i t_s}}{L_i} - \frac{e^{-\lambda_j t_e} - e^{-\lambda_j t_s}}{\lambda_j}\right)\right. \\ &\left. + \frac{A_1 B_i\left(e^{-\lambda_1 t_s}(\lambda_1 t_s + 1) - e^{-\lambda_1 t_e}(\lambda_1 t_e + 1)\right)}{\lambda_1^2 (L_i - \lambda_1)}\right) \end{aligned} \tag{4.16}$$

We also calculated the TAC's Jacobian analytically to improve optimization. The derivatives of M in Equation 4.16 with respect to $B_k, k = 1, 2$ and $L_k, k = 1, 2$ are as follows, where $\bar{A} = (-A_2 - A_3, A_2, A_3)$:

$$\begin{aligned} \frac{\partial M}{\partial B_k} =& \frac{1}{I}\left[\sum_{j=1}^{3}\frac{\hat{A}_j}{(L_k - \lambda_j)}\left(\frac{e^{-L_k t_e} - e^{-L_k t_s}}{L_k} - \frac{e^{-\lambda_j t_e} - e^{-\lambda_j t_s}}{\lambda_j}\right)\right. \\ &\left. + \frac{A_1\left(e^{-\lambda_1 t_s}(\lambda_1 t_s + 1) - e^{-\lambda_1 t_e}(\lambda_1 t_e + 1)\right)}{\lambda_1^2 (L_k - \lambda_1)}\right] \\ \frac{\partial M}{\partial L_k} =& \frac{B_k}{I}\sum_{j=1}^{3}\left[\frac{\bar{A}_j}{(L_k - \lambda_j)^2}\left(\frac{e^{-\lambda_j t_e} - e^{-\lambda_j t_s}}{\lambda_j} - \frac{e^{-L_k t_e} - e^{-L_k t_s}}{L_k}\right)\right. \\ &\left. - \frac{\bar{A}_j}{(L_k - \lambda_j)}\left(\frac{t_e e^{-L_k t_e} - t_s e^{-L_k t_s}}{L_k} + \frac{e^{-L_k t_e} - e^{-L_k t_s}}{L_k^2}\right)\right] \\ &- \frac{1}{I}\frac{2A_1 B_k}{(L_k - \lambda_j)^3}\left(\frac{e^{-\lambda_j t_e} - e^{-\lambda_j t_s}}{\lambda_j} - \frac{e^{-L_k t_e} - e^{-L_k t_s}}{L_k}\right) \\ &+ \frac{1}{I}\frac{A_1 B_k}{(L_k - \lambda_j)^2}\left(\frac{t_e e^{-L_k t_e} - t_s e^{-L_k t_s}}{L_k} + \frac{e^{-L_k t_e} - e^{-L_k t_s}}{L_k^2}\right) \\ &- \frac{1}{I}\frac{A_1 B_k\left(e^{-\lambda_1 t_s}(\lambda_1 t_s + 1) - e^{-\lambda_1 t_e}(\lambda_1 t_e + 1)\right)}{\lambda_1^2 (\lambda_1 - L_k)^2} \end{aligned}$$

4.4 Methods

4.4.1 Simulation study for [^{18}F]FDG

A 2D dynamic brain phantom was generated using the BrainWeb database [12][53], which provides both tissue segmentation and unsegmented, simulated MR scans. The noise free MR image of the selected slice with white and gray matter regions and an added tumor region is shown in Fig. 4.2b.

The dynamic activity phantom simulates [^{18}F]FDG uptake in the brain using a 2TC model with kinetic parameter values reported in literature [187] and given in units [min^{-1}]: $K_1 =$

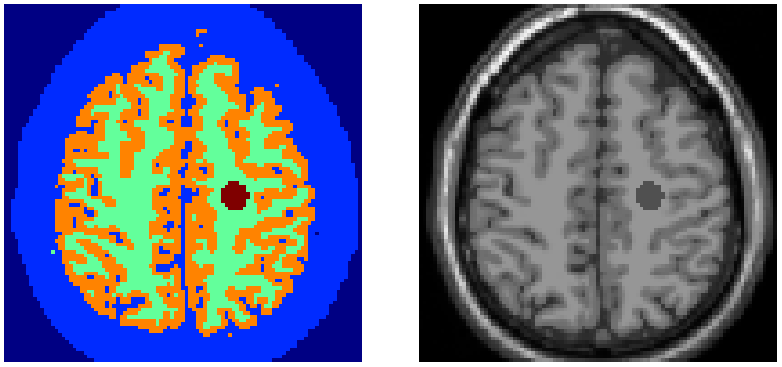

(a) Original activity (b) MR

Figure 4.2: Simulated (a) true [^{18}F]FDG activity distribution for a late time frame and (b) corresponding T_1-weighted MR image.

0.059, $k_2 = 0.149$, $k_3 = 0.090$, $k_4 = 0.013$ for white matter; $K_1 = 0.116$, $k_2 = 0.254$, $k_3 = 0.116$, $k_4 = 0.011$ for gray matter; $K_1 = 0.088$, $k_2 = 0.055$, $k_3 = 0.096$, $k_4 = 0.001$ for the tumor region. The Feng input function was derived from $A_1 = 851.1225$ [ml^{-1}min^{-1}], $A_2 = 21.87$ [ml^{-1}], $A_3 = 20.8$ [ml^{-1}], $\lambda_1 = 4.13$ [ml^{-1}], $\lambda_2 = 0.119$ [ml^{-1}], $\lambda_3 = 0.01$ [ml^{-1}]. The blood volume fraction was set to zero for all regions. The simulated total scan time of 60 min was divided into 24 frames [187]: 4×20 s, 4×40 s, 4×60 s, 4×180 s, and 8×300 s. For each ROI the calculated TACs were integrated over the individual frame intervals and normalized by the frame length. The sampled activity values were assigned to the phantom regions shown in Fig. 4.2a.

An analytically computed 2D system matrix reflecting the mMR's scanner geometry [63] with a detector size of 4 mm was implemented based on an area weighted strip integral calculation. It was used to forward project the dynamic images to a sequence of sinograms with 344 bins and 252 angles. After scaling the sinograms to a total of 60 million counts over the total scan time, Poisson noise was added to the sinograms. The effect of attenuation as well as scatter and random events was not considered in the simulation study.

The MR image was resampled to a voxel size of 1.66×1.66 mm to match the resolution of the reconstructed PET image with a matrix size of 128×128. As seen in Fig. 4.2b the simulated MR image is not segmented and has smooth transitions between tissue regions.

4.4.2 Algorithm Implementation

All reconstructions were performed with an in-house developed C++ reconstruction framework for sinogram data [1] specific to the mMR scanner. It was extended for the proposed algorithms. PET images were reconstructed with a 2D MLEM implementation. Images were initialized by setting all k parameters to 0.01. The MR image was used to exclude

background voxels from fitting to speed up the algorithm. Direct reconstruction results were obtained for 500 and 400 MLEM iterations for phantom data and clinical data, respectively. 5 nonlinear fitting iterations were performed after each MLEM iteration. In the indirect approach each frame was reconstructed with Green's one step late OSL-MAP-EM algorithm [86] using a conventional, distance-weighted smoothing prior for 63 iterations (Post). Up to 1000 iterations of the Levenberg-Marquardt algorithm were used for fitting. We note that the OSL-implementation does not guarantee convergence and is only shown for the reader's convenience. Our main benchmark for comparison is the direct distance-weighted method (PenA), which was already shown to be superior to the indirect approach (Post) [187].

Regularization was applied to 8 neighbors in the 2D phantom study and 26 neighbors for the 3D clinical data. We introduce the notation $Pen\{B|A|P\}$ to refer to different combinations of weighting and regularization in our penalized likelihood algorithm (4.13), where

- B $\widehat{=}$ Bowsher-weighted, i.e., anatomy-driven regularization (cf. Section 4.3.2.2). Combinations without (B) use distance-weighted regularization instead.
- A $\widehat{=}$ regularization applied to activity images and controlled by β.
- P $\widehat{=}$ regularization applied to micro-kinetic parameter K_1, k_2, k_3, k_4 images and controlled by γ.

Analytic convolution with Feng's input model was used (cf. Section 4.3.5) to speed up computation. Both the function value and derivatives with respect to B and L were calculated (see Appendix 4.1). Numerical problems arise in two cases: When the exponential parameters of the IRF (θ_i) and of the Feng function (λ_j) are very similar, division by a very small number or zero occurs; this was addressed with linear interpolation over the instability region. Exponentials may become very small/large; this was addressed with 80-bit arithmetic (*long double*) in addition to grouping similar magnitudes.

The fitting problem in (4.12) can be solved by any nonlinear optimization algorithm. For the work presented here, we used a preconditioned conjugate gradient algorithm from the open source C++ library ALGLIB [32], BLEIC. BLEIC uses the active set method for bound constrained optimization. The function value and gradient of the objective function was given as input to the algorithm as well as the approximate scale of each parameter B, L, V_B. Default stopping conditions were used.

4.4.3 Quantitative Analysis

We performed an analysis both for the entire brain in terms of voxel-based measures to quantify reconstruction quality and for the tumor ROI in terms of ROI-based measures to assess ROI quantification. $N = 100$ independent noise realizations were generated.

Voxel-based mean absolute bias [182] and *normalized standard deviation (NSD)* for a given homogeneous ROI with M_{ROI} voxels were defined as follows

$$\%Mean|Bias| = \frac{\frac{1}{M_{ROI}} \sum_{j \in ROI} \left| \frac{\sum_{n=1}^{N} (X_j^n - X_j^{true})}{N} \right|}{(\bar{X}^{true})^{ROI}} \times 100\%$$

$$\%NSD = \frac{\frac{1}{M_{ROI}} \sqrt{\frac{1}{N-1} \sum_{n=1}^{N} (X_j^n - \bar{X}_j)^2}}{\bar{X}^{ROI}} \times 100\%$$

where X_j^n is the intensity in voxel j from the nth realization, $\bar{X}_j$ is the mean intensity in voxel j over all realizations, , and $\bar{X}^{ROI}$ is the mean intensity in the ROI over all realizations. The true intensity is given by X_j^{true} and $(\bar{X}^{true})^{ROI}$. In order to compute $\%Mean|Bias|$ and $\%NSD$ for the entire brain (including tumor), each ROI was calculated separately and then the weighted average was calculated according to the respective size in voxels of each ROI.

For tumor ROI quantification the normalized bias and *standard deviation (STD)* in the tumor ROI was calculated as [162]

$$\%Bias_{ROI} = \frac{1}{N} \sum_{n=1}^{N} \frac{|\bar{X}_n^{ROI} - (\bar{X}^{true})^{ROI}|}{(\bar{X}^{true})^{ROI}} \times 100\%$$

$$\%STD_{ROI} = \frac{\sqrt{(\sum_{n=1}^{N} (\bar{X}_n^{ROI} - \frac{1}{N} \sum_{i=1}^{N} \bar{X}_n^{ROI}))^2}}{(\bar{X}^{true})^{ROI}} \times 100\%$$

where $\bar{X}_n^{ROI}$ is the mean reconstructed intensity in the ROI from the nth realization.

As a unified measure to evaluate reconstruction error for parametric images of different magnitude, the *normalized root mean squared error (nRMSE)* was used [162]

$$nRMSE = \frac{\sqrt{\sum_{j=1}^{J} (X_j - X_j^{true})^2}}{\sqrt{\sum_{j=1}^{J} (X_j^{true})}}$$

For all quantitative evaluation plots β was varied to include 0.0 and then from 0.00003 to 0.03 (.1 for PenBA), γ was varied to include 0 and then from 100 to 10000, each in 3/10 increments.

4.4.4 Evaluation on clinical [^{18}F]FET PET/MR data

Clinical data were acquired on a Siemens Biograph mMR PET/MR scanner in list mode for 40 min after injection of 180 MBq of [^{18}F]FET. The data were binned into 9 × 10 s, 3 × 30 s, 1 × 120 s, 3 × 300 s, 2 × 600 s frames. The 3D emission sinograms were fully pre-corrected for attenuation (Dixon sequence), scatter, randoms, and normalization using vendor software, and converted to 2D sinograms using Fourier rebinning. A structural MR image was simultaneously acquired with a T_1-weighted gadolinium-enhanced MPRAGE sequence, and used as input for the anatomical prior. The MR image was co-registered to a single OSEM (3 iterations × 21 subsets) reconstructed PET image using rigid mutual information based registration in PMOD [13]. Both PET and MR 3D images had 1.0 × 1.0 × 2.03 mm voxel size and 255 × 255 × 110 voxels. A 2TC model including a blood volume term was used for data fitting. An input function was derived from independently reconstructed PET frames (OSEM) by delineating an internal carotid ROI on the MR image. The Feng model in (4.15) was fitted to the data.

4.5 Results

4.5.1 Simulation study for [^{18}F]FDG

4.5.1.1 Distance-weighted vs. Bowsher-weighted regularization

We assessed the advantage of our Bowsher-weighted regularization over the established distance-weighted regularization, with regularization applied to activity images only (PenA, cf. [187]) or to activity and parameters K_1 to k_4 simultaneously (PenAP, as proposed in this work). The methods are summarized in Table 4.1. Regularization parameters were chosen as to yield lowest reconstruction error (nRMSE) summed over K_1, k_2 and K_i images for all considered parameter values (cf. Section 4.4.3) after 500 iterations. For this choice, k_3 and k_4 images were excluded as they have very little contrast and the model is nearly irreversible. The advantage in terms of summed nRMSE of adding Bowsher regularization to activity (PenBA) was 22 %, and 24 % for simultaneous regularization (PenBAP). Bowsher-weighted regularization allowed for larger values of β and γ. As the effect of simultaneous regularization is partially cumulative, those methods used smaller β values. Due to different methods of estimating scaling (see Section 4.3.4) β and γ vary by several orders of magnitude.

Figure 4.3a shows that good convergence has been achieved after 500 iterations for the considered parameter combinations and the chosen metric. Convergence for the k_2 image

Table 4.1: Lowest achieved nRMSE summed over K_1, k_2 and K_i images, averaged over 100 noise realizations.

Method	β	γ	**nRMSE**
Post	0.001	-	0.884
PenA	0.03	-	0.800
PenBA	0.1	-	0.623
PenAP	0.0003	3000	0.647
PenBAP	0.001	3000	0.490

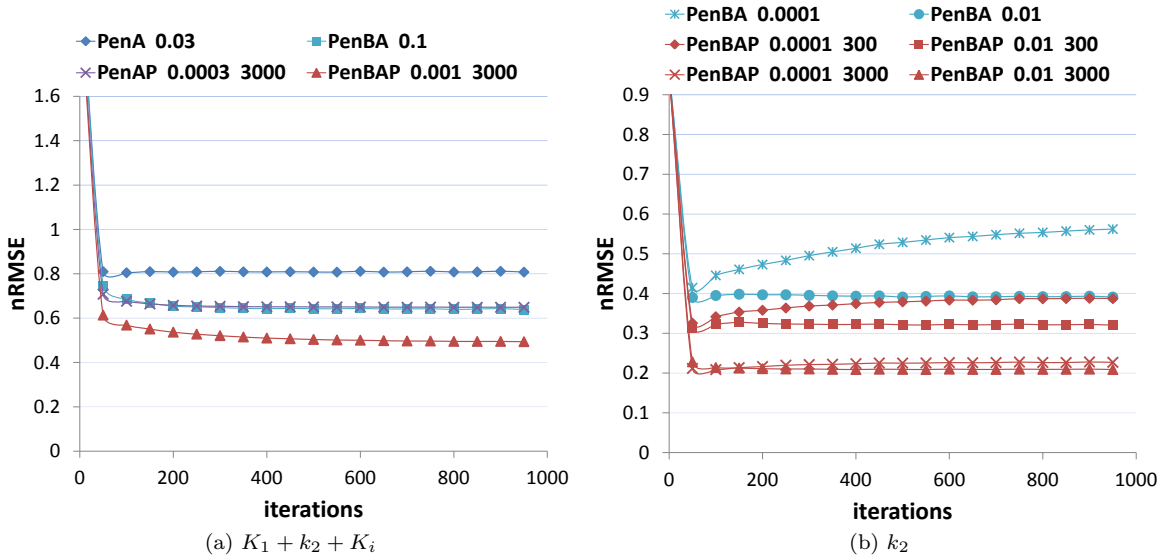

(a) $K_1 + k_2 + K_i$ (b) k_2

Figure 4.3: nRMSE representing total reconstruction error (a) summed over K_1, k_2 and K_i images and (b) plotted over 1000 iterations. The first parameter behind the algorithm name denotes β, the second parameter (if applicable) γ.

and varying parameter choices as in Figure 4.3b was also reasonable after 500 iterations even for weak activity regularization ($\beta = 0.0001$).

For visual assessment, true and reconstructed parametric images from a single noise realization for methods as in Table 4.1 are shown in Figure 4.4. As expected, the indirect method (Post) was outperformed by all direct approaches. Compared to the distance-weighted method (PenA) the Bowsher-weighted method (PenBA) visually led to better results especially at tissue borders. For k_2 and k_3, however, the structural information alone was not sufficient for adequate recovery.

Simultaneous regularization on activity and parameters (PenAP) gives superior results compared to PenA, and again Bowsher-weighted regularization (PenBAP) improved feature definition. The K_i image benefits significantly, even though it was not subject to regularization directly. This can also be seen from the line profiles in Figure 4.5.

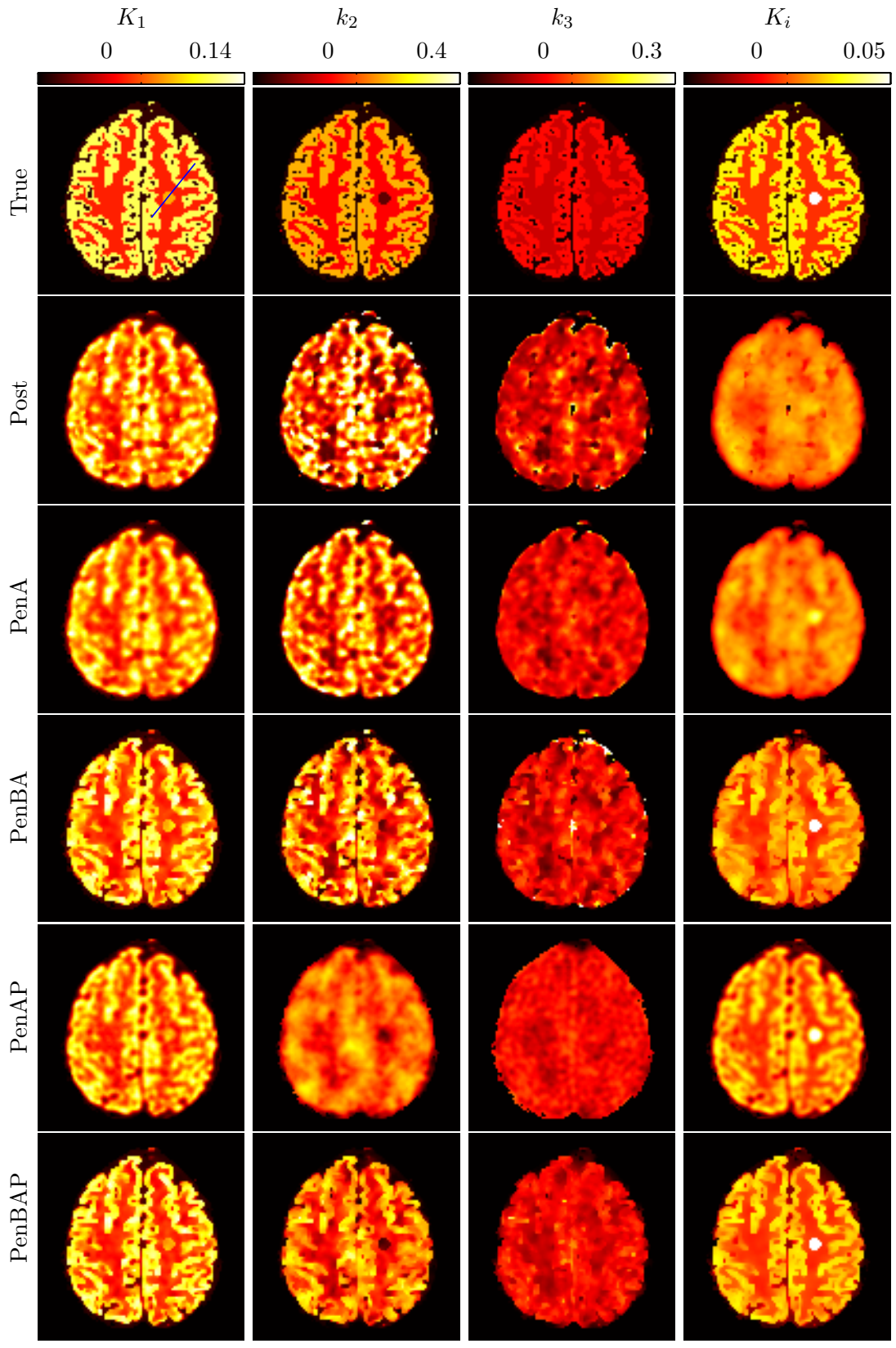

Figure 4.4: [^{18}F]FDG simulation: True parameters and reconstructed parametric images for methods Post ($\beta = 0.001$), PenA ($\beta = 0.03$), PenBA ($\beta = 0.1$), PenAP ($\beta = 0.0003, \gamma = 3000$), and PenBAP ($\beta = 0.001, \gamma = 3000$), see also Table 4.1.

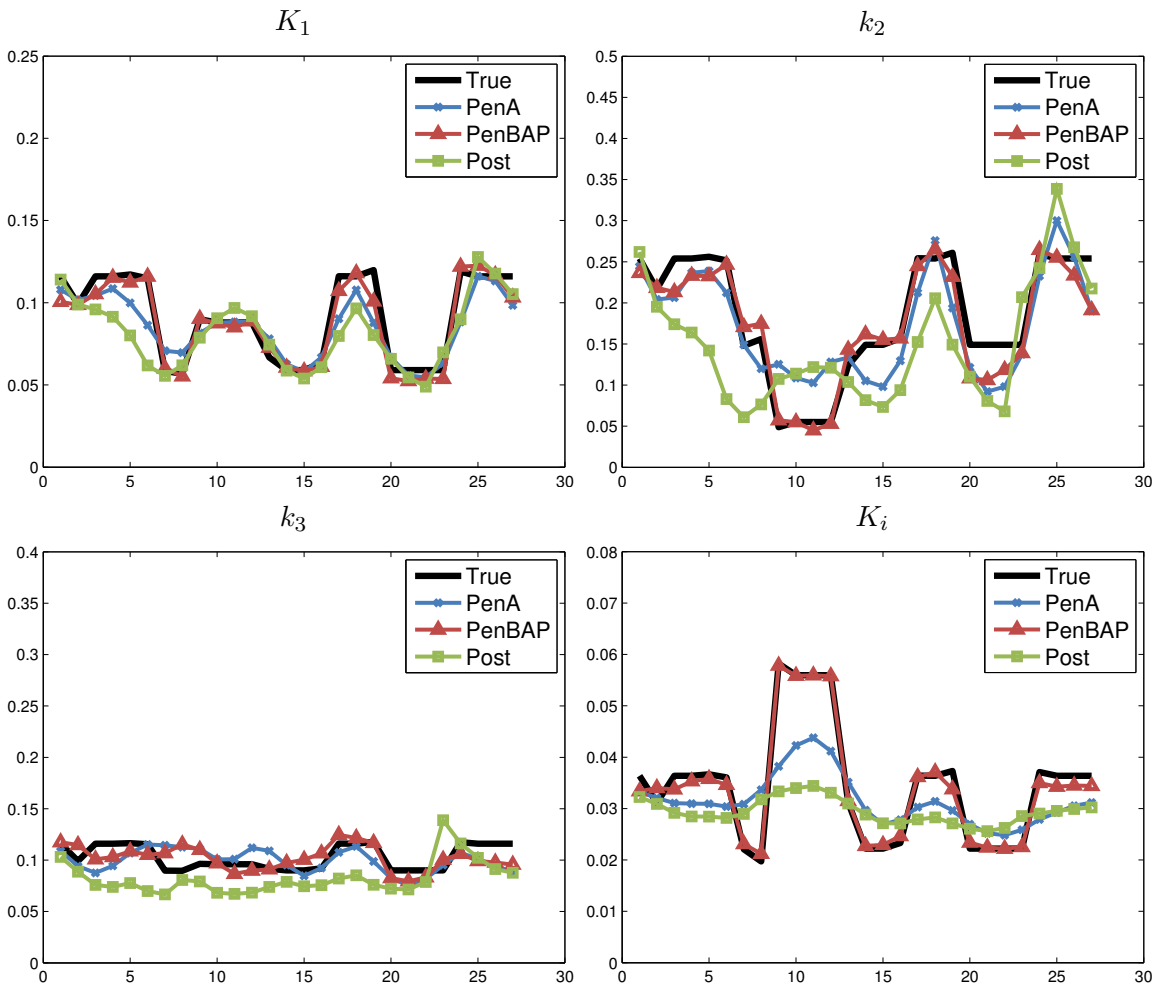

Figure 4.5: Line profiles across the tumor region for different methods shown in Figure 4.4 (voxels 9 to 12, line indicated in the true K_1 image in Fig. 4.4)

.

The advantage of the Bowsher-weighted methods can also be seen, e.g., for parameter k_2 from Figure 4.6. At a lower level of variance, lower bias on average over all realizations could be achieved, especially at tissue borders. Additional parameter regularization (PenBAP) decreased standard deviation further.

Figure 4.7 shows a quantitative bias-noise analysis for all methods by varying the parameters β and γ (ranges as in Section 4.4.3). Quantification with the voxel-based metric for the entire brain (left column) showed that Bowsher-weighted methods offer a significantly lower $\%Mean|Bias|$ than their distance-weighted counterparts. Adding parameter regularization (PenAP, PenBAP) directly resulted in decreased $\%NSD$ when compared to PenA resp. PenBA. ROI based quantification of the tumor region (right column) showed that adding Bowsher weighting (PenBA) to activity (PenA) alone decreased $\%Bias_{ROI}$ and $\%STD_{ROI}$ for small values of β, but the benefit was limited and standard deviation even increased for larger values. Simultaneous regularization (PenBAP) consistently decreased $\%Bias_{ROI}$ at a $\%STD_{ROI}$ comparable to the conventional PenA approach. Please note that the tumor in

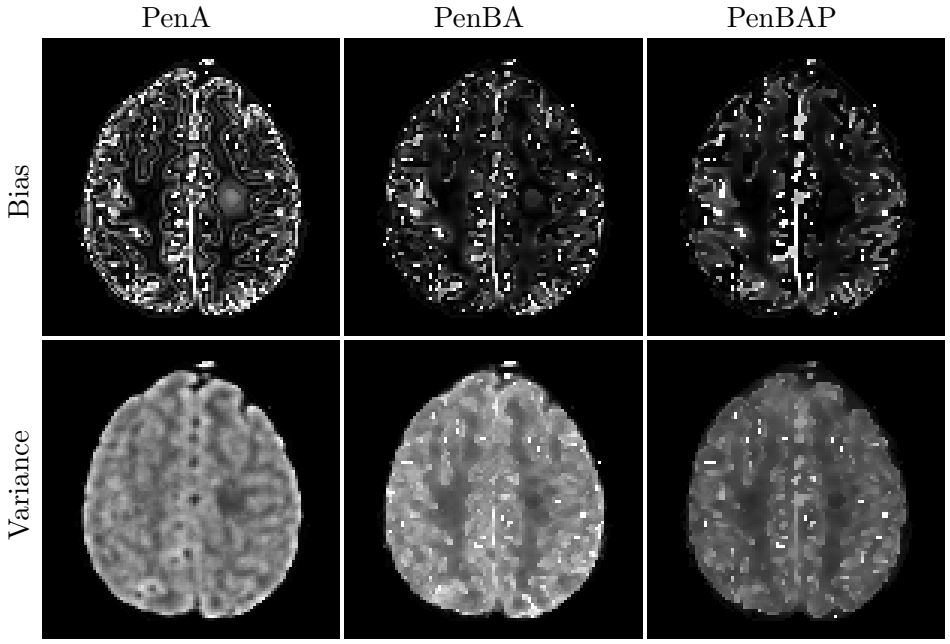

Figure 4.6: Bias and variance images of k_2 for PenA ($\beta = 0.03$), PenBA ($\beta = 0.1$), and PenBAP ($\beta = 0.001, \gamma = 3000$) methods as shown in Figure 4.4.

the k_2 image was a cold lesion, and that for the distance-weighted regularization methods the 0 % bias mark was crossed due to a small positive bias found in the K_1 image for unregularized direct reconstruction.

4.5.1.2 Activity vs. parametric regularization

The question arises if regularization is better applied to activity or directly to the parametric images, or, as is possible in our framework, to both simultaneously. We focussed on Bowsher-weighted methods since they proved superior in the evaluation of the last section.

The quantitative tradeoff as before is shown in Figure 4.8 for parameter only regularization (PenBP, γ varies), activity only regularization (PenBA, β varies) and simultaneous regularization ($\beta \in \{0.0001, 0.001\}$, γ varies) with parameter ranges as in Section 4.4.3. Quantification with the voxel-based metric for the entire brain (left column) revealed that PenBP was not able to match the other methods in terms of $\%Mean|Bias|$ (K_1) and $\%NSD$ (K_i), but performed well on the more unstable k_2 parameter. PenBAP exhibited best bias and NSD in all parameters, and for K_1 and k_2 there was an optimal value γ for each β in terms of bias. Especially the K_i image benefited from strong parameter regularization but only if a small amount of activity regularization was simultaneously applied (compare leftmost points for PenBP and PenBAP). ROI quantification (right column) showed PenBAP outperforming PenBP in terms of $\%STD_{ROI}$ and PenBA both in term of $\%Bias_{ROI}$

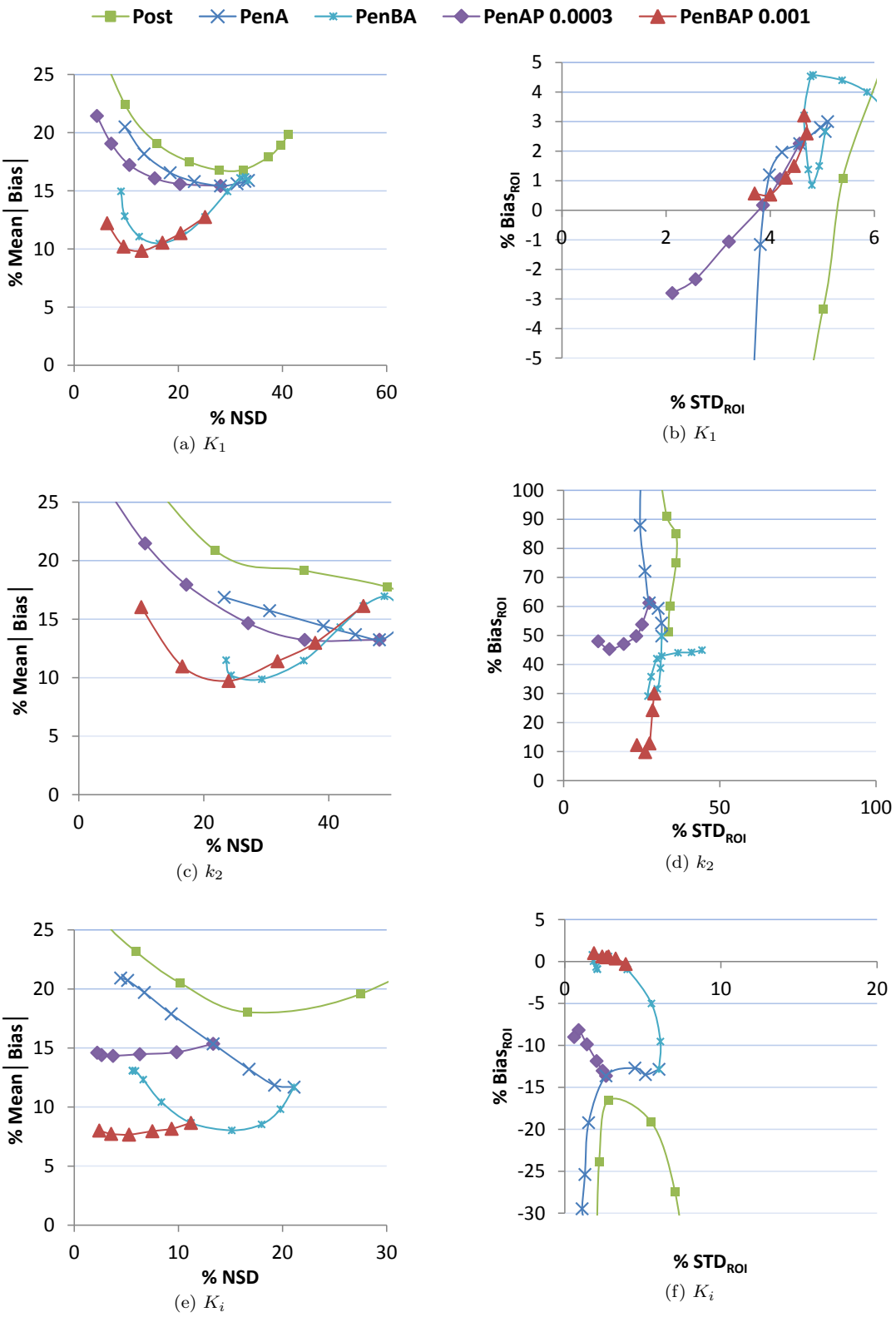

(a) K_1 (b) K_1

(c) k_2 (d) k_2

(e) K_i (f) K_i

Figure 4.7: Bias-noise analysis for K_1, k_2 and K_i images comparing all methods: (a), (c), (e) voxel-based quantification of entire brain; (b), (d), (f) tumor ROI quantification. Points on the curves correspond to different values of β (Post, PenA, PenBA) resp. γ (PenAP, PenBAP). Plots for methods PenA and PenBA coincide for $\beta = 0$, and the simultaneously regularized methods (PenAP, PenBAP) intersect their counterparts accordingly. In general, smallest β resp. γ values corresponds to highest $\%NSD$ resp. $\%STD_{ROI}$.

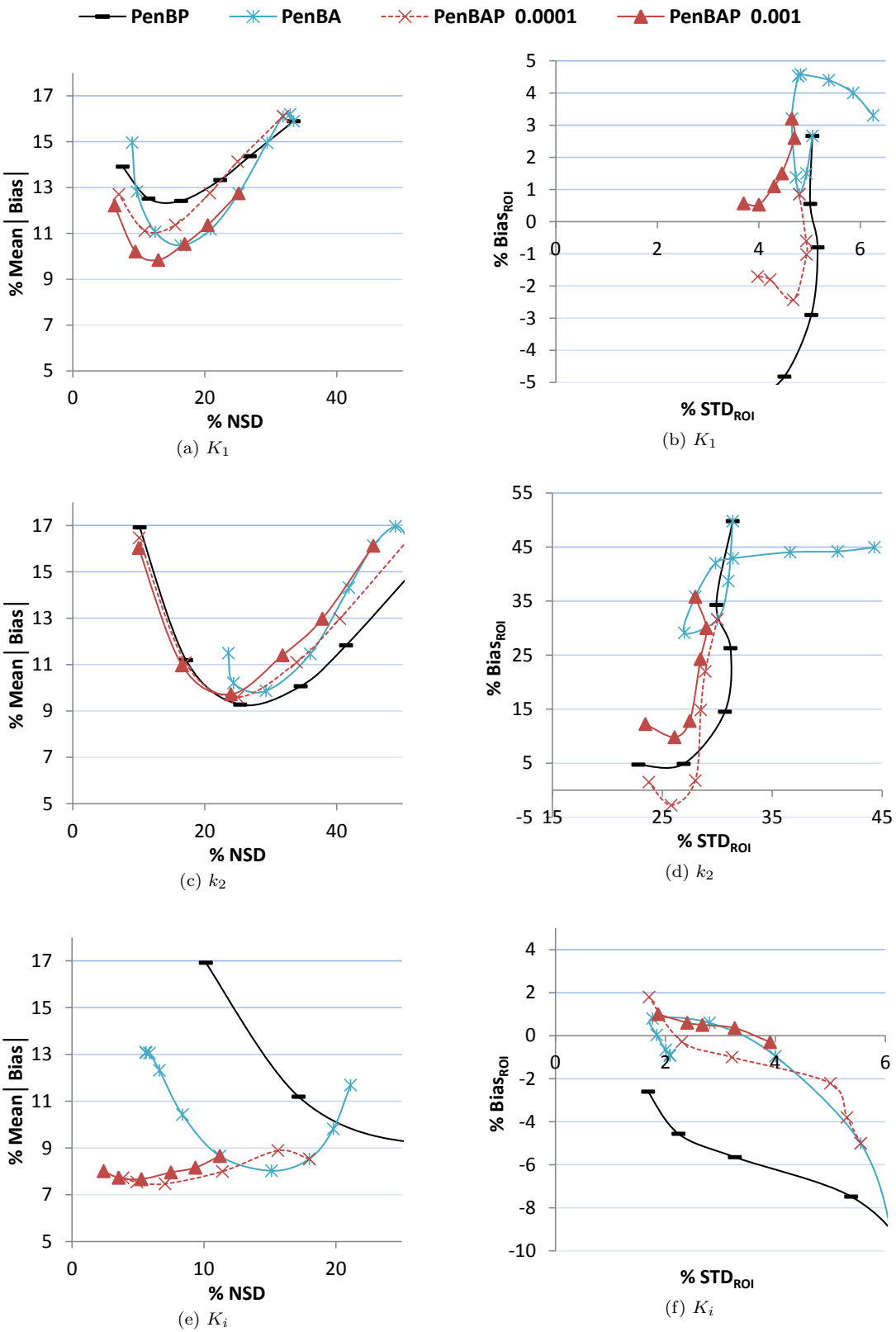

(a) K_1 (b) K_1

(c) k_2 (d) k_2

(e) K_i (f) K_i

Figure 4.8: Bias-noise analysis for K_1, k_2 and K_i images comparing PenBA, PenBP, PenBAP methods: (a), (c), (e) voxel-based quantification of entire brain; (b), (d), (f) tumor ROI quantification. Points on the curves correspond to different values of β (PenBA) resp. γ (PenBP, PenBAP). Plots for PenBAP intersect PenBA accordingly. In general, smallest β resp. γ values correspond to highest $\%NSD$ and $\%STD_{ROI}$.

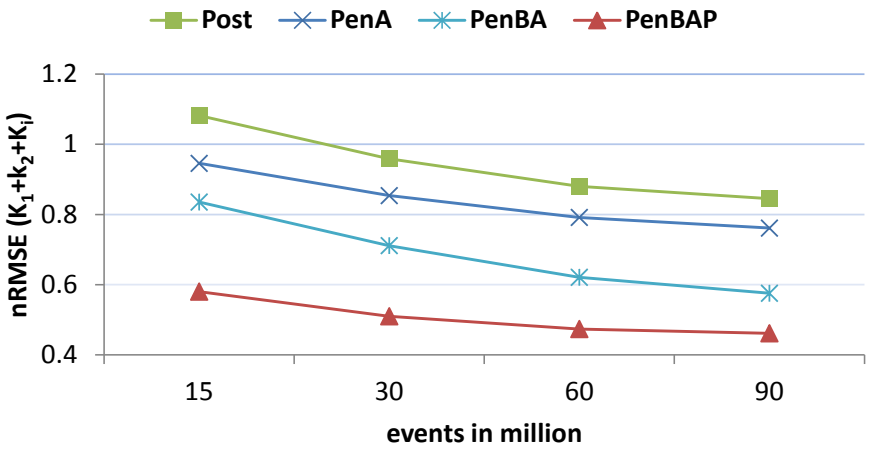

Figure 4.9: Lowest achieved nRMSE (summed over K_1, k_2, K_i, averaged over 10 realizations) at each considered statistics level for all considered parameter values.

and $\%STD_{ROI}$ for K_1 and k_2 images. The advantages were less obvious in the K_i image. In general (not shown in plots), simultaneous regularization with very strong activity regularization ($\beta > 0.01$) degraded results significantly.

Regularizing only a single parametric image has been proposed in literature. Our findings indicate that for parameters k_1 to k_3, single parameter regularization performed comparable to regularizing all parameters, if the amount of regularization (parameter γ) was increased by a factor of 3. In this case, non-regularized images did not benefit significantly. It is also possible to regularize only the combined parameter K_i in our framework, i.e., the penalty was derived from current estimate of parameters $K_1 - k_4$. However, simultaneous regularization was superior (NSD 7 % vs. 17 % at comparable best achievable mean bias), and even activity-only regularization was better (NSD 15 %), as also found in [34].

4.5.1.3 Impact of statistics

The impact of scan statistics was evaluated in terms of lowest achieved summed nRMSE at each statistics level, and results are shown in Figure 4.9. As expected, error increased with decreased statistics for all methods. PenBA was affected most (44 % increase from 90 million counts baseline to 15 million), while PenBAP remained as stable as PenA (23 % increase). Figure 4.10 shows the K_1 image generated with PenBAP at different noise levels. Increasing statistics decreased the patchiness of the Bowsher-weighted image and reveals greater detail.

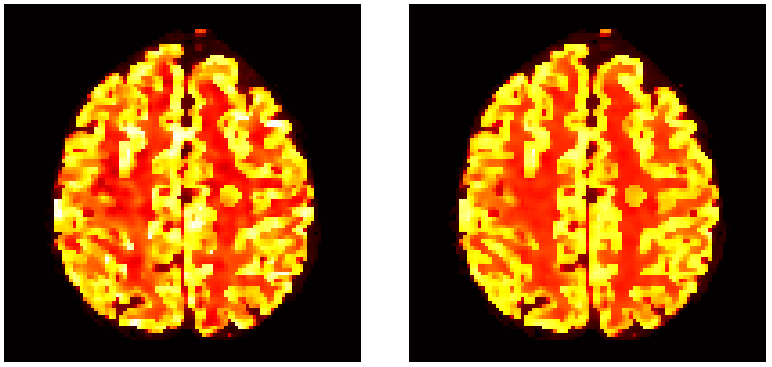

(a) 15M events (b) 90M events

Figure 4.10: Effect of increasing statistics from 15 (a) to 90 million events (b) on the K_1 image for PenBAP ($\beta = 0.001, \gamma = 10000$).

4.5.2 Clinical [^{18}F]FET PET/MR data

The methods were applied to a clinical dynamic [^{18}F]FET brain scan of a glioblastoma patient (cf. Section 4.4.4).

Figure 4.11 shows the benefit of direct (PenA, $\beta = 30$) and simultaneously regularized, Bowsher-weighted (PenBAP, $\beta = 100, \gamma = 0.003$) reconstruction over frame-independent reconstruction (MAP-OSL-EM, $\beta = 30$) for the activity image, and corresponding MR images. Please note that sinograms were in ECAT count scale, leading to different parameter ranges. The scaling coefficients σ_p for PenBAP were chosen experimentally to achieve comparable standard deviation in the parametric images in a homogeneous background ROI, which was defined in white matter (900 voxels altogether). Then, parameters for both direct methods were chosen to yield comparable standard deviation in the activity images in the same background ROI. Post exhibited more noise at the same value of β despite the good statistics available in the shown frame (600 s). PenBAP showed greater detail and better contrast. This becomes more apparent for the lesion image in Figure 4.12, that was rescaled to the dynamic range of the lesion. Only PenBAP revealed gray matter contrast and blood vessels. The tumor region is potentially heterogeneous, as is common with high grade Glioblastoma [140]. This was partially visible in the transverse and coronal activity image for Post in Figure 4.12, and clearly pronounced in the PenBAP activity image, assuming good MR correlation.

Parametric images were assessed for both the linear parameter K_1 (Fig. 4.13) and the nonlinear parameter k_3 (Fig. 4.14). It must be noted that FET achieved only small contrast between white and gray matter, but high contrast for lesions. K_1 images were reasonable for all approaches, with PenBAP showing less noise and revealing potential lesion detail such as the edema surrounding the tumor. The difference became larger for k_3, where only PenBAP was able to partially recover brain matter contrast in the full head image, and potentially

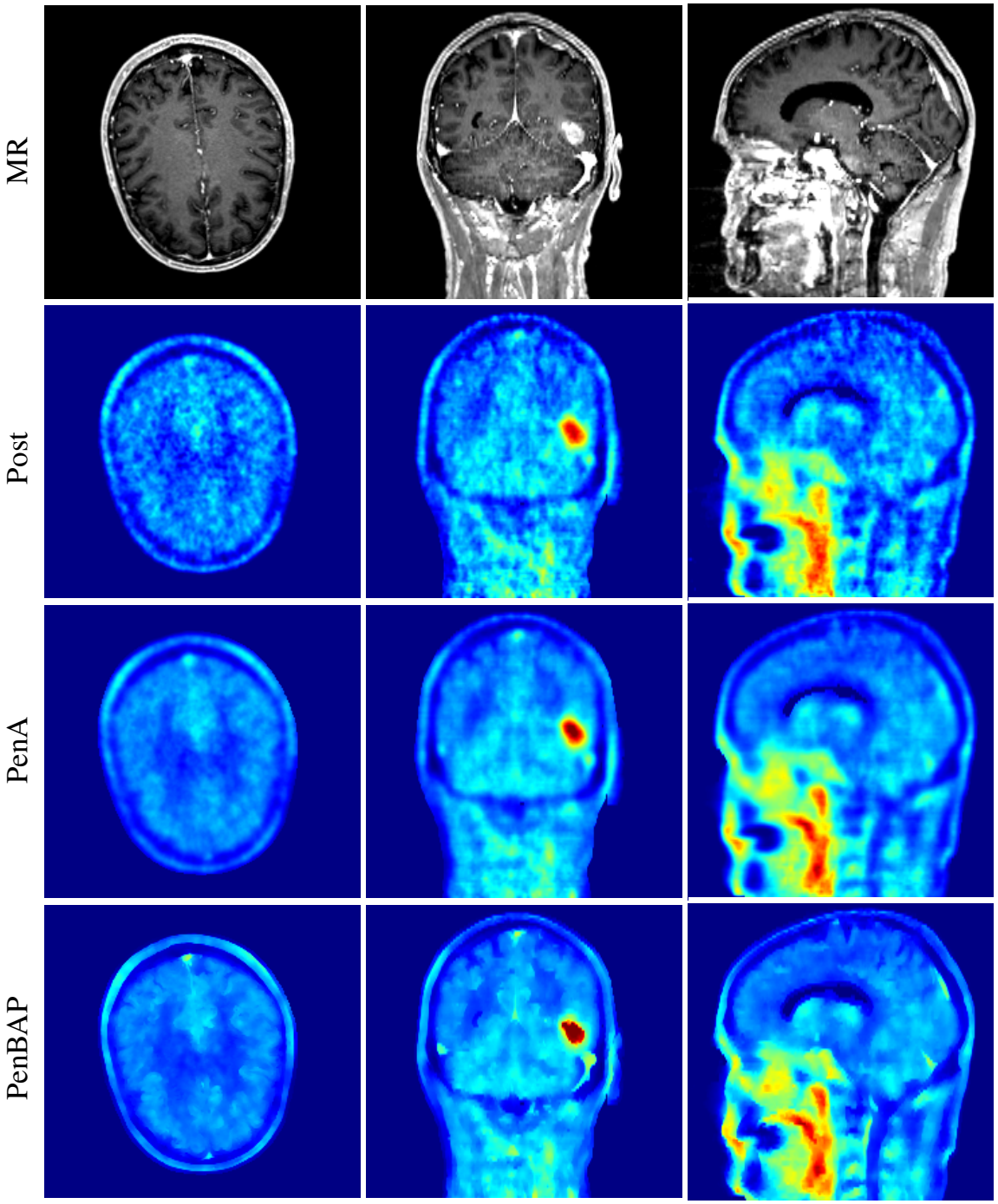

Figure 4.11: Glioblastoma patient data showing the MR image, and reconstructed [^{18}F]FET activity images (18th frame) obtained from frame-independent reconstruction, and direct reconstruction using the distance-weighted method (PenA) and the Bowsher-weighted method with simultaneous regularization (PenBAP). Columns represent transverse, sagittal, and coronal slices of the 3D volume.

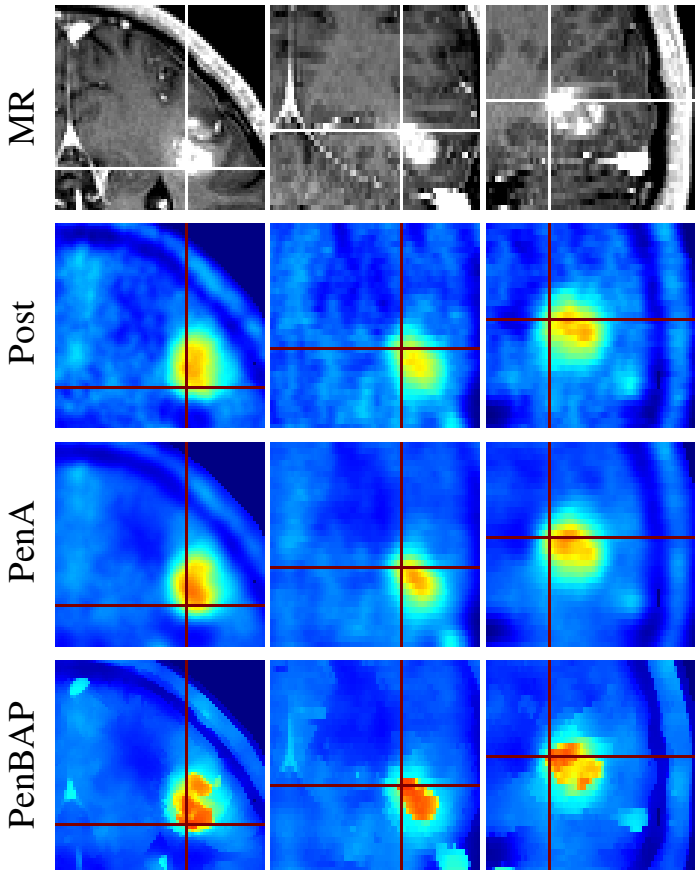

Figure 4.12: A section of the brain from Figure 4.11 showing the lesion with the corresponding MR image. Transverse, sagittal, and coronal views are shown in columns.

distinguished between a high and low k_3 area in the tumor. The additional detail given by PenBAP assumes good MR correlation and needs further validation, e.g., by biopsy, in future work.

For quantitative analysis, in addition to the background ROI, a 60 % isocontour ROI was defined in the MR image for the main tumor region (900 voxels), corresponding to the hot region visible in the K_1 image. Figure 4.15 shows the K_1 contrast between tumor and background ROI over noise standard deviation in background, as iterations increase from 50 to 400. It can be observed that the Bowsher-weighted method converged to a higher contrast, while standard deviation was contained at a smaller level as the image was directly regularized.

4.6 Discussion

Direct methods outperformed the indirect Post method, as was to be expected from literature. Applying distance-weighted regularization to the activity images during direct

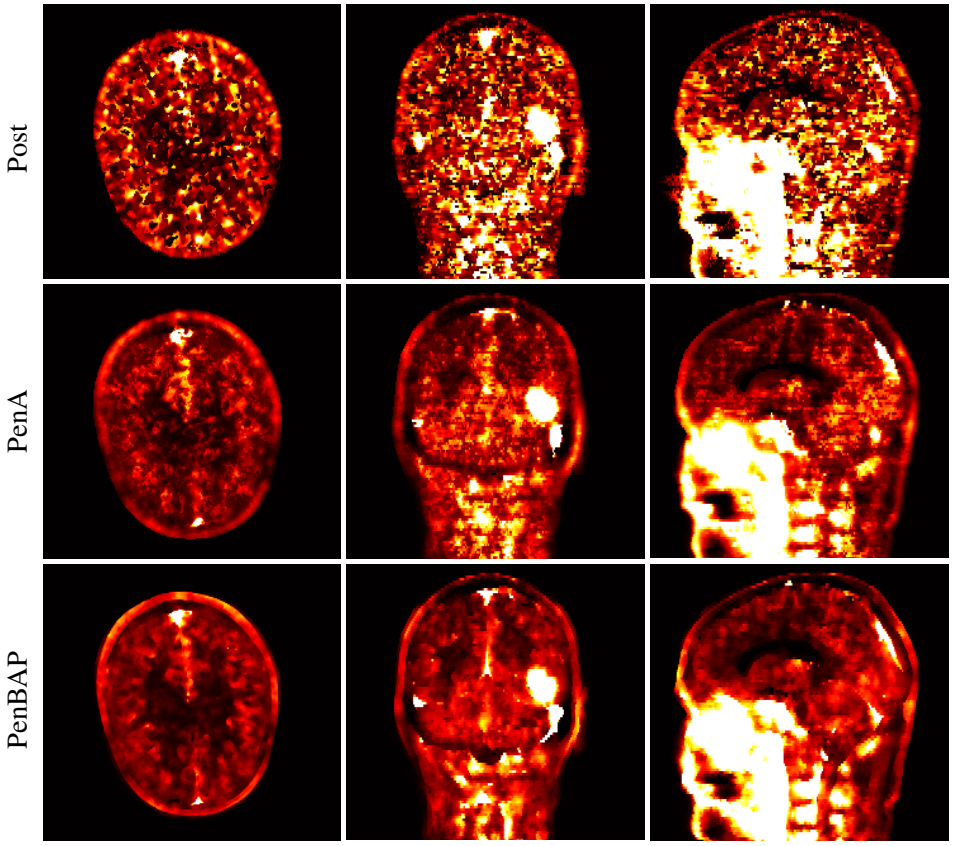

(a) K_1 parametric image

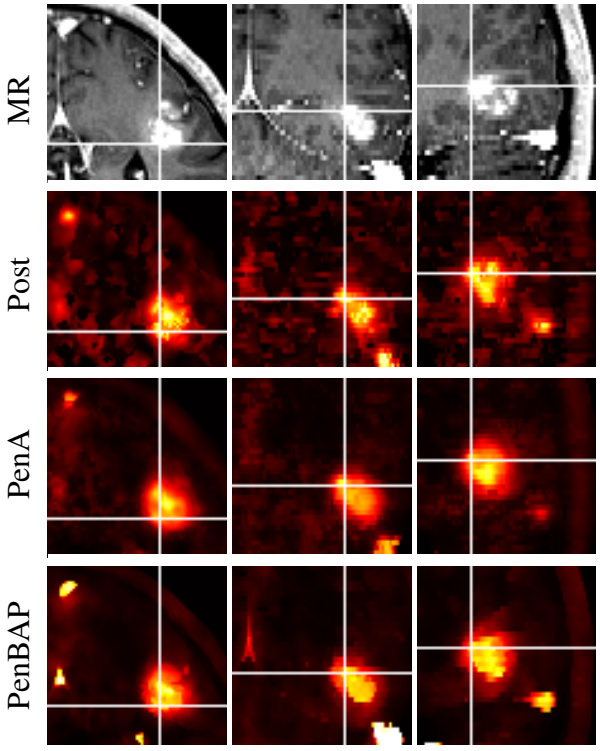

(b) Lesion from (a) and corresponding MR image.

Figure 4.13: K_1 image of a glioblastoma patient obtained from the indirect method (Post), and direct methods using distance-weighting (PenA) and Bowsher-weighting with simultaneous regularization (PenBAP). Columns represent transverse, sagittal, and coronal slices.

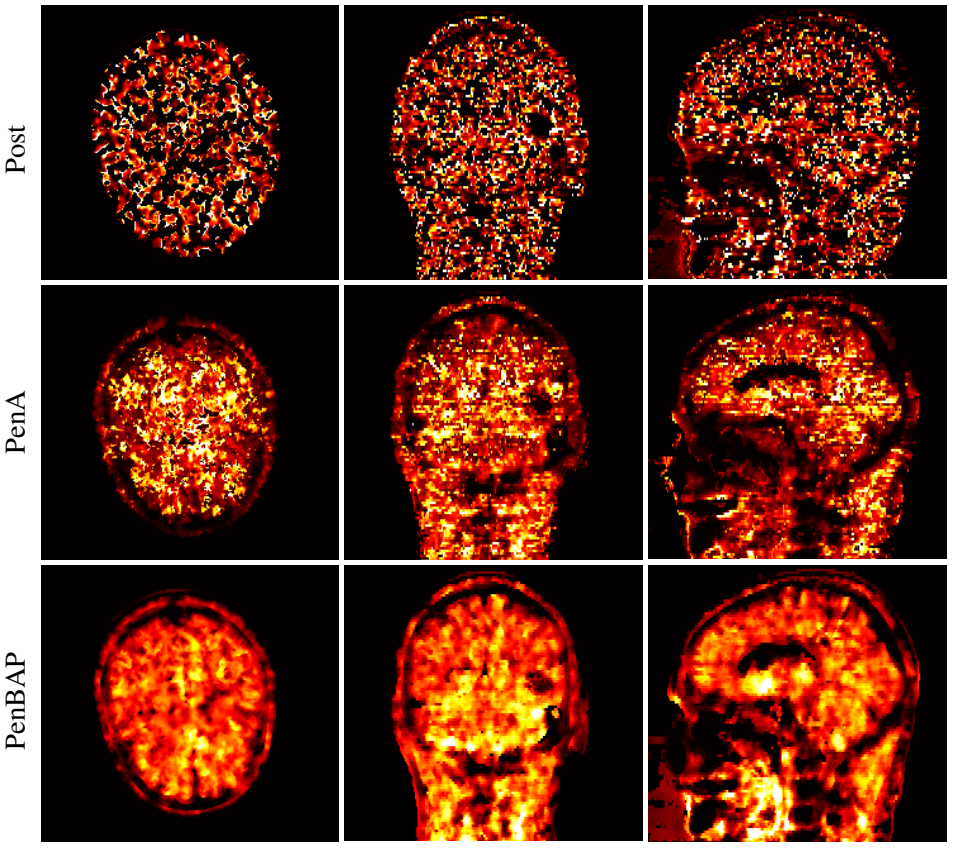

(a) k_3 parametric image

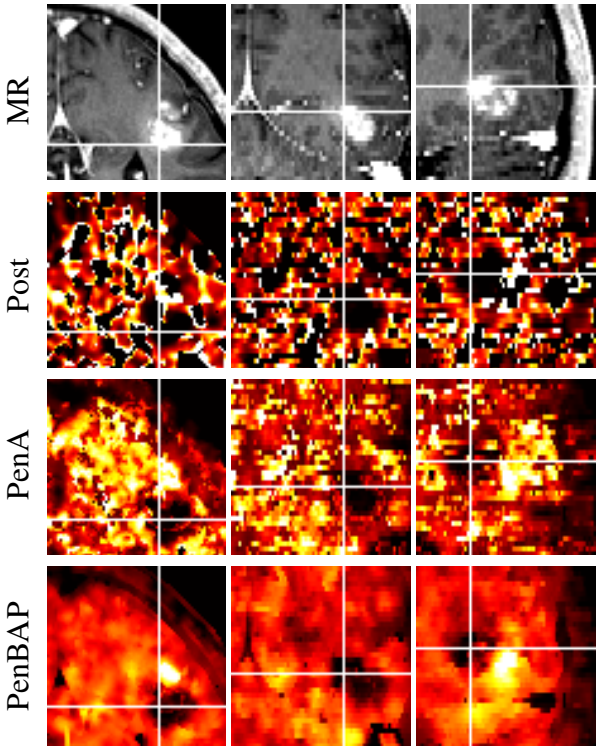

(b) Lesion from (a) and corresponding MR image.

Figure 4.14: k_3 image of a glioblastoma patient obtained from the indirect method (Post), and direct methods using distance-weighting (PenA) and Bowsher-weighting with simultaneous regularization (PenBAP). Columns represent transverse, sagittal, and coronal slices.

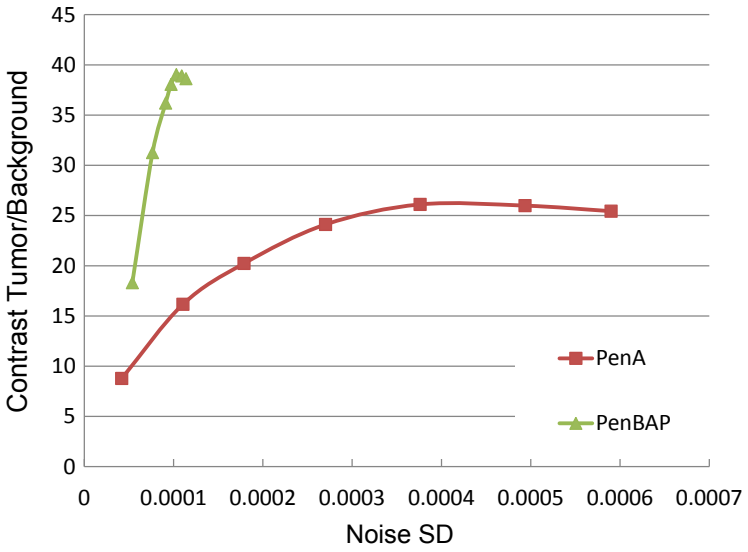

Figure 4.15: K_1 contrast tumor to background over noise standard deviation in background, as iterations are increased from 50 to 400 for PenA and PenBAP.

reconstruction as in [187] corresponds to our PenA method. We observed a good match of our k_3 and K_i images with the ones presented in [187] for the same FDG TAC model, albeit we can only show a different bias/noise tradeoff in this work (Fig. 4.4). Adding Bowsher regularization improved image quality, especially for stable parameters and activity images.

Regularizing parametric images directly is a promising approach. Typically, smoother images result, and model fitting is improved and more stable, if it can be assumed that similar voxels also have similar physiological function. Kamasak *et al.* [104] observed a clear advantage of directly reconstructing and regularizing parametric images K_1 to k_4 over post-fit, however, it is not clear if the advantage is due to the direct reconstruction or the regularization. They have recently re-assessed the validity of their approach [105]. Bousse *et al.* [34] found that anatomically regularizing the derived parameter K_i alone is not superior to anatomically regularizing activity. This is in line with our findings in Sec. 4.5.1.2. Even when all parameters K_1 to k_4 were regularized, K_i images had higher bias and error (cf. PenBP vs. PenBA in Fig. 4.8).

In our approach, if parametric images were regularized in addition to activity images simultaneously, superior images could be generated that exhibit less bias and noise at the same time. For example, PenBAP achieved the same combined reconstruction error (nRMSE) at only one sixth of the scan statistics as PenBA (cf. Fig. 4.9). Similarly, simultaneous regularization outperformed parameter-only regularization. This comparison may not be entirely fair in general, as static scaling for activity [119] and parameter [104][105] regularization was used. This scaling, e.g., does not consider the sensitivity variation between the parametric images, potentially resulting in differing resolution. Even though simultaneous regularization likely would benefit from optimally chosen scaling as well, it is possible that the gap to

activity-only or parameter-only regularization becomes smaller, motivating further study of scaling methods or the exhaustive exploration of the configuration space.

Voxelwise estimation of nonlinear parameters in the used 2TC model remains challenging. Issues with ill-posedness are well known, and they cannot be mitigated completely even as additional regularization is applied. Approaches that reduce the parameter set should be considered in addition [103].

Bowsher-weighted regularization was able to recover anatomical detail, both in the simulation study and for the clinical data, even below scanner resolution. Compared to joint entropy regularization (e.g., [132]), Bowsher-weighted regularization operates locally. This is an advantage, when there is no unique relation to the gray values in the MR image, as was the case, e.g., in the tumor region of the clinical study. Possible alternatives to the anatomical weight defined in (4.4) would be to modify the algorithm (4.13) by redefining the weight ω_{jk} to $(\omega_{jk}+\omega_{jk})/2$ and to use the original weight [33] or the Bowsher prior [35] (with $\omega_{jk} = 0$ if pixel j is not defined as a neighbor of pixel k). This, together with the impact of our modification, should be further evaluated.

Combined PET/MR scanners improve registration and alignment of the two modalities, and approaches for motion correction exist [177]. Inter-frame motion was not significant for the patient data in this study. In general, though, given long scan times, this should be addressed, e.g., by incorporating frame-wise image realignment prior to the fitting step.

A drawback of additional regularization in our approach is the larger configuration space $(\beta, \gamma, \sigma_p)$. The static scaling for σ_p (Sec. 4.3.4, [104]) made our approach more practical. Still, finding a good parameter configuration for the clinical data was challenging, as conditions differed from the simulation study, e.g., in terms of administered radiotracer, resolution, 2D/3D neighborhood, and lack of ground truth. In clinical routine, images for a range of configurations should be made available.

The optimization transfer principle together with the reformulation of Wang *et al.* [187], that allows breaking up the algorithm in three separate steps, provided a powerful and flexible algorithmic infrastructure that made nonlinear models feasible in direct reconstruction. We could show that it can be extended to simultaneous, anatomically-weighted regularization. The selected ALGLIB optimizer was suitable for the given problem and handled boundary conditions (mainly non-negativity) well.

Using C++ and analytical TAC modeling yielded an efficient implementation. The Feng model was a good match for the image-derived input function in the clinical study. Regularized images can be efficiently pre-calculated at the beginning of each iteration, and the Bowsher weighting did not add significantly to runtime. Separable optimization lends itself for straightforward voxelwise parallelization. Consequently, we were able to perform 5

iterations of the nonlinear fitting algorithm on 5500 voxels in the phantom study in only .3 seconds on a standard dual-core laptop. Including MLEM reconstruction, 200 algorithm iterations took approx. 200s.

Future studies will involve tumor biopsy of patients with surgery. This will allow correlation of voxelwise parametric images with tumor grade and different MR images.

4.7 Conclusion

We have presented a direct reconstruction algorithm for combining anatomical information with regularization on activity and kinetic parametric images. We have shown that the optimization transfer principle can be applied to a Bowsher-style anatomical weight to operate on a broad set of penalty functions. Our evaluation on simulated data has investigated tradeoffs for a subset of combinations of such regularization. It indicates an advantage for both simulated and clinical data when anatomical information is included and applied simultaneously to the activity and the parametric images. Especially, we have shown high-quality voxelwise nonlinear parametric images obtained from a clinical PET/MR scanner. The method is applicable to nonlinear compartment models, and using an analytic form for the input function allows for an efficient implementation.

Chapter 5

Development of a Reconstruction Framework for the Siemens Biograph mMR PET/MR Scanner

A C++-based framework was developed to efficiently prototype and evaluate algorithms for the Siemens Biograph mMR scanner. It covers all steps from data import or generation, algorithm implementation, image synthesis, and analysis. It was applied extensively, e.g., to direct reconstruction and anatomically-driven PET/MR reconstruction.

5.1 Requirements

Rapid prototyping of reconstruction and image-enhancing algorithms for a newly-introduced PET/MR scanner such as the Biograph mMR requires a complex and extensible software infrastructure. We focus on specifically enhancing PET images. Key requirements therefore are

- Allow reconstruction of PET data produced by the Biograph mMR scanner. This requires, e.g., a system matrix mapping sinogram to object space, data input/output (IO) for files produced by the scanner, and incorporation of normalization and attenuation.
- Allow for both 3D and 4D data sets and various measurement protocols.
- Efficient enough to run real-world data sets on workstations and small clusters without requiring specialized computing resources.

- Featured to support PET reconstruction, e.g., support input function modeling and decay.
- Allow efficient generation of artificial data sets, e.g., based on the Shepp-Logan phantom [157] or other anatomical data.
- Allow prototyping of iterative reconstruction algorithms and image enhancement techniques such as nested and direct algorithms, anatomical priors, and kinetic modeling, and combinations thereof.
- Allow comprehensive analysis of algorithms in terms of accuracy and performance.

The software developed and delivered by Siemens for the Biograph mMR is closed source and not easily re-usable or extendable for experimentation. Since PET/MR was a comparably new technology when this worked was initiated (2010), no existing framework was able to cover all requirements.

- PET-specific frameworks such as *STIR* [172] lack support for the Biograph mMR scanner and the MR facet. Other PET-only frameworks focus, e.g., on arbitrary scanner geometries [122].
- MATLAB-based approaches are often not efficient enough or require complicated multi-language development of algorithm parts in C/C++. Also object orientation and other facilities found in today's general purpose programming languages are not as mature as in other languages, making the development of a large-scale software framework more tedious. Examples include the *Image Reconstruction Toolbox for MATLAB (and Freemat)* by Fessler [73].
- More recently, dedicated PET/MR frameworks have been proposed. For example, the *CCP-PETMR* [14] project likely addresses many of the requirements, however, it is a very recent effort and scoped for the years 2015 – 2020. Other more recent efforts include the *SIMULTANEOUS PET/MR* project [16].

Therefore, a C++-based development framework called *reconlib* was developed, focusing on PET reconstruction and the incorporation of MR images generated by the Siemens mMR scanner. Its features, architecture, and implementation are explained and examples are given in the following.

5.2 Framework Overview

5.2.1 Key features

The framework enables efficiently working with scanner data and is specifically featured to support dynamic PET imaging. For experimentation, phantom data can be generated and results quantitatively analyzed. The reconstruction process is easy to use and extendable. Algorithm prototyping is facilitated by a plug-in approach for algorithms, a prior framework, and kinetic modeling infrastructure. In greater detail:

- **Input/Output.** The framework allows for reading both the mMR's sinogram and list mode data. In addition, Fourier rebinning can be performed on 3D sinogram datasets. MR images, normalization, and attenuation files are also supported. Exported data is usually in *.hdr* format with a small header describing the raw data blob, which can be visualized, e.g., in the AMIDE viewer [118]. IO of ITK [199] formats is supported an can be converted to the frameworks proprietary CVolume instances.

- **Scanner and PET specific.** A row-compressed 2D system matrix that exploits symmetries supports projection from the mMR's sinogram space to image space and back. Normalization and attenuation is processed directly from the mMR's output files into a normalization volume. Scatter correction is implemented using the Siddon algorithm [158]. All functions support array of volumes to handle 4D PET data, and a measurement protocol abstraction encapsulates frame durations and decay. Tracer input functions can be modeled and fitted.

- **Phantom generation.** An extendable phantom class allows to specify dynamic TACs, manages associated MR images, adds blur and noise as needed, and can generate sinograms given a projection matrix. Implementations include the Shepp-Logan phantom [157], a region-based phantom that can read arbitrary segmented volumes from file and associate TACs, and a phantom geared for misalignment studies capable of handling and interleaving several MR images based on the BRATS database [125].

- **Analysis.** A *region-of-interest (ROI)* toolset allows definition of various geometric shapes and, e.g., phantom regions. ROIs can be visualized and defined in AMIDE. The main analysis class allows to keep track of single values, functions (such as TACs), vectors, or volumes and ROIs over the time of algorithm execution and compares to a true value (if given). It integrates with gnuplot for visualization at runtime. An analysis database is provided that can process multiple noise realizations and derive, e.g., bias and variance.

- **Reconstruction.** The reconstruction class simplifies the task of preparing all data and invoking an actual reconstruction algorithm. It is configured with a settings object that encapsulates all parameters (such as file names, number of iterations, etc.) as needed. Several iterative reconstruction algorithms are provided, including MLEM/OSEM, OSL, and direct parametric reconstruction algorithms for kinetic modeling. Filtering such as to correct for positron range can be added as needed.

- **Generic Prior framework.** A highly versatile prior infrastructure is provided built around a prior base class. It comprises a set of potentials, distance measures, and voxel neighborhoods, that can be extended to implement more complex schemes. Examples include MAP reconstruction algorithms using, e.g., Bowsher [35], Huber, and non-local priors [38]. Debugging facilities can visualize the prior for a selected set of voxels.

- **Kinetic Modeling.** A kinetic model is fitted using a fitting (or optimization) algorithm. Kinetic models include spectral basis functions and non-linear 1/2/3 tissue compartment models along with means to compute the convolution with the input function as well as the gradient. Optimization algorithms can be voxel based or operate on complete volumes. A versatile third party math library (ALGLIB [32]) is integrated for a selection of 1D fitting algorithms used for voxel-based fitting.

- **Infrastructure.** A custom small-scale math library includes vectors and matrices (i.e., volumes) and operator overloading. A powerful function abstraction for N-to-M valued mappings is used to implement, e.g., sampled, interpolated, analytical and kinetic model functions and to provide operations for these functions. A randomization infrastructure allows for repeatable experiments and evaluation of different noise realizations. Scripting automation is provided to export to AMIDE, run multiple realizations in batch, and iteratively optimize parameters.

5.2.2 Architecture

Since the framework comprises a significant development effort, it is key to follow well-established software engineering principles. Specifically, the components of the framework must be scalable and re-usable to new use cases efficiently and must not restrict usage. For example, an iterative reconstruction algorithm implementation may need to be combined with kinetic modeling and anatomical constraints. From a user perspective, such a framework also allows for efficient rapid prototyping of algorithms.

- **Object orientation.** Based on the principle of information hiding, inheritance, and well-defined external APIs, this approach generally allows better scaling and reuse [100]. All components of the framework are implemented this way.

- **Generic programming.** Templates in C++ allow decoupling of algorithm or data type implementation from a specific underlying type. This reduces the amount of code to be written and encourages re-use [20]. Especially data structures such as volumes and optimization algorithms are implemented using templates, but also reconstruction algorithms and, e.g., anatomical constraints made extensive use of it.

- **Separation of concerns.** Related to the Single Responsibility Principle, no functionality should be duplicated in the framework. In addition, different aspects must not be mixed. This avoids errors and enforces a better and more scalable design of APIs [95]. For example, the framework clearly separates the aspects of IO, reconstruction, optimization, and analysis.

- **Low coupling / high cohesion.** Classes are designed to combine closely related concepts but to make as few assumptions about their usage to the outside [31]. For example the optimization classes encapsulate external libraries, data type translation, and configuration and are used both during iterative reconstruction as well as post-reconstruction fit.

- **Design patterns.** Well-established design patterns allow for better code that is easier to understand by third parties [81]. For example, the reconstruction is configured via a *command*, uses a *strategy* to incorporate the actual reconstruction algorithm, which in turn implements *template methods*. *Adapter* classes are used to incorporate external imaging (ITK) and optimization libraries (ALGLIB).

Examples for class hierarchies are given in the following. The penalized likelihood fitting algorithm (Fig. 5.1) used in the MAP direct reconstruction algorithm of Chapter 4 extends the base *Levenberg-Marquardt (LM)* fitting algorithm and can be customized with a target function given as a template parameter. The LM algorithm in turn derives from a basic *FittingAlgorithm* class that allows weights on the input in addition. The algorithm is furthermore *Cloneable*, as needed for parallelization. The penalized likelihood fitting algorithm is used by the *VolumeFitting1D* class (Fig. 5.2) that fits an entire volume by delegating each voxel to a *FittingAlgorithm* and that is a specialization of *BasisVolumeFitting*. *BasisVolumeFitting* also manages the basis functions used during the fitting. Another example is given in Figure 5.3 for the function abstraction and the kinetic models implemented in the framework in Figure 5.3.

An experiment is defined in the *main* function and comprises all steps needed to load data and configure the reconstruction. Main functions can differ in the way data is imported (clinical vs. phantom) and what algorithms are used together. Different main functions were implemented for, e.g., standalone reconstruction and post-fitting, direct dynamic reconstruction, reconstruction with positron range correction, and anatomically constraint

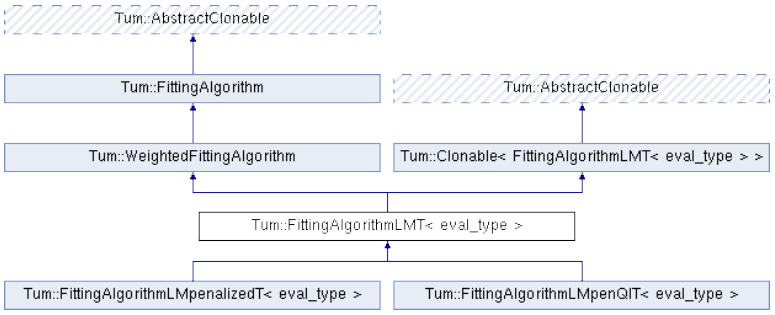

Figure 5.1: Class hierarchy for the LM-based penalized likelihood fitting algorithm used in the MAP direct reconstruction framework.

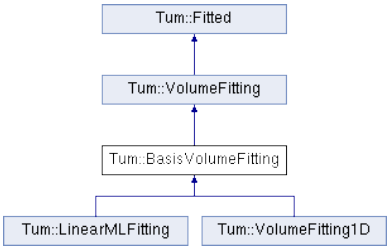

Figure 5.2: Class hierarchy for *FittingAlgorithm1D*.

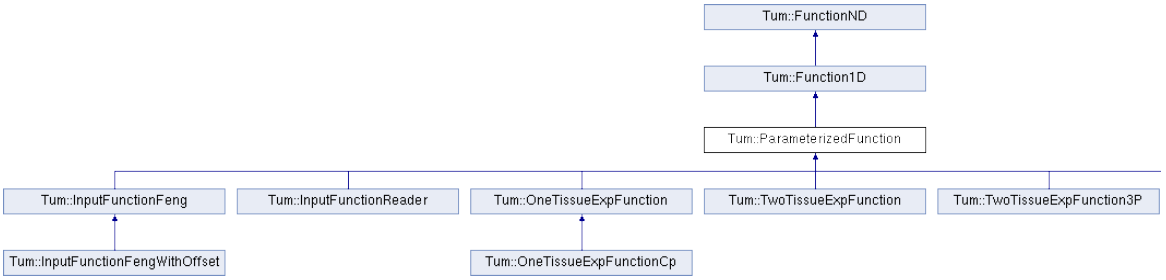

Figure 5.3: Class hierarchy for kinetic models, which are based on *ParameterizedFunction*.

reconstruction. One variant of these main functions repeats part of the reconstruction process iteratively to optimize parameters in a given range, e.g., for lowest error. A high-level view of the main function for direct dynamic reconstruction is given as an example in Listing 5.1.

5.2.3 Implementation Details

Flexibility was achieved by composing and customizing components as needed, reusing existing parts and prototyping new parts. For example, the generic prior framework is based on the *GenericPrior* class that is customized with components for *Weight*, *PotentialDerivate*, and *Neighborhood*. Customization is done by template parameters to avoid virtual function call overhead, e.g., Listing 5.2 defines a $5 \times 5 \times 5$ Bowsher prior for the mMR scanner. Since the selection of neighboring voxels in this case is constant throughout the execution of the reconstruction algorithm, they can be buffered for each voxel. *GenericPrior* accepts

```
parsing of command line parameters if applicable
setting up of recon settings such as input/output filenames and parameters
setting up of MR volumes
setting up of measurement protocol
generation of system matrix (parameters)
setting up of analysis object and ROI definition
setting up of priors (MR volumes)
setting up of iteration counts and related reconstruction parameters
generation of input function and set of basis functions (measurement protocol)
generation of inner reconstruction algorithm, e.g., OSEM (parameters, priors)
setting up of fitting, including fitting algorithm, coefficients,
        parameters, and initial values
generation of outer, nested reconstruction algorithm (inner algorithm, fitting)
generation of reconstruction object(recon settings, system matrix,
        outer recon algorithm)
invocation of reconstruct function
exporting of reconstructed image sequence and other data such as parametric images
```

Listing 5.1: Overview of steps involved in the direct dynamic reconstruction experiment's main function. Arguments for generation steps are given in brackets.

pre-constructed objects for each component or will construct a default object with empty constructor argument list otherwise. In the previous example, the *BowsherNeighborhood* requires an MR image to be set and is therefore pre-constructed, whereas the weight is stateless and can be constructed from a default constructor.

In addition to flexibility, performance is a key aspect. Exploitation of parallelism has great potential even on regular PC hardware. In the direct reconstruction problem, parallelism occurs most notably

- in the projection of the system matrix.
- in the independent reconstruction of a series of PET frames
- in the independent fitting of a single voxel over a series of PET frames

The Microsoft PPL library was used to exploit loop-level parallelism (*parallel_for_fixed*). This generally requires temporary data structure inside the loop to be duplicated for each thread context. PPL provides a *combinable* data type that provides a thread-local copy as needed and allows to accumulate results from multiple threads. Such a thread-local copy is especially needed for the prior and the fitting objects during parallelized reconstruction.

```
typedef GenericPrior< BufferingNeighborhood< BowsherNeighborhoodNxNxN<5> >,
                      DistanceWeightMMR3D,
                      PotentialDerivative_Quadratic>
BufferedBowsherPriorMMR3D;
```

Listing 5.2: Definition of 3D buffered Bowsher prior for the mMR geometry.

The reconstruction algorithm typically only has a pointer to the base class of these objects and does not know their precise type, and the copy constructor cannot be virtual in C++. Therefore, a *Cloneable* infrastructure was established that invokes the copy constructor of a derived class from within a virtual clone method. The infrastructure and its use are shown in Listing 5.3.

```
struct AbstractClonable
{
  virtual ~AbstractClonable() {}
  virtual AbstractClonable* clone() const = 0;
};

template <class C>
struct Clonable : public virtual AbstractClonable {
  virtual AbstractClonable* clone() const {
    return new C( dynamic_cast<const C&>(*this) );
  }
};
...
// declaration using lambda syntax
Concurrency::combinable<Prior*> priors(
  [&]{return dynamic_cast<Prior*>(this->_prior->clone());}
)
...
// use of thread local copy within parallel loop
Concurrency::samples::parallel_for_fixed< int>(start, end, 1, [&]( int f) {
  Prior* prior = priors.local();
...
```

Listing 5.3: *Cloneable* infrastructure, and example of how *Cloneable* is used to generate a thread-local copy with PPL's *combinable* of a Prior class implementing *Cloneable*.

5.3 Examples and Results

Framework results are given in Subsection 5.3.1, including complexity and runtime performance. The framework was used to prototype and evaluate a large set of PET-related algorithms from literature, including direct parametric reconstruction using spectral basis functions [147], nested reconstruction [124], simultaneous estimation of parametric images and input function [146], edge-preserving [86][83][127] and anatomical [35][33] priors. We present original work on direct reconstruction (Sec. 5.3.2) and non-local anatomical regularization (Sec. 5.3.3).

5.3.1 Framework Results

The framework was implemented in C++ using Microsoft Visual Studio Express 2012. The code was also successfully ported and run on a Linux server workstation. The framework comprises approximately 28000 lines of C++ code in 100 framework files and 6000 lines of C++ code in 20 experimentation main files. External libraries include the ALGLIB math

library, Microsoft *parallel processing library (PPL)*, a gnuplot iostream integration, and a small part of ITK.

Performance characteristics are presented in Table 5.1. The experiments were run on a Windows 7 laptop with 16 GB RAM and an Intel i5-2430M quad-core processor running at 2.2 GHz. Basic OSEM reconstruction of 18 frames took 117 s. Parallelization of the system matrix projection calculation improved performance by only 23 %, likely because other parts of the reconstruction still were single threaded. Fully parallelizing independent frame reconstruction onto the 4 threads improved performance by 54 % which seems adequate given that the laptop was executing normal operating system tasks in the background. Obviously, this optimization is only available for multi-frame dynamic PET series. Combining the two methods did not enhance performance further. Adding a Bowsher prior which selects 10 anatomically similar pixels from a $3 \times 3 \times 3$ neighborhood for additional regularization increased runtime to 590 s. However, applying again frame parallelism (which included the prior calculation) improved performance again by 54 %. Buffering the selection of the neighboring voxels improved performance even by 80 %, making the anatomical reconstruction only 2X slower than the basic reconstruction. Kinetic modeling in general is very complex. However, for a spectral model, calculation can be fairly efficient, e.g., using a *non-negative least squares (NNLS)* algorithm. With both reconstruction and the 1D independent voxel fitting parallelized, generation of the kinetic parameter images took only 238 s (vs. 552 s single threaded).

Algorithm setup	Runtime
OSEM	117 s
OSEM (parallel system matrix)	90 s
OSEM (parallel frames)	**54 s**
OSEM (parallel frames + system matrix)	67 s
OSEM/Bowsher-10	590 s
OSEM/Bowsher-10 (parallel frames)	270 s
OSEM/Bowsher-10 (parallel frames, buffered)	**120 s**
OSEM/Kinetic modeling spectral/NNLS	552 s
OSEM/Kinetic modeling spectral/NNLS (parallel frames + fit)	**238 s**

Table 5.1: Performance results for various reconstruction algorithms on an Intel i5-2430M quad-core laptop using Microsoft Visual Studio Express 2012. A dynamic series of 18 mMR sinograms was reconstructed to 18 partial $172 \times 172 \times 10$ volumes. The OSEM algorithm was used with 21 subsets for a total of 63 subset iterations.

5.3.2 Dynamic reconstruction using spectral basis functions

Dynamic (4D) imaging is a prerequisite for extraction of biological kinetic parameters from PET, e.g., for improved diagnosis of brain glioma patients. However, conventional dynamic PET based on independent frame reconstruction suffers from noisy images, especially when a high temporal resolution is needed. We investigated dynamic image reconstruction using the

spectral analysis model [147] for [^{18}F]FET imaging in patients with brain glioma acquired with the Biograph mMR PET/MR system using the reconlib framework in the following.

A 40 min dynamic [^{18}F]FET scan (126 MBq) of a patient with a glioblastoma in the frontal lobe was acquired with the Biograph mMR. List mode data were histogrammed into 21 frames (1×5 s, 9×10 s, 3×30 s, 1×2 min, 7×5 min). Data were dynamically reconstructed from sinograms using a reconstruction software developed in-house for the Biograph mMR. Single-slice rebinning and 3 OSEM iterations (21 subsets) were used for all reconstructions. ROIs were defined as shown in Figure 5.4.

Given a dynamic sequence $\{y_m, m = 1, \ldots, M\}$ of sinograms for each time frame m, a geometric system matrix $A = (a_{ij})$, and a set of basis functions $b_k(t), k = 1, \ldots, K$ the dynamic time activity is modeled as

$$x_m(\theta_j) = \sum_{k=1}^{K} b_{mk}\theta_{jk}$$

with the coefficients θ_{jk} to be estimated, and b_{mk} denoting the average value of the kth temporal basis function $b_k(t)$ in time frame m and θ_{jk} the coefficient of the kth basis function for the jth voxel. Application of the MLEM algorithm leads to the following update equation

$$\theta_{jk}^{n+1} = \frac{\theta_{jk}^{n}}{\sum_i a_{ij} \sum_m b_{mk}} \sum_m b_{mk} \sum_i a_{ij} \frac{y_{im}}{\eta_{im} + \sum_j a_{ij} \sum_k b_{mk}\theta_{jk}^{n}}.$$

The spectral analysis model [56] uses a set of exponential functions that are convolved with the AIF $C_p(t)$:

$$b_k(t) = \exp(-\beta_k t) \otimes C_p(t)$$

with rate constants β_k of the kth spectrum. For reconstruction a set of 50 spectral basis functions was used where β_k was logarithmically-spaced between $\left[\lambda\ s^{-1}, 0.1\ s^{-1}\right]$, with λ being the decay constant for ^{18}F. An additional blood volume term was added to the basis functions.

The direct reconstruction algorithm was implemented with a cascaded ReconAlgorithm. The outer one iterating between an actual reconstruction step and the fitting to a spectral model. The reconstruction algorithm was implemented using OSEM subsets and included correction for random events. The run-time analysis capabilities of the framework are shown in Figure 5.5 for TAC analysis.

Parametric images of K_1 were calculated and compared with post-reconstruction spectral analysis fitting using NNLS, as shown in Figure 5.6. The direct reconstruction exhibited greatly reduced standard deviation at comparable bias.

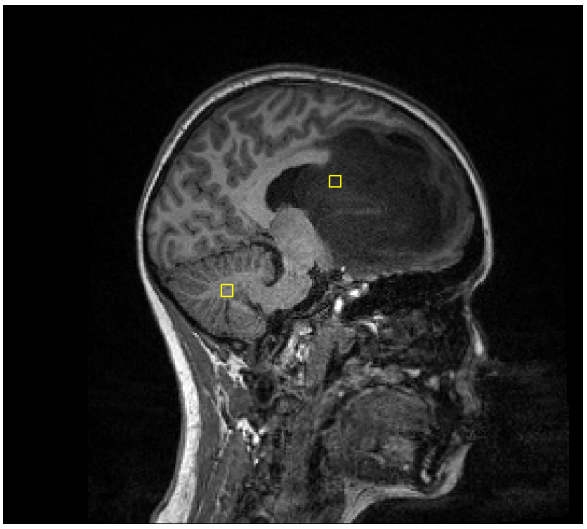

Figure 5.4: ROI definition for the experiment, automatically visualized over the MR image in AMIDE.

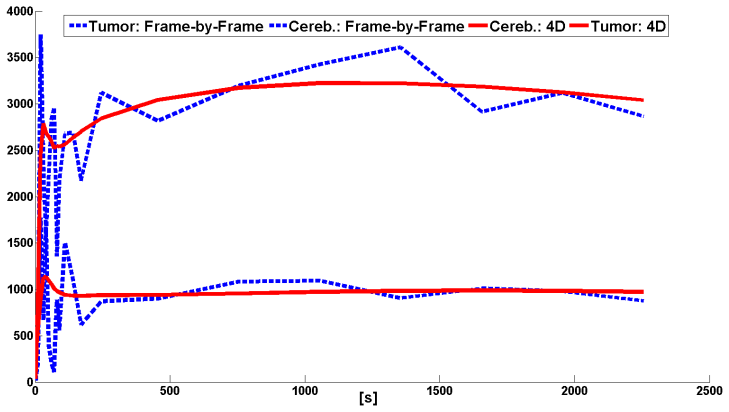

Figure 5.5: At-runtime analysis of corresponding TACs using gnuplot.

5.3.3 Non-local anatomical regularization and anatomical mismatch

MR-based priors leveraging high-quality multi-modal image data from an integrated scanner such as the Biograph mMR are promising, and a number of approaches exist (cf. Section 2.4.5). However, a problem arises from mismatch between PET and MR information. Conventional MR-based priors rely on the assumption that a homogeneous MR uptake corresponds to a homogeneous uptake in the PET image, which is mostly the case for FDG brain imaging. Brain tumors, however, are very heterogeneous and the benefit of MR-based priors must be evaluated carefully. Existing approaches include edge blurring [54] and non-local filtering [38], which can be combined with anatomical information to address mismatch [129]. A problem with the non-local filter from [38] is that it is not invariant under rotation, which can lead to distortions around edges and edge artifacts. Also, it is computationally

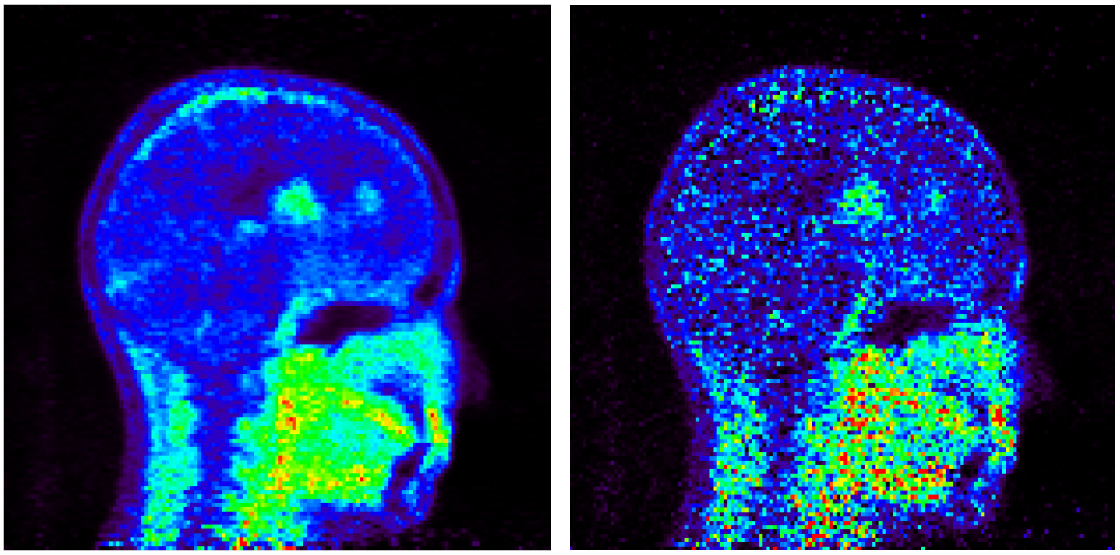

(a) Direct (b) Post

Figure 5.6: K_1 parametric image obtained from direct reconstruction (a) and post-reconstruction fitting (b) using the spectral analysis model.

expensive, because a patch around each voxel in the search window needs to be compared to the patch around the center pixel. Patch computation is sketched in Figure 5.7.

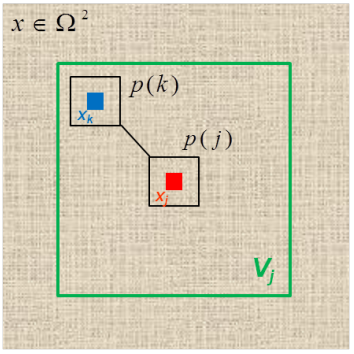

Figure 5.7: Non-local filtering determines weight ω_{jk} by calculating a measure based on voxels in patches p for each voxel k in a search window V around voxel j.

We have prototyped a novel weight measure based on rotation-invariant Zernike moments [96]. The Zernike polynomials form a complete orthogonal set over the interior of the unit ball. They are defined in polar coordinates with azimuthal angle θ and radial distance ρ. The Zernike polynomial of order n and repetition m where n and m are non-negative integers fulfilling the condition $n \geq 0$, $n - |m|$ is even, and $|m| < n$ are defined by

$$Z_n^m(\rho, \theta) = R_n^m(\rho) \exp(im\theta)$$

where the radial polynomial R_n^m is calculated by

$$R_n^m(\rho) = \sum_{s=0}^{\frac{n-|m|}{2}} \frac{(-1)^s (n-s)!}{s!(\frac{n+|m|}{2}-s)!(\frac{n-|m|}{2}-s)!} \rho^{n-2s}.$$

The Zernike moments for a continuous image function f are defined as the projection of the image function onto the orthogonal set of Zernike polynomials:

$$A_n^m = \frac{n+1}{\pi} \int_0^{2\pi} \int_0^1 f(\rho,\theta) Z_n^{m*}(\rho,\theta) \rho d\rho d\theta \tag{5.1}$$

where $*$ denotes the complex conjugate. The discrete form of (5.1) for an $N \times N$ image is obtained by replacing the integrals by summations leading to

$$A_n^m = \frac{n+1}{\pi} \sum_{x=0}^{N-1} \sum_{y=0}^{N-1} f(x,y) Z_n^{m*}(x,y)$$

where $x^2 + y^2 \leq 1$. To compute the Zernike moments, the image needs to be mapped into polar co-ordinates and onto the unit circle with center $(\bar{x}, \bar{y})$ using

$$\rho = \sqrt{(x-\bar{x})^2 + (y-\bar{y})^2 / d}, \quad \theta = \tan^{-1}\left[\frac{x-\bar{x}}{y-\bar{y}}\right]$$

where the distance d is computed by

$$d = \sqrt{(x_2 - \bar{x})^2 \frac{1}{2} + (y_2 - \bar{y})^2 \frac{1}{2}}.$$

We define a new nonlocal weight that is based on Zernike moments for image patches that includes the following steps:

(1) Determine the order n of Zernike moments, e.g., 3

(2) Determine patch size N, e.g., 5×5, and search window size, e.g., 11×11

(3) For each patch centered around a voxel x_k inside the search window V_j being centered around the current voxel x_j

   (a) the vector of magnitudes of Zernike moments is computed by

$$v_k = \left(|A_0^0|, |A_1^1|, |A_2^0|, |A_2^2|, |A_3^1|, |A_3^3|\right)$$

   (b) the similarity of v_k to the vector of magnitudes v_j is determined by

$$\|v_j - v_k\|_2^2$$

(c) the Zernike based prior weight for the neighboring voxels x_k and x_j is calculated as

$$\omega_{Z,jk} = \exp\left(-\frac{\|v_j - v_k\|_2^2}{h^2}\right)/d_{jk}$$

The weight $\omega_{Z,jk}$ is input to the nonlocal regularization function that is defined by

$$R_{\text{Zernike}}(x) = \sum_{j=1}^{J}\sum_{k\in V_j}\omega_{Z,jk}\psi(x_j - x_k).$$

The regularization function $R_{\text{Zernike}}(x)$ is then incorporated into our MAP framework (see 2.8), resulting in the $\text{Z}_{N,n}$ **algorithm**, where the n-th order Zernike moments are calculated over $N \times N$-sized patches.

Closely related to the Bowsher approach, anatomical guidance can be incorporated via a thresholded selection of the neighborhood voxels N_{Thresh}. Only voxels in a N-by-N search window that are similar in intensity within p in the MR image μ are considered, giving rise to the regularization function $R_{\text{ThresholdedBowsher}}(x)$ with a simple distance measure ω_{jk}. This regularization results in the $\text{TB}_{N,p}$ **algorithm**:

$$N_{\text{Thresh}}(j,\mu,\tau,V) := \left\{k \in k_1, k_2, \ldots : \tau < \frac{\mu_j}{\mu_k} < \frac{1}{\tau}, \tau = 1 + p\right\},$$

$$R_{\text{ThresholdedBowsher}}(x) = \sum_{j=1}^{J}\sum_{k\in N_{\text{Thresh}}}\omega_{jk}\psi(x_j - x_k).$$

Finally, we combine the anatomical thresholding with the Zernike-based weighting function in the $\text{TB}_{N,p} + \text{Z}_{N,n}$ **algorithm** using the regularization function

$$R_{\text{TB+Z}}(x) = \sum_{j=1}^{J}\sum_{k\in N_{\text{Thresh}}}\omega_{Z,jk}\psi(x_j - x_k).$$

We have prototyped these three algorithms in the framework, leveraging the prior infrastructure and an existing implementation of the anatomical neighborhood selection. For reference, a conventional variant was also added based on non-local patches [38] of size N, which we refer to as the PS_N **algorithm**. All algorithms are summarized in Table 5.2.

In a first simulation study an artificial mismatch phantom was generated in the framework as shown in Figure 5.8. The conventional anatomical approach (TB) performed well on matched tumors, but failed to address mismatch completely. The combined TB+Z method outperformed the two conventional methods both in *Peak-Signal-to-Noise-Ratio (PSNR)* over the whole image as well as in *Mean Squared Error (MSE)* in the lesions.

Algorithm	Description
$Z_{N,n}$	non-local, uses n-th order Zernike moments with patch size $N \times N$
$TB_{N,p}$	anatomical, incorporates p-similar MR information in an $N \times N$ window
$TB_{N,p} + Z_{N,n}$	combines anatomical and non-local methods
PS_N	non-local, uses conventional $N \times N$ patches

Table 5.2: Overview of prototyped algorithms.

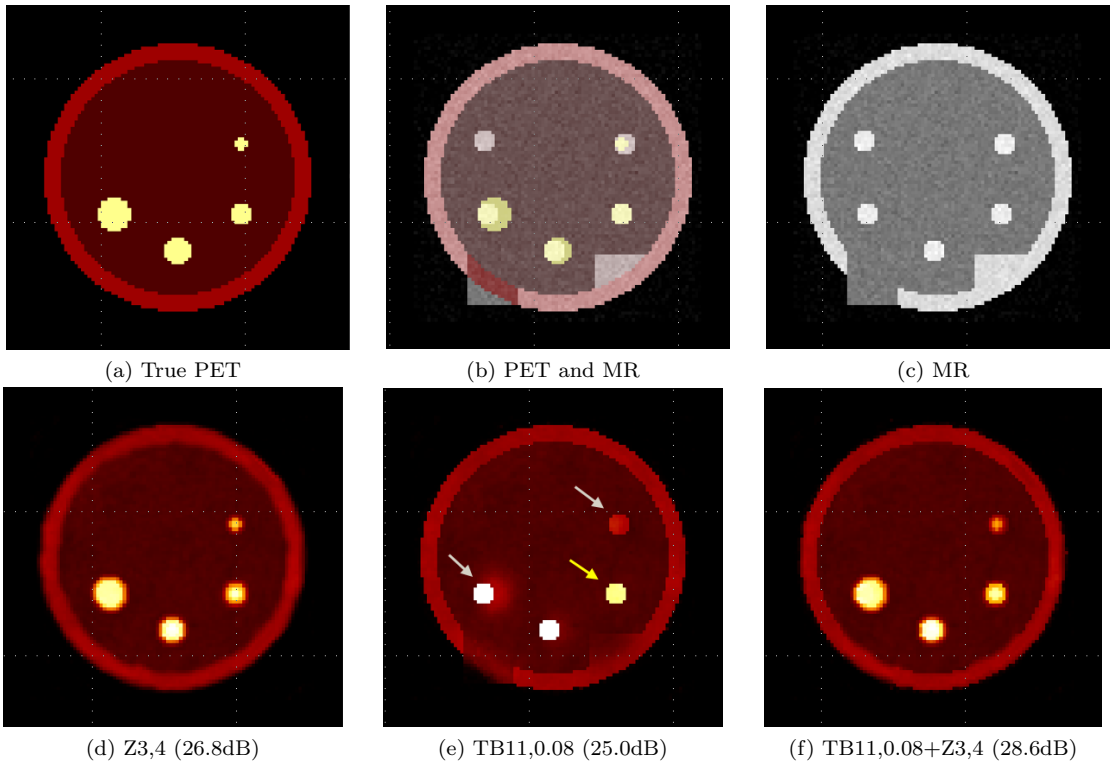

(a) True PET (b) PET and MR (c) MR

(d) Z3,4 (26.8dB) (e) TB11,0.08 (25.0dB) (f) TB11,0.08+Z3,4 (28.6dB)

Figure 5.8: Comparing conventional approaches (d),(e) to the combined non-local filtering anatomical approach (f) for an artificial mismatch phantom (a)–(c). The combined method showed best PSNR (given in brackets below the images), PSNRs for matched/unmatched tumor ROIs only are 45.0 dB/41.8 dB (d), 248 dB/0.1 dB (e), and 54.0 dB/23.0 dB (f). This means that the combined method did not quite match the performance of the non-anatomical approach in mismatch and the anatomical approach in match but performed best overall.

A set of more realistic phantoms was generated from the Multimodal Brain Tumor Image Segmentation (BRATS) training dataset available from the MICCAI 2013 conference website [125], which provides histological labels in addition to simulated MR images for a comparatively large number of cases. Of particular interest were tumor areas that are non-enhancing in MR, effectively producing mismatch and missing delineation in the MR. One of the dynamic phantoms generated in the framework from labeled data with clinical TACs and the associated T1c MR image are shown in Figure 5.9. Compared to conventional MAP in Figure 5.10, the nonlocal approaches clearly revealed greater detail. The conventional patch-based approaches were prone to edge artifacts and the image was more edged overall.

The effect of adding anatomical information is shown in Figure 5.11. The large non-enhancing part of the tumor was only correctly delineated with the combined method, and the recovery coefficient over the complete tumor improved from 88.8 % to 96.5 % with the combined method. Smaller mismatched parts at the bottom of the tumor were better recovered than in the conventional method, but the artifact were still visible.

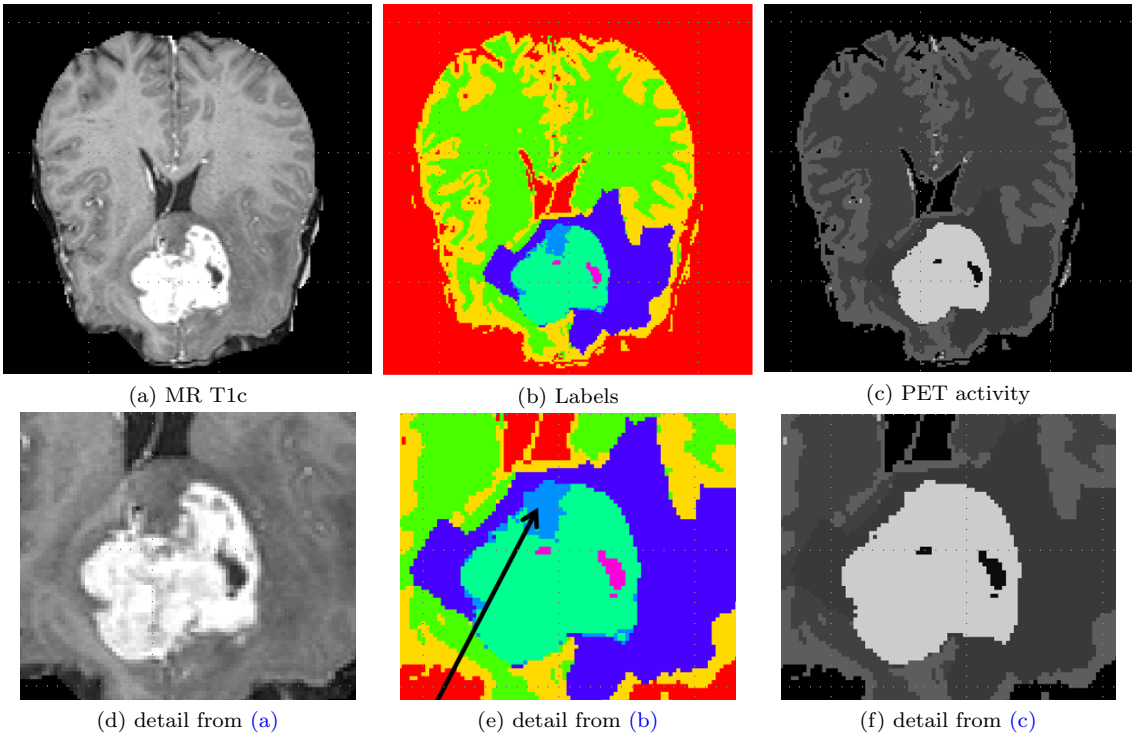

(a) MR T1c (b) Labels (c) PET activity

(d) detail from (a) (e) detail from (b) (f) detail from (c)

Figure 5.9: From the BRATS database, T1c MR image (a),(d), label image available from the database (b),(e), generated dynamic PET activity image (c),(f). The black arrow in (e) highlights the non-enhancing (MR) label which represents PET/MR mismatch.

Finally, we used clinical data from the mMR scanner as shown in Figure 5.12. Since the ground truth was not known, the approaches could only be compared visually. The anatomical methods improved the resolution of the image overall, but the conventional method (TB) failed to address mismatch in the tumor region, where activity extends beyond the boundaries found in the MR image (see marked regions in Figure 5.13). The combined method seemed to produce a more consistent image overall.

Zernike moments are more efficient to calculate, as shown in Table 5.3. Standard non-local filtering computes the distance between each voxel in each patch around each voxel in the search window for every center voxel in the picture. Zernike moments can be pre-calculated for each voxel in the picture, and the measure is calculated only on a small set of moments (e.g., 4-th order moments for $Z_{5,4}$ vs. 25 voxels in a 5×5 patch). We found the Zernike-based approach to be rotation invariant as opposed to the original non-local approach, as can be seen in Figure 5.14 that compares the filter weights. However, the advantage was more visually and did not manifest consistently in our quantitative analysis. This could be

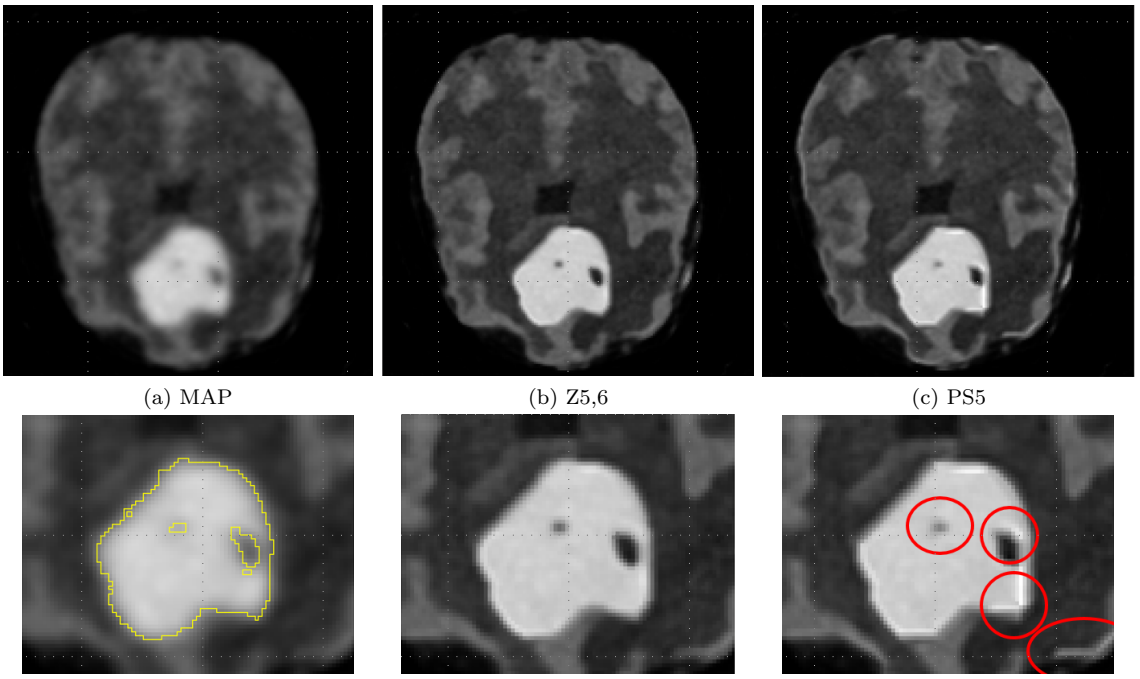

(a) MAP (b) Z5,6 (c) PS5

(d) detail from (a) (e) detail from (b) (f) detail from (c)

Figure 5.10: For the BRATS phantom, reconstruction using conventional MAP (a),(d), the Zernike-based nonlocal approach with a 5×5 patch size (b),(e), and the conventional nonlocal patch-based approach with a 5×5 patch size (c)(f). The latter was more prone to artifacts (red circles).

due to the homogeneous nature of the artificial mismatch phantom, where stronger filtering on fewer voxels may be beneficial. A limitation of the approach chosen to incorporate anatomical information is that it addresses the case of mismatch where a border is absent in the MR. However, it only insufficiently addresses the case where a false border is in the MR. This needs further investigation. We have found the BRATS database to be an excellent source of images for investigation of multimodal image mismatch.

Algorithm	Description	Runtime
$Z_{3,4}$	nonlocal Zernike, 3×3 patch	16 s
$Z_{5,6}$	nonlocal Zernike, 5×5 patch	22 s
TB_{11}	conventional anatomical	4 s
$TB_{11} + Z_{3,4}$	anatomical and non-local combined	12 s
PS_3	conventional nonlocal, 3×3 patch	22 s
PS_5	conventional nonlocal, 5×5 patch	57 s

Table 5.3: Performance results for various algorithms on an Intel i5-2430M laptop for the clinical dataset $172 \times 172 \times 1$ and a search window of 11×11.

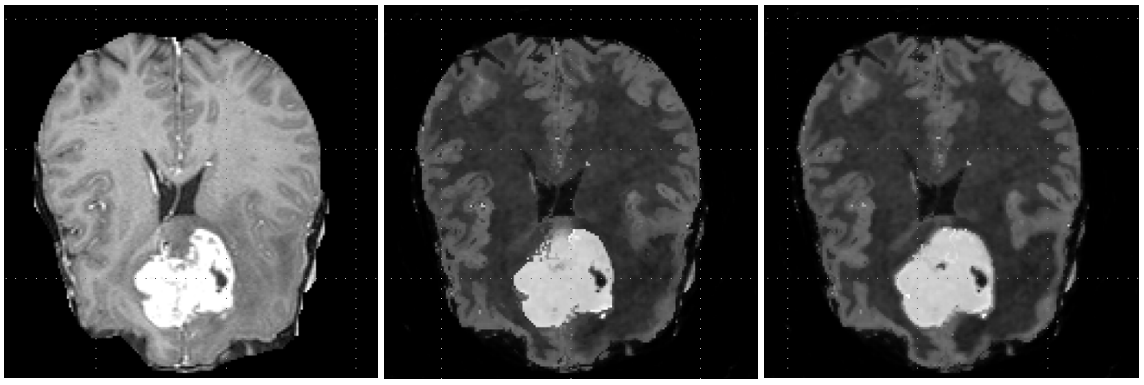

(a) MR T1c (b) TB11,0.08 (c) TB11,0.08+Z5,6

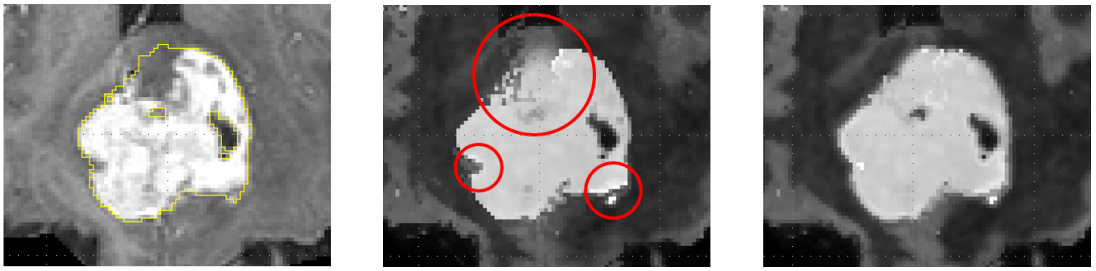

(d) detail from (a) (e) detail from (b) (f) detail from (c)

Figure 5.11: For the BRATS phantom, the MR image (a),(d) used by the conventional TB approach (b),(e) and the combined TB+Z approach (c),(f). The recovery coefficient for the non-enhancing ROIs (highlighted by red circles) was 88.8 % for the TB approach (b), but reached 96.5 % for the combined approach (c).

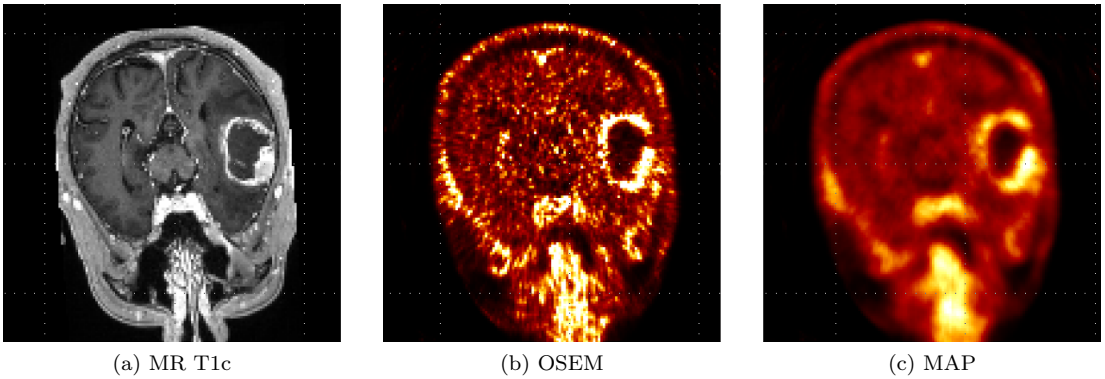

(a) MR T1c (b) OSEM (c) MAP

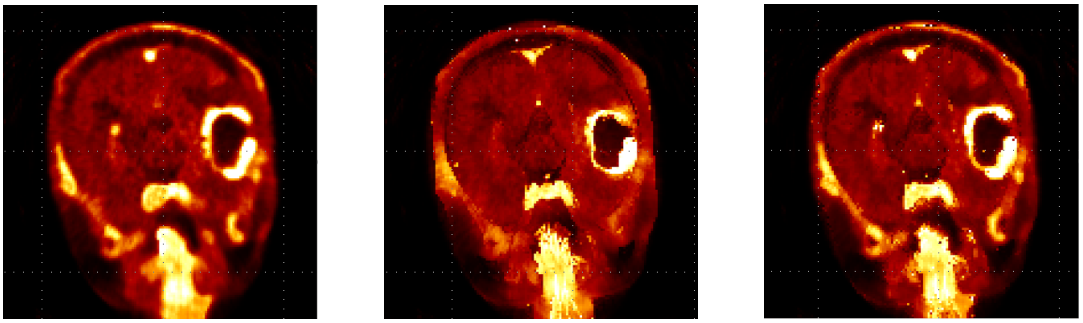

(d) Z5,6 (e) TB11,0.08 (f) TB11,0.08+Z5,6

Figure 5.12: Clinical data from the mMR scanner, T1c MR image (a) and reconstructed images (b)–(f).

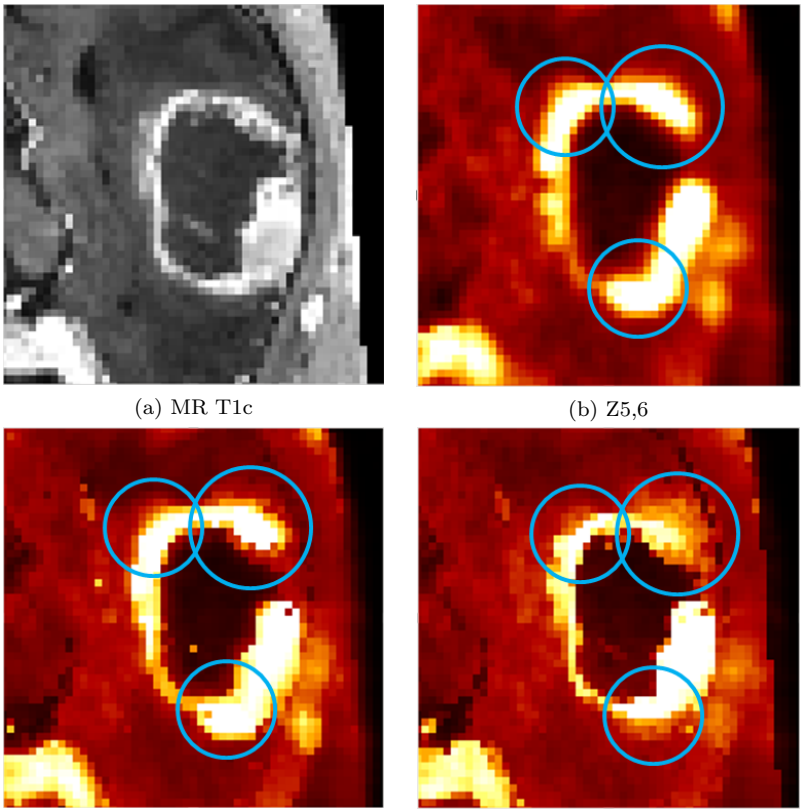

(a) MR T1c (b) Z5,6

(c) TB11,0.08+Z5,6 (d) TB11,0.08

Figure 5.13: Section detail of the tumor region from Figure 5.12.

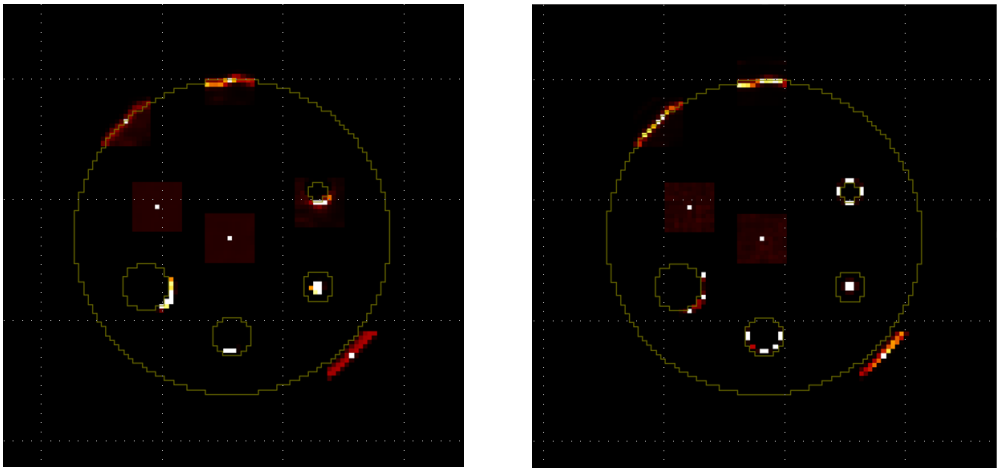

(a) Conventional patches (b) Rotation-invariant patches

Figure 5.14: Comparing the weights for 9 select voxels (shown white) generated by the conventional nonlocal approach (a) vs. the rotation-invariant Zernike-based approach (b).

5.4 Discussion

The *reconlib* framework comprises all facets required to prototype algorithms for the Biograph mMR scanner, resulting in a fairly complex framework comprising approximately 28000 lines of code. Its modular approach following well-established software engineering

techniques proved versatile enough to successfully prototype and evaluate a range of algorithms (e.g., incorporating anatomical knowledge into a nonlocal prior). Its implementation in C++ and the parallelization of compute-intense projections and multi-frame reconstruction allowed to quickly turnaround images during algorithm development or to run full scale clinical images in batch mode. It is well integrated into third-party tools and libraries such as AMIDE for visualization and ROI definition, gnuplot for at runtime analysis, or ITK for file IO, enabling a productive work flow. A challenge arose from the constant addition of new requirements during rapid prototyping of new algorithms, which could result in single-purpose code unless development is accompanied by careful code refactoring.

Chapter 6

Conclusion

The opportunities and challenges associated with modern integrated multimodal imaging devices necessitate novel tools, approaches, and algorithms. A first example was given as part of Chapter 1, where we could show that an inpainting approach applied to a truncated attenuation map can yield significantly better results and reduce artifacts [5, 8]. Throughout the thesis, we could show that new algorithms both can improve upon shortcomings associated with integrated devices and can generate a new class of images with unprecedented detail. Key to these results was the in-house developed reconstruction framework.

Researching these methods takes place in a complex environment spanning physics, biology, mathematics, and computer science. In Chapter 2 we have given a self-contained introduction and summarized related work on PET systems, data aquisition, image degrading effects, reconstruction algorithms, anatomically guided PET reconstruction, and dynamic PET reconstruction.

In Chapter 3 we have investigated positron range for high energy tracers such as ^{82}Rb and its effect on image quality in the new Siemens Biograph mMR hybrid PET/MR scanner using Monte Carlo simulation [3]. We found positron range to be tissue dependent and especially significant in the direction of the 3 T magnetic field. At inhomogeneous tissue borders, this degrades spatial resolution and can lead to misplacement artifacts. Our 3D-MLEM framework applying positron range diffusion kernels allows for a localized correction depending on underlying tissue. A potential for tissue-specific positron range correction was found for both homogeneous regions and at tissue borders. Especially, our anatomically generalized approach improved image quality for realistic phantoms [1].

In Chapter 4 we have presented a direct reconstruction algorithm for combining anatomical information with regularization on activity and kinetic parametric images. We have shown that the optimization transfer principle can be applied to a Bowsher-style anatomical weight

to operate on a broad set of penalty functions. Our evaluation on simulated data has investigated tradeoffs for a subset of combinations of such regularization. It indicates an advantage for both simulated and clinical data when anatomical information is included and applied simultaneously to the activity and the parametric images. Especially, we have shown high-quality voxelwise nonlinear parametric images obtained from a clinical PET/MR scanner. The method is applicable to nonlinear compartment models, and using an analytic form for the input function allowed for an efficient implementation [2].

In Chapter 5 we have presented our C++-based *reconlib* framework. It enables to efficiently prototype and evaluate algorithms for the Siemens Biograph mMR scanner. It covers all steps from data import or generation, algorithm implementation, image synthesis, and analysis. It was applied extensively, e.g., to direct reconstruction in Chapter 4 and anatomically-driven PET/MR reconstruction. This resulted in a fairly complex framework comprising approximately 28000 lines of code. Its implementation in C++ and the parallelization of compute-intense projections and multi-frame reconstruction allowed to quickly turnaround images during algorithm development or to run full scale clinical images in batch mode. It is well integrated into third-party tools, which increased usability significantly.

The frameworks modular approach following well-established software engineering techniques proved versatile enough to successfully prototype and evaluate a range of algorithms. As part of Chapter 5 we showed additional applications to underpin this capability. This included an approach from related work, namely direct reconstruction with spectral basis functions, which was applied to data obtained with the Biograph mMR [4]. It also included a novel approach to leveraging anatomical regularization, which leveraged an efficient, rotation invariant metric that was combined with anatomical data in a way to effectively address many cases of mismatch between PET and anatomical data.

In addition, we have contributed to works on kinetic modeling for rapid dual-tracer PET [7], Monte-Carlo based system matrix generation for the Biograph mMR [6], a 16-channel coil for simultaneous PET/MR in breast cancer [10], a simulation model for the Biograph mMR Whole-Body PET/MR Scanner[9], and voxel-based analysis of Alzheimer's disease [11].

Within the areas that were covered in this thesis, we perceive a number of open questions and opportunities for future research, most notably:

- The correlation of PET with anatomical images produced by different MR sequences for anatomically guided PET reconstruction is not well understood. If mismatch occurs, it must be handled gracefully by the algorithm. In addition, it is conceivable to leverage anatomical data from multiple sources, e.g., incorporating multiple, different MR sequences into the same PET reconstruction process.

- Anatomically-guided parametric PET images should be validated clinically. Future studies could involve tumor biopsy of patients with surgery. This would allow correlation of voxelwise parametric images with tumor grade and different MR images.

- Improved optimization algorithms and pharmacokinetic models for direct reconstruction are needed. This could include methods to reduce the number of parameters in the pharmacokinetic models to increase stability.

- Image-based input function estimation as needed for many pharmacokinetic models remains challenging. Promising approaches include simultaneous estimation of parameters and input function as well as development of models that do not require input function modeling.

- The positron range correction approach presented in this thesis can be extended to more complex anatomical cases. A good candidate for clinical evaluation would be [^{68}Ga]DOTA-TOC data from patients with neuroendocrine tumors or [^{68}Ga]PSMA data from patients with prostate cancer.

Author's Publications

[1] R. Kraus, G. Delso, and S. Ziegler. Simulation study of tissue-specific positron range correction for the new Biograph mMR whole-body PET/MR system. *IEEE Trans Nucl Sci*, 59(5):1900–1909, Oct 2012.

[2] R. Loeb, N. Navab, and S. Ziegler. Direct parametric reconstruction using anatomical regularization for simultaneous PET/MRI data. *IEEE Trans Med Imaging*, 34(11):2233–2247, Nov 2015.

[3] R. Kraus, G. Delso, X. Cheng, and S. Ziegler. 3D reconstruction with an extended system model for the new Biograph mmr whole-body MR/PET system. *Proceedings of the Annual Meeting of the Society of Nuclear Medicine(SNM 2011)*, 52(suppl. 1):1992, 2011.

[4] R. Kraus, G. Delso, A. Drzezga, S. Nekolla, M. Schwaiger, and S. Ziegler. Fully 4D image reconstruction of simultaneously acquired PET/MR data for [18F]FET. *Proceedings of the Annual Meeting of the Society of Nuclear Medicine(SNM 2012)*, 53(suppl.1):2340, 2012.

[5] R. Kraus, G. Delso, H.-P. Loeb, A. Martinez-Möller, R. Bundschuh, A. Drzezga, and S. Ziegler. An inpainting approach for the correction of incomplete attenuation maps in PET/MR. *Proceedings of the Annual Meeting of the Society of Nuclear Medicine(SNM 2010)*, 51(suppl. 2):1380, 2010.

[6] X. Cheng, G. Delso, R. Kraus, and S. Ziegler. Monte-Carlo based system matrix generation for the Biograph mMR. *Proceedings of the Annual Meeting of the Society of Nuclear Medicine(SNM 2011)*, 52(suppl. 1):1993, 2011.

[7] X. Cheng, K. Shi, R. Kraus, G. Delso, and S. Ziegler. Feasibility study of factor analysis and kinetic modeling for spatial discrimination of rapid dual-tracer PET. *Proceedings of the Annual Meeting of the Society of Nuclear Medicine(SNM 2011)*, 52(suppl. 1):2032, 2011.

[8] G. Delso, R. Kraus, R. Bundschuh, A. Martinez-Möller, S. Nekolla, and S. Ziegler. PET/MR truncation artifact reduction with an active model of the patients arms.

Proceedings of the Annual Meeting of the Society of Nuclear Medicine(SNM 2010), 51(suppl. 2):1379, 2010.

[9] G. Delso, R. Kraus, and S. Ziegler. Prospective study of truncation artifacts in simultaneous whole-body PET/MR. *Proceedings of the World Molecular Imaging Congress(WMIC 2010)*, 2010.

[10] I. Dregely, M. Nimbalkar, M. Mueller, T. Lanz, S. Nekolla, S. Ziegler, R. Kraus, S. Fürst, A. Haase, and M. Schwaiger. A 16-channel coil for simultaneous PET/MR in breast cancer. *Proceedings of the Annual Meeting of the Society of Nuclear Medicine(SNM 2013)*, 54(suppl. 2):483, 2013.

[11] B. von Reutern, B. Gruenecker, D. Scherübl, R. Kraus, and A. Drzezga. Feasibility of voxel-based analysis of amyloid-burden in transgenic mice of Alzheimer's disease. *Proceedings of the Annual Meeting of the Society of Nuclear Medicine(SNM 2011)*, 52(suppl. 1):2050, 2011.

Bibliography

[12] Available online at http://www.bic.mni.mcgill.ca/brainweb/.

[13] Available online at http://www.pmod.com/technologies/index.html.

[14] Collaborative computational project in positron emission tomography and magnetic resonance imaging (CCP-PETMR). https://www.ccppetmr.ac.uk/softwareframework.html. [Online; accessed 11-June-2016].

[15] National Institute of Standards and Technology, Material Composition Database. http://physics.nist.gov/cgi-bin/Star/compos.pl?text.

[16] Simultaneous PET/MR. http://cmictig.cs.ucl.ac.uk/research/ib/pet-mr. [Online; accessed 11-June-2016].

[17] S Agostinelli, J Allisonas, and K Amako. Geant4 — a simulation toolkit. *Nucl Instrum Meth A*, A(506):250–303, 2003.

[18] Sakari Alenius and Ulla Ruotsalainen. Bayesian image reconstruction for emission tomography based on median root prior. *Eur J Nucl Med*, 24(3):258–265, 1997.

[19] Adam Alessio and Lawrence MacDonald. Spatially variant positron range modeling derived from CT for PET image reconstruction. *IEEE Nucl Sci Symp Conf Rec*, pages 3637–3640, 2008.

[20] Andrei Alexandrescu. *Modern C++ design: generic programming and design patterns applied*. Addison-Wesley, 2001.

[21] Kristof Baete, Johan Nuyts, Koen Van Laere, Wim Van Paesschen, Sarah Ceyssens, Liesbet De Ceuninck, Olivier Gheysens, Annemarie Kelles, Jimmy Van den Eynden, Paul Suetens, et al. Evaluation of anatomy based reconstruction for partial volume correction in brain FDG-PET. *NeuroImage*, 23(1):305–317, 2004.

[22] B. Bai, A. Ruangma, R. Laforest, Y.-C. Tai, and R. M. Leahy. Positron range modeling for statistical PET image reconstruction. *IEEE Nucl Sci Symp Conf Rec*, 4:2501–2505, 2003.

[23] Bing Bai, R. Laforest, A. M. Smith, and R. M. Leahy. Evaluation of MAP image reconstruction with positron range modeling for 3D PET. *IEEE Nucl Sci Symp Conf Rec*, 5:2686–2689, 2005.

[24] Bing Bai, Quanzheng Li, and Richard M Leahy. MR Guided PET Iimage Rrecon-struction. *Semin Nucl Med*, 43:30–44, 2013.

[25] Dale L Bailey and Steven R Meikle. A convolution-subtraction scatter correction method for 3D PET. *Phys Med Biol*, 39(3):411, 1994.

[26] Dale L Bailey, David W Townsend, Peter E Valk, and Michael N Maisey. *Positron emission tomography*. Springer, 2005.

[27] F Bataille, C Comtat, S Jan, FC Sureau, and R Trebossen. Brain PET partial-volume compensation using blurred anatomical labels. *IEEE Trans Nucl Sci*, 54(5):1606–1615, 2007.

[28] MA Belzunce and AJ Reader. Time-invariant component-based normalization for a simultaneous PET-MR scanner. *Phys Med Biol*, 61(9):3554, 2016.

[29] M Bentourkia, P Msaki, J Cadorette, and R Lecomte. Assessment of scatter components in high-resolution PET: correction by nonstationary convolution subtraction. *J Nucl Med*, 36(1):121–129, 1995.

[30] Thomas Beyer, David W Townsend, Tony Brun, Paul E Kinahan, Martin Charron, Raymond Roddy, Jeff Jerin, John Young, Larry Byars, and Ronald Nutt. A combined PET/CT scanner for clinical oncology. *J Nucl Med*, 41:1369–1379, 2000.

[31] James M Bieman and Byung-Kyoo Kang. Cohesion and reuse in an object-oriented system. In *ACM SIGSOFT Software Engineering Notes*, volume 20, pages 259–262. ACM, 1995.

[32] Sergey Bochkanov and Vladimir Bystritsky. Alglib, 2013. Available online at http://www.alglib.net/.

[33] A Bousse, S Pedemonte, D Kazantsev, S Ourselin, S Arridge, and BF Hutton. Weighted MRI-Based Bowsher priors for SPECT brain image reconstruction. *IEEE Nucl Sci Symp Conf Rec*, pages 3519–3522, 2010.

[34] Alexandre Bousse, Christos Panagiotou, Kjell Erlandsson, Sebastien Ourselin, Simon Arridge, and Brian F Hutton. Monotonic algorithm for joint entropy-based anatomical priors in parametric PET image reconstruction. *IEEE Nucl Sci Symp Conf Rec*, pages 3918–3924, 2012.

[35] J. Bowsher, L. Yuan, L. Hedlund, T. Turkington, G. Akbani, A. Baeda, W. Kurylo, C. Wheeler, G. Cofer, M. Dewhirst, and G. Johnson. Utilizing MRI information to estimate F18-FDG distributions in rat flank tumors. *IEEE Nucl Sci Symp Conf Rec*, 4:2488–2492, 2004.

[36] James E. Bowsher, David M. DeLong, Timothy G. Turkington, and Ronald J. Jaszczak. Aligning emission tomography and MRI images by optimizing the emission-tomography image reconstruction objective function. *IEEE Trans Nucl Sci*, 53(3):1248–1258, 2006.

[37] David Brasse, Paul E Kinahan, Carole Lartizien, Claude Comtat, Mike Casey, and Christian Michel. Correction methods for random coincidences in fully 3D whole-body PET: impact on data and image quality. *J Nucl Med*, 46(5):859–867, 2005.

[38] A. Buades, B. Coll, and J. M. Morel. A review of image denoising algorithms, with a new one. *Multiscale Model. Simul.*, 4:490–530, 2005.

[39] J. Cal-Gonzalez, J. L. Herraiz, S. Espana, M. Desco, J. J. Vaquero, and J. M. Udias. Positron range effects in high resolution 3D PET imaging. *IEEE Nucl Sci Symp Conf Rec*, pages 2788–2791, 2009.

[40] Richard E Carson. Tracer kinetic modeling in PET. In *Positron Emission Tomography*, pages 127–159. Springer, 2005.

[41] Ciprian Catana, Andre van der Kouwe, Thomas Benner, Christian J Michel, Michael Hamm, Matthias Fenchel, Bruce Fischl, Bruce Rosen, Matthias Schmand, and A Gregory Sorensen. Toward implementing an MRI-based PET attenuation-correction method for neurologic studies on the MR-PET brain prototype. *J Nucl Med*, 51(9):1431–1438, 2010.

[42] C. Champion and C. Le Loirec. Positron follow-up in liquid water: II. Spatial and energetic study for the most important radioisotopes used in PET. *Phys Med Biol*, 52(22):6605–6625, 2007.

[43] Chung Chan, Roger Fulton, David Dagan Feng, and Steven Meikle. Regularized image reconstruction with an anatomically adaptive prior for positron emission tomography. *Phys Med Biol*, 54(24):7379–400, 2009.

[44] Chung Chan, Roger R. Fulton, Robert Barnett, David Dagan Feng, and Steven R. Meikle. Postreconstruction Nonlocal Means Filtering of Whole-Body PET With an Anatomical Prior. *IEEE Trans Med Imaging*, 33(3):636–650, 2014.

[45] Yang Chen, Jianhua Ma, Qianjin Feng, Limin Luo, Pengcheng Shi, and Wufan Chen. Nonlocal Prior Bayesian Tomographic Reconstruction. *J Math Imaging Vis*, 30(2):133–146, 2008.

[46] Jinxiu Cheng-Liao and Jinyi Qi. PET image reconstruction with anatomical edge guided level set prior. *Phys Med Biol*, 56(21):6899–918, 2011.

[47] Simon R Cherry. Recent advances in instrumentation for positron emission tomography. *Nucl Instrum Meth A*, 348(2):577–582, 1994.

[48] Simon R Cherry and Sung-Cheng Huang. Effects of scatter on model parameter estimates in 3D PET studies of the human brain. *IEEE Trans Nucl Sci*, 42(4):1174–1179, 1995.

[49] Simon R Cherry, Steven R Meikle, and E Jcorrection Hoffman. Correction and characterization of scattered events in three-dimensional PET using scanners with retractable septa. *J Nucl Med*, 34(4):671–678, 1993.

[50] Z. H. Cho, J. K. Chan, L. Ericksson, M. Singh, S. Graham, N. S. MacDonald, and Y. Yano. Positron ranges obtained from biomedically important positron-emitting radionuclides. *J Nucl Med*, 16(12):1174–1176, 1975.

[51] Se Y. Chun, Jeffrey A. Fessler, and Yuni K. Dewaraja. Non-local means methods using CT side information for i-131 SPECT image reconstruction. *IEEE Nucl Sci Symp Conf Rec*, pages 3362–3366, 2012.

[52] Se Young Chun, Jeffrey A Fessler, and Yuni K Dewaraja. Post-reconstruction non-local means filtering methods using CT side information for quantitative SPECT. *Phys Med Biol*, 58(17):6225–6240, 2013.

[53] D. L. Collins, A. P. Zijdenbos, V. Kollokian, J. G. Sled, N. J. Kabani, C. J. Holmes, and A. C. Evans. Design and construction of a realistic digital brain phantom. *IEEE Trans Med Imaging*, 17(3):463–468, Jun 1998.

[54] Claude Comtat, Paul E Kinahan, Jeffrey A Fessler, Thomas Beyer, David W Townsend, Michel Defrise, and Christian Michel. Clinically feasible reconstruction of 3D whole-body PET/CT data using blurred anatomical labels. *Phys Med Biol*, 47(1):1–20, Jan 2002.

[55] Bernard D Coombs, Jerzy Szumowski, and William Coshow. Two-point Dixon technique for water-fat signal decomposition with B0 inhomogeneity correction. *Magn. Reson. Med.*, 38(6):884–889, 1997.

[56] V.J. Cunningham and T. Jones. Spectral analysis of dynamic PET studies. *J Cereb Blood Flow Metab*, 13(1):15–23, 1993.

[57] H. Daniel. Shapes of beta-ray spectra. *Rev. Mod. Phys.*, 40:659–672, 1968.

[58] Margaret E Daube-Witherspoon and Gerd Muehllehner. Treatment of axial data in three-dimensional PET. *J Nucl Med*, 28(11):1717–1724, 1987.

[59] A. R. De Pierro. A modified expectation maximization algorithm for penalized likelihood estimation in emission tomography. *IEEE Trans Med Imaging*, 14(1):132–137, 1995.

[60] Michel Defrise and Paul Kinahan. Data acquisition and image reconstruction for 3D PET. In *The Theory and Practice of 3D PET*, pages 11–53. Springer, 1998.

[61] Michel Defrise, Paul E Kinahan, David W Townsend, Christian Michel, Merence Sibomana, and Danny F Newport. Exact and approximate rebinning algorithms for 3-D PET data. *IEEE Trans Med Imaging*, 16(2):145–158, 1997.

[62] Dominique Delbeke. Oncological applications of FDG PET imaging: brain tumors, colorectal cancer lymphoma and melanoma. *J Nucl Med*, 40(4):591–603, 1999.

[63] Gaspar Delso, Sebastian Fürst, Björn Jakoby, Ralf Ladebeck, Carl Ganter, Stephan G. Nekolla, Markus Schwaiger, and Sibylle I. Ziegler. Performance measurements of the Siemens mMR integrated whole-body PET/MR scanner. *J Nucl Med*, 52(12):1914–1922, Dec 2011.

[64] Gaspar Delso and Sibylle Ziegler. PET/MRI system design. *Eur J Nucl Med*, 36:86–92, 2009.

[65] A. P. Dempster, N. M. Laird, and D. B. Rubin. Maximum likelihood from incomplete data via the EM algorithm. *J Roy Stat Soc B*, 39(1):1–38, 1977.

[66] S Derenzo. Precision measurement of annihilation point spread distributions for medically important positron emitters. *Positron Annihilation, R. Fujiwara, Ed. Sendai, Japan: The Japan Institute of Metals*, pages 819–823, 1979.

[67] Stephen E. Derenzo. Mathematical Removal of Positron Range Blurring in High Resolution Tomography. *IEEE Trans Nucl Sci*, 33(1):565–569, 1986.

[68] Antonia Dimitrakopoulou-Strauss, Ludwig G. Strauss, Thomas Heichel, Hua Wu, Cyrill Burger, Ludger Bernd, and Volker Ewerbeck. The Role of Quantitative (18)F-FDG PET Studies for the Differentiation of Malignant and Benign Bone Lesions. *J Nucl Med*, 43(4):510–518, Apr 2002.

[69] W Thomas Dixon. Simple proton spectroscopic imaging. *Radiology*, 153(1):189–194, 1984.

[70] M. J. Ehrhardt, P. Markiewicz, M. Liljeroth, A. Barnes, V. Kolehmainen, J. S. Duncan, L. Pizarro, D. Atkinson, B. F. Hutton, S. Ourselin, K. Thielemans, and S. R.

Arridge. PET Reconstruction with an Anatomical MRI Prior using Parallel Level Sets. *IEEE Trans Med Imaging*, 35(9):2189–2199, 2016.

[71] Kjell Erlandsson, Irene Buvat, P Hendrik Pretorius, Benjamin A Thomas, and Brian F Hutton. A review of partial volume correction techniques for emission tomography and their applications in neurology, cardiology and oncology. *Phys Med Biol*, 57(21):R119–59, 2012.

[72] Dagan Feng, Koon-Pong Wong, Chi-Ming Wu, and Wan-Chi Siu. A technique for extracting physiological parameters and the required input function simultaneously from PET image measurements: theory and simulation study. *IEEE Trans Inform Tech Biomed*, 1(4):243–254, 1997.

[73] Jeff Fessler. Image reconstruction toolbox. http://web.eecs.umich.edu/~fessler/code/. [Online; accessed 11-June-2016].

[74] Jeffrey A Fessler. Penalized weighted least-squares image reconstruction for positron emission tomography. *IEEE Trans Med Imaging*, 13(2):290–300, 1994.

[75] Jeffrey A Fessler, Neal H Clinthorne, and W Leslie Rogers. Regularized emission image reconstruction using imperfect side information. *IEEE Trans Nucl Sci*, 39(5):1464–1471, 1992.

[76] James W Fletcher, Benjamin Djulbegovic, Heloisa P Soares, Barry A Siegel, Val J Lowe, Gary H Lyman, R Edward Coleman, Richard Wahl, John Christopher Paschold, Norbert Avril, et al. Recommendations on the use of 18F-FDG PET in oncology. *J Nucl Med*, 49(3):480–508, 2008.

[77] Joanna S Fowler and Tatsuo Ido. Initial and subsequent approach for the synthesis of 18 fdg. In *Semin Nucl Med*, volume 32, pages 6–12. Elsevier, 2002.

[78] John V Frangioni. New technologies for human cancer imaging. *J Clin Oncol*, 26(24):4012–4021, 2008.

[79] Edward K Fung and Richard E Carson. Cerebral blood flow with [15O] water PET studies using an image-derived input function and MR-defined carotid centerlines. *Phys Med Biol*, 58(6):1903, 2013.

[80] Norbert Galldiks, Roland Ullrich, Michael Schroeter, Gereon R Fink, and Lutz W Kracht. Volumetry of [11C]-methionine PET uptake and MRI contrast enhancement in patients with recurrent glioblastoma multiforme. *Eur J Nucl Med*, 37(1):84–92, 2010.

[81] Erich Gamma, Richard Helm, Ralph Johnson, and John Vlissides. *Design patterns: Abstraction and reuse of object-oriented design*. Springer, 1993.

[82] GEANT4. GEANT4 User's Guide for Application Developers. http://geant4.web.cern.ch/geant4/UserDocumentation/UsersGuides/ForApplicationDeveloper/html/index.html.

[83] S. Geman and D. McClure. Bayesian image analysis: An application to single photon emission tomography. *Proc Stat Comput Sect Am Stat Assoc*, pages 12–18, 1985.

[84] Gene Gindi, Mindy Lee, Anand Rangarajan, and I George Zubal. Bayesian reconstruction of functional images using anatomical information as priors. *IEEE Trans Med Imaging*, 12(4):670–680, 1993.

[85] Alexander M Grant, Timothy W Deller, Mohammad Mehdi Khalighi, Sri Harsha Maramraju, Gaspar Delso, and Craig S Levin. NEMA NU 2-2012 performance studies for the SiPM-based ToF-PET component of the GE SIGNA PET/MR system. *Med Phys*, 43(5):2334–2343, 2016.

[86] Peter J Green. Bayesian reconstructions from emission tomography data using a modified EM algorithm. *IEEE Trans Med Imaging*, 9(1):84–93, 1990.

[87] S Grootoonk, TJ Spinks, D Sashin, NM Spyrou, and T Jones. Correction for scatter in 3D brain PET using a dual energy window method. *Phys Med Biol*, 41(12):2757–2774, 1996.

[88] Julio Brandao Guimaraes, Leticia Rigo, Fabio Lewin, and Andre Emerick. The importance of PET/CT in the evaluation of patients with Ewing tumors. *Radiologia Brasileira*, 48:175–180, 06 2015.

[89] B. Gurin, S. Cho, S. Y. Chun, X. Zhu, N. M. Alpert, and G. El Fakhri. Nonrigid PET motion compensation in the lower abdomen using simultaneous tagged-MRI and PET imaging. *Med Phys*, 38(6):3025–3038, 2011.

[90] S. F. Haber, S. E. Derenzo, and D. Uber. Application of mathematical removal of positron range blurring in positron emission tomography. *IEEE Trans Nucl Sci*, 37(3):1293–1299, 1990.

[91] B E Hammer, N L Christensen, and B G Heil. Use of a magnetic field to increase the spatial resolution of positron emission tomography. *Med Phys*, 21:1917–1920, 1994.

[92] R. L. Harrison, M. S. Kaplan, S. D. Vannoy, and T. K. Lewellen. Positron range and coincidence non-collinearity in SimSET. *IEEE Nucl Sci Symp Conf Rec*, 3:1265–1268, 1999.

[93] H. Herzog, H. Iida, C. Weirich, L. Tellmann, J. Kaffanke, S. Spellerberg, L. Caldeira, E. R. Kops, and N. J. Shah. Influence from high and ultra-high magnetic field on

positron range measured with a 9.4TMR-BrainPET. *IEEE Nucl Sci Symp Conf Rec*, pages 3410–3413, 2010.

[94] Matthias Hofmann, Ilja Bezrukov, Frederic Mantlik, Philip Aschoff, Florian Steinke, Thomas Beyer, Bernd J Pichler, and Bernhard Schölkopf. MRI-based attenuation correction for whole-body PET/MRI: quantitative evaluation of segmentation-and atlas-based methods. *J Nucl Med*, 52(9):1392–1399, 2011.

[95] Walter L Hürsch and Cristina Videira Lopes. Separation of concerns. 1995.

[96] Sun-Kyoo Hwang and Whoi-Yul Kim. A novel approach to the fast computation of zernike moments. *Pattern Recognition*, 39(11):2065–2076, 2006.

[97] ICRP, International Commission on Radiological Protection. *Reference man: anatomical, physiological and metabolic characteristics*. ICRP Publication 23, New York, 1975.

[98] H. Iida, I. Kanno, S. Miura, M. Murakami, K. Takahashi, and K. Uemura. A Simulation Study of a Method to Reduce Positron Annihilation Spread Distributions Using a Strong Magnetic Field in Positron Emission Tomography. *IEEE Trans Nucl Sci*, 33(1):597–600, 1986.

[99] A Iriarte, R Marabini, S Matej, COS Sorzano, and RM Lewitt. System models for PET statistical iterative reconstruction: A review. *Comput Med Imaging Graph*, 48:30–48, 2016.

[100] Ivar Jacobson, Martin Griss, and Patrik Jonsson. *Software reuse: architecture, process and organization for business success*. ACM Press/Addison-Wesley Publishing Co., 1997.

[101] S. Jan, G. Santin, D. Strul, S. Staelens, K. Assie, and et al. Gate: a simulation toolkit for PET and SPECT. *Phys Med Biol*, 49:4543–4561, 2004.

[102] Thies H Jochimsen, Vilia Zeisig, Jessica Schulz, Peter Werner, Marianne Patt, Jörg Patt, Antje Y Dreyer, Johannes Boltze, Henryk Barthel, Osama Sabri, et al. Fully automated calculation of image-derived input function in simultaneous PET/MRI in a sheep model. *EJNMMI physics*, 3:2, 2016.

[103] Dan J Kadrmas and M Bugrahan Oktay. Generalized separable parameter space techniques for fitting 1K-5K serial compartment models. *Med Phys*, 40(7):072502, 2013.

[104] M. E. Kamasak, C. A. Bouman, E. D. Morris, and K. Sauer. Direct reconstruction of kinetic parameter images from dynamic PET data. *IEEE Trans Med Imaging*, 24(5):636–650, May 2005.

[105] Mustafa E Kamasak, Bradley T Christian, Charles A Bouman, and Evan D Morris. Quality and precision of parametric images created from PET sinogram data by direct reconstruction: proof of concept. *IEEE Trans Med Imaging*, 33(3):695–707, 2014.

[106] Daniil Kazantsev, Simon R Arridge, Stefano Pedemonte, Alexandre Bousse, Kjell Erlandsson, Brian F Hutton, and Sébastien Ourselin. An anatomically driven anisotropic diffusion filtering method for 3D SPECT reconstruction. *Phys Med Biol*, 57(12):3793, 2012.

[107] Daniil Kazantsev, Alexandre Bousse, Stefano Pedemonte, Simon R. Arridge, Brian F. Hutton, and Sébastien Ourselin. Edge preserving bowsher prior with nonlocal weighting for 3D spect reconstruction. *IEEE Nucl Sci Symp Conf Rec*, pages 1158–1161, 2011.

[108] Daniil Kazantsev, Sébastien Ourselin, Brian F Hutton, Katherine J Dobson, Anders P Kaestner, William RB Lionheart, Philip J Withers, Peter D Lee, and Simon R Arridge. A novel technique to incorporate structural prior information into multi-modal tomographic reconstruction. *Inverse Problems*, 30(6):065004, 2014.

[109] Vincent Keereman, Yves Fierens, Tom Broux, Yves De Deene, Max Lonneux, and Stefaan Vandenberghe. MRI-based attenuation correction for PET/MRI using ultrashort echo time sequences. *J Nucl Med*, 51(5):812–818, 2010.

[110] Paul E Kinahan, Bruce H Hasegawa, and Thomas Beyer. X-ray-based attenuation correction for positron emission tomography/computed tomography scanners. In *Semin Nucl Med*, volume 33, pages 166–179. Elsevier, 2003.

[111] A. Kolb, M. Hofmann, A. Sauter, C.-C Liu, L. Eriksson, and B. Pichler. Inhomogeneous Positron Range Effects in High Magnetic Fields might Cause Severe Artefacts in PET/MRI. *WMIC*, 2010.

[112] Elena Rota Kops and Hans Herzog. Alternative methods for attenuation correction for PET images in MR-PET scanners. *IEEE Nucl Sci Symp Conf Rec*, 6:4327–4330, 2007.

[113] Kenneth Lange, David R Hunter, and Ilsoon Yang. Optimization transfer using surrogate objective functions. *J Comput Graph Statist*, 9(1):1–20, 2000.

[114] Paul Lecoq. Development of new scintillators for medical applications. *Nucl Instrum Meth A*, 809:130–139, 2016.

[115] C. S. Levin and E. J. Hoffman. Calculation of Positron Range and its Effect on Positron Emission Tomography System Spatial Resolution. *Phys Med Biol*, 44(3):781–799, 1999.

[116] B. Lipinski, H. Herzog, E. Rota Kops, W. Oberschelp, and H. W. Müller-Gärtner. Expectation maximization reconstruction of positron emission tomography images using anatomical magnetic resonance information. *IEEE Trans Med Imaging*, 16(2):129–136, 1997.

[117] C.-C. Liu, M. Judenhofer, A. Kolb, and B. J. Pichler. The observation and correction of positron range for PET-Insert scanner. *IEEE Nucl Sci Symp Conf Rec*, 2010.

[118] Andreas Markus Loening, Sanjiv Sam Gambhir, et al. AMIDE: a free software tool for multimodality medical image analysis. *Molecular imaging*, 2(3):131–137, 2003.

[119] Lijun Lu, Nicolas A Karakatsanis, Jing Tang, Wufan Chen, and Arman Rahmim. 3.5D dynamic PET image reconstruction incorporating kinetics-based clusters. *Phys Med Biol*, 57(15):5035–5055, 2012.

[120] Lijun Lu, Jianhua Ma, Qianjin Feng, Wufan Chen, and Arman Rahmim. Anatomy-guided brain PET imaging incorporating a joint prior model. *Phys Med Biol*, 60(6):2145–2166, 2015.

[121] A. Martinez-Möller, M. Souvatzoglou, G. Delso, R. A. Bundschuh, C. Chefd'hotel, S. Ziegler, N. Navab, M. Schwaiger, and S. Nekolla. Tissue Classification as a Potential Approach for Attenuation Correction in Whole-Body PET/MRI: Evaluation with PET/CT Data. *J Nucl Med*, 50(4):520–526, Apr 2009.

[122] Aswin John Mathews. A four-dimensional image reconstruction framework for PET under arbitrary geometries. 2014.

[123] J. Matthews, D. Bailey, P. Price, and V. Cunningham. The direct calculation of parametric images from dynamic PET data using maximum-likelihood iterative reconstruction. *Phys Med Biol*, 42(6):1155–73, 1997.

[124] J. C. Matthews, G. I. Angelis, F. A. Kotasidis, P. J. Markiewicz, and A. J. Reader. Direct reconstruction of parametric images using any spatiotemporal 4D image based model and maximum likelihood expectation maximisation. *IEEE Nucl Sci Symp Conf Rec*, pages 2435–2441, 2010.

[125] Bjoern Menze, Andras Jakab, Stefan Bauer, Jayashree Kalpathy-Cramer, Keyvan Farahani, Justin Kirby, Yuliya Burren, Nicole Porz, Johannes S lotboom, Roland Wiest, Levente Lanczi, Elisabeth Gerstner, Marc-Andre Weber, Tal Arbel, Brian Avants, Nicholas Ayache, Patricia Buendia, Louis Collins, Nicolas Cordier, Jason Corso, Antonio Criminisi, Tilak Das, Hervé Delingette, Cagatay Demiralp, Christopher Durst, Michel Dojat, Senan Doyle, Joana Festa, Florence Forbes, Ezequiel Geremia, Ben Glocker, Polina Golland, Xiaotao Guo, Andac Hamamci, Khan

Iftekharuddin, Raj Jena, Nigel John, Ender Konukoglu, Danial Lashkari, Jose Antonio Mariz, Raphael Meier, Sergio Pereira, Doina Precup, S. J. Price, Tammy Riklin-Raviv, Syed Reza, Michael Ryan, Lawrence Schwartz, Hoo-Chang Shin, Jamie Shotton, Carlos Silva, Nuno Sousa, Nagesh Subbanna, Gabor Szekely, Thomas Taylor, Owen Thomas, Nicholas Tustison, Gozde Unal, Flor Vasseur, Max Wintermark, Dong Hye Ye, Liang Zhao, Binsheng Zhao, Darko Zikic, Marcel Prastawa, Mauricio Reyes, and Koen Van Leemput. The Multimodal Brain Tumor Image Segmentation Benchmark (BRATS). *IEEE Trans Med Imag*, 34(10):1993–2024, Oct 2015.

[126] William W Moses. Fundamental limits of spatial resolution in PET. *Nucl Instrum Meth A*, 648:S236–S240, 2011.

[127] Erkan Ü Mumcuoglu, Richard M Leahy, and Simon R Cherry. Bayesian reconstruction of PET images: methodology and performance analysis. *Phys Med Biol*, 41(9):1777–807, 1996.

[128] NEMA Standards Publication NU 2-2007. *Performance Measurements of Positron Emission Tomographs*. National Electrical Manufacturers Association, Rosslyn, VA, 2007.

[129] Van-Giang Nguyen and Soo-Jin Lee. Incorporating Anatomical Side Information Into PET Reconstruction Using Nonlocal Regularization. *IEEE Trans Image Process*, 22(10):3961–3973, 2013.

[130] Thomas E Nichols, Jinyi Qi, Evren Asma, and Richard M Leahy. Spatiotemporal reconstruction of list-mode PET data. *IEEE Trans Med Imaging*, 21(4):396–404, 2002.

[131] Agneta Nordberg, Juha O Rinne, Ahmadul Kadir, and Bengt Långström. The use of PET in Alzheimer disease. *Nat Rev Neurol*, 6(2):78–87, 2010.

[132] J. Nuyts. The use of mutual information and joint entropy for anatomical priors in emission tomography. *IEEE Nucl Sci Symp Conf Rec*, 6:4149–4154, 2007.

[133] Johan Nuyts, Patrick Dupont, Sigrid Stroobants, Roel Benninck, Luc Mortelmans, and Paul Suetens. Simultaneous maximum a posteriori reconstruction of attenuation and activity distributions from emission sinograms. *IEEE Trans Med Imaging*, 18(5):393–403, 1999.

[134] Xiaolong Ouyang, Wing Hung Wong, Valen E Johnson, Xiaoping Hu, and Chin-Tu Chen. Incorporation of correlated structural images in PET image reconstruction. *IEEE Trans Med Imaging*, 13(4):627–640, 1994.

[135] Tinsu Pan and Osama Mawlawi. PET/CT in radiation oncology. *Med Phys*, 35(11):4955–4966, 2008.

[136] M. E. Phelps, E. J. Hoffman, and M. M. Ter-Pogossian S. C. Huang. Effect of positron range on spatial resolution. *J Nucl Med*, 16:649–52, 1975.

[137] M.E. Phelps. *PET: Physics, Instrumentation, and Scanners.* Springer New York, 2006.

[138] Bernd J Pichler, Armin Kolb, Thomas Ngele, and Heinz-Peter Schlemmer. PET/MRI: Paving the Way for the Next Generation of Clinical Multimodality Imaging Applications. *J Nucl Med*, 51(3):333–336, 2010.

[139] Bernd J Pichler, Hans F Wehrl, Armin Kolb, and Martin S Judenhofer. Positron emission tomography/magnetic resonance imaging: the next generation of multimodality imaging? *Semin Nucl Med*, 38(3):199–208, 2008.

[140] G. Pöpperl, F.W. Kreth, J.H. Mehrkens, J. Herms, K. Seelos, W. Koch, F.J. Gildehaus, H.A. Kretzschmar, J.C. Tonn, and K. Tatsch. FET PET for the evaluation of untreated gliomas: correlation of FET uptake and uptake kinetics with tumour grading. *Eur J Nucl Med*, 34(12):1933–1942, 2007.

[141] Arman Rahmim. Advanced motion correction methods in PET. *Iran J Nucl Med*, 13(2):1–17, 2005.

[142] Arman Rahmim, Jinyi Qi, and Vesna Sossi. Resolution modeling in PET imaging: theory, practice, benefits, and pitfalls. *Med Phys*, 40(6):064301, 2013.

[143] Arman Rahmim, Jing Tang, and Habib Zaidi. Four-dimensional (4D) image reconstruction strategies in dynamic PET: beyond conventional independent frame reconstruction. *Med Phys*, 36(8):3654–3670, Aug 2009.

[144] Arman Rahmim, Yun Zhou, Jing Tang, Lijun Lu, Vesna Sossi, and Dean F Wong. Direct 4D parametric imaging for linearized models of reversibly binding PET tracers using generalized AB-EM reconstruction. *Phys Med Biol*, 57(3):733–55, 2012.

[145] R. R. Raylman, B. E. Hammer, and N. L. Christensen. Combined MRI-PET Scanner: A Monte Carlo Evaluation of the Improvements in PET Resolution Due to the Effects of a Static Homogeneous Magnetic Field. *IEEE Trans Nucl Sci*, 43(4):2406–2412, 1996.

[146] A. J. Reader, J. C. Matthews, F. C. Sureau, C. Comtat, R. Trebossen, and I. Buvat. Fully 4D image reconstruction by estimation of an input function and spectral coefficients. *IEEE Nucl Sci Symp Conf Rec*, 5:3260–3267, 2007.

[147] A.J. Reader, J.C. Matthews, F.C. Sureau, C. Comtat, R. Trebossen, and I. Buvat. Iterative kinetic parameter estimation within fully 4D PET image reconstruction. *IEEE Nucl Sci Symp Conf Rec*, 3:1752–1756, 2006.

[148] Bryan W Reutter, Grant T Gullberg, and Ronald H Huesman. Direct least-squares estimation of spatiotemporal distributions from dynamic SPECT projections using a spatial segmentation and temporal B-splines. *IEEE Trans Med Imaging*, 19(5):434–450, 2000.

[149] Bryan W Reutter, Grant T Gullberg, and Ronald H Huesman. Effects of temporal modelling on the statistical uncertainty of spatiotemporal distributions estimated directly from dynamic SPECT projections. *Phys Med Biol*, 47(15):2673–83, 2002.

[150] Marie Anne Richard, Jérémie P Fouquet, Réjean Lebel, and Martin Lepage. MRI-guided derivation of the input function for PET kinetic modeling. *PET clinics*, 11(2):193–202, 2016.

[151] Eric M Rohren, Timothy G Turkington, and R Edward Coleman. Clinical applications of PET in oncology 1. *Radiology*, 231(2):305–332, 2004.

[152] André Salomon, Andreas Goedicke, Bernd Schweizer, Til Aach, and Volkmar Schulz. Simultaneous reconstruction of activity and attenuation for PET/MR. *IEEE Trans Med Imaging*, 30(3):804–813, 2011.

[153] Arend FL Schinkel, Don Poldermans, Abdou Elhendy, and Jeroen J Bax. Assessment of myocardial viability in patients with heart failure. *J Nucl Med*, 48(7):1135–1146, 2007.

[154] V Schulz, I Torres-Espallardo, S Renisch, Z Hu, N Ojha, P Börnert, M Perkuhn, T Niendorf, WM Schäfer, H Brockmann, et al. Automatic, three-segment, MR-based attenuation correction for whole-body PET/MR data. *Eur J Nucl Med*, 38(1):138–152, 2011.

[155] Markus Schwaiger. Myocardial perfusion imaging with PET. *J Nucl Med*, 35(4):693–698, 1994.

[156] L.A. Shepp and Y Vardi. Maximum likelihood reconstruction in PET. *IEEE Trans Med Imaging*, 1(2):113–122, 1982.

[157] Lawrence A Shepp and Benjamin F Logan. The Fourier reconstruction of a head section. *IEEE Trans Nucl Sci*, 21(3):21–43, 1974.

[158] Robert L Siddon. Fast calculation of the exact radiological path for a three-dimensional CT array. *Med Phys*, 12(2):252–255, 1985.

[159] Alejandro Snchez-Crespo, Pedro Andreo, and Stig A Larsson. Positron flight in human tissues and its influence on PET image spatial resolution. *Eur J Nucl Med*, 31(1):44–51, 2004.

[160] Donald L. Snyder, Michael I. Miller, Lewis J. Thomas, and David G. Politte. Noise and Edge Artifacts in Maximum-Likelihood Reconstructions for Emission Tomography. *IEEE Trans Med Imaging*, 6(3):228–238, 1987.

[161] Sangeetha Somayajula, Evren Asma, and Richard M Leahy. PET image reconstruction using anatomical information through mutual information based priors. *IEEE Nucl Sci Symp Conf Rec*, 5:2722–2726, 2005.

[162] Sangeetha Somayajula, Christos Panagiotou, Anand Rangarajan, Quanzheng Li, Simon R Arridge, and Richard M Leahy. PET image reconstruction using information theoretic anatomical priors. *IEEE Trans Med Imaging*, 30(3):537–549, 2011.

[163] G Soultanidis, N Karakatsanis, G Nikiforidis, and G Loudos. Study of the effect of magnetic field in positron range using GATE simulation toolkit. *Journal of Physics: Conference Series*, 317(1):012021, 2011.

[164] Yi Su, Ana M Arbelaez, Tammie LS Benzinger, Abraham Z Snyder, Andrei G Vlassenko, Mark A Mintun, and Marcus E Raichle. Noninvasive estimation of the arterial input function in positron emission tomography imaging of cerebral blood flow. *J Cereb Blood Flow Metab*, 33(1):115–121, 2013.

[165] F.C Sureau, A.J. Reader, C. Comtat, C. Leroy, M.J. Ribeiro, I. Buvat, and R. Trbossen. Impact of image-space resolution modeling for studies with the high-resolution research tomograph. *J Nucl Med*, 49(6):1000–1008, 2008.

[166] YF Tai and P Piccini. Applications of positron emission tomography (pet) in neurology. *J Neurol Neurosurg Psychiatry*, 75(5):669–676, 2004.

[167] Mustafa Takesh. The potential benefit by application of kinetic analysis of PET in the clinical oncology. *ISRN Oncol*, 2012, 2012.

[168] Jing Tang, Hiroto Kuwabara, Dean F Wong, and Arman Rahmim. Direct 4D reconstruction of parametric images incorporating anato-functional joint entropy. *Phys Med Biol*, 55(15):4261–4272, Aug 2010.

[169] Jing Tang and A. Rahmim. Anatomy assisted MAP-EM PET image reconstruction incorporating joint entropies of wavelet subband image pairs. *IEEE Nucl Sci Symp Conf Rec*, pages 3741–3745, 2009.

[170] Jing Tang and Arman Rahmim. Bayesian PET image reconstruction incorporating anato-functional joint entropy. *Phys Med Biol*, 54(23):7063–7075, Dec 2009.

[171] Jing Tang and Arman Rahmim. Anatomy assisted PET image reconstruction incorporating multi-resolution joint entropy. *Phys Med Biol*, 60(1):31–48, 2015.

[172] Kris Thielemans, Charalampos Tsoumpas, Sanida Mustafovic, Tobias Beisel, Pablo Aguiar, Nikolaos Dikaios, and Matthew W Jacobson. STIR: software for tomographic image reconstruction release 2. *Phys Med Biol*, 57(4):867–83, 2012.

[173] David W Townsend, Jonathan PJ Carney, Jeffrey T Yap, and Nathan C Hall. PET/CT today and tomorrow. *J Nucl Med*, 45(1 suppl):4S–14S, 2004.

[174] C. Tsoumpas, J.E. Mackewn, P. Halsted, A.P. King, C. Buerger, J.J. Totman, T. Schaeffter, and P.K. Marsden. Simultaneous PETMR acquisition and MR-derived motion fields for correction of non-rigid motion in PET. *Ann Nucl Med*, 24:745–750, 2010.

[175] Charalampos Tsoumpas, Federico E Turkheimer, and Kris Thielemans. Study of direct and indirect parametric estimation methods of linear models in dynamic positron emission tomography. *Med Phys*, 35(4):1299–1309, April 2008.

[176] Charalampos Tsoumpas, Federico E. Turkheimer, and Kris Thielemans. A survey of approaches for direct parametric image reconstruction in emission tomography. *Med Phys*, 35(9):3963–3971, Sep 2008.

[177] MG Ullisch, J Scheins, C Weirich, E Rota Kops, A Celik, L Tellmann, T Stöcker, H Herzog, and NJ Shah. MR-guided data framing for PET motion correction in simultaneous MR–PET: A preliminary evaluation. *Nucl Instrum Meth A*, 702:67–69, 2013.

[178] Dominique Van de Sompel and Michael Brady. Regularising limited view tomography using anatomical reference images and information theoretic similarity metrics. *Med Image Anal*, 16(1):278–300, 2012.

[179] Stefaan Vandenberghe and Paul K Marsden. PET-MRI: a review of challenges and solutions in the development of integrated multimodality imaging. *Phys Med Biol*, 60(4):R115–54, 2015.

[180] J. Verhaeghe, Y. DAsseler, S. Vandenberghe, S. Staelens, and I. Lemahieu. An investigation of temporal regularization techniques for dynamic PET reconstructions using temporal splines. *Med Phys*, 34(5):1766–1778, 2007.

[181] J. Verhaeghe, D. Van De Ville, I. Khalidov, Y. D'Asseler, I. Lemahieu, and M. Unser. Dynamic PET Reconstruction Using Wavelet Regularization With Adapted Basis Functions. *IEEE Trans Med Imaging*, 27(7):943–959, 2008.

[182] Kathleen Vunckx, Ameya Atre, Kristof Baete, Anthonin Reilhac, Christophe M Deroose, Koen Van Laere, and Johan Nuyts. Evaluation of three MRI-based anatomical priors for quantitative PET brain imaging. *IEEE Trans Med Imaging*, 31(3):599–612, 2012.

[183] Gudrun Wagenknecht, Hans-Jürgen Kaiser, Felix M Mottaghy, and Hans Herzog. MRI for attenuation correction in PET: methods and challenges. *MAGMA*, 26(1):99–113, 2013.

[184] Guobao Wang, Lin Fu, and Jinyi Qi. Maximum a posteriori reconstruction of the Patlak parametric image from sinograms in dynamic PET. *Phys Med Biol*, 53(3):593–604, Feb 2008.

[185] Guobao Wang and Jinyi Qi. Generalized Algorithms for Direct Reconstruction of Parametric Images From Dynamic PET Data. *IEEE Trans Med Imaging*, 28(11):1717–1726, 2009.

[186] Guobao Wang and Jinyi Qi. Acceleration of the direct reconstruction of linear parametric images using nested algorithms. *Phys Med Biol*, 55(5):1505–1517, March 2010.

[187] Guobao Wang and Jinyi Qi. An Optimization Transfer Algorithm for Nonlinear Parametric Image Reconstruction From Dynamic PET data. *IEEE Trans Med Imaging*, 31(10):1977–1988, 2012.

[188] Guobao Wang and Jinyi Qi. Direct Estimation of Kinetic Parametric Images for Dynamic PET. *Theranostics*, 3(10):802–815, 2013.

[189] Guobao Wang and Jinyi Qi. PET image reconstruction using kernel method. *IEEE Trans Med Imaging*, 34(1):61–71, 2015.

[190] Otto Warburg. Über den Stoffwechsel der Carcinomzelle. *Naturwissenschaften*, 12(50):1131–1137, 1924.

[191] Otto Warburg et al. On the origin of cancer cells. *Science*, 123(3191):309–314, 1956.

[192] Charles C Watson. New, faster, image-based scatter correction for 3D PET. *IEEE Trans Nucl Sci*, 47(4):1587–1594, 2000.

[193] Charles C Watson, DMEC Newport, and Mike E Casey. A single scatter simulation technique for scatter correction in 3D PET. In *Three-dimensional image reconstruction in radiology and nuclear medicine*, pages 255–268. Springer, 1996.

[194] Hans F Wehrl, Alexander W Sauter, Mathew R Divine, and Bernd J Pichler. Combined PET/MR: a technology becomes mature. *J Nucl Med*, 56(2):165–168, 2015.

[195] Ralph Weissleder. Molecular imaging in cancer. *Science*, 312(5777):1168–1171, 2006.

[196] M. N. Wernick, E. J. Infusino, and M. Milosevic. Fast spatio-temporal image reconstruction for dynamic PET. *IEEE Trans Med Imaging*, 18(3):185–195, 1999.

[197] A. Wirrwar, H. Vosberg, H. Herzog, H. Halling, S. Weber, and H.-W. Muller-Gartner. 4.5 Tesla magnetic field reduces range of high-energy positrons - Potential implications for positron emission tomography. *IEEE Trans Nucl Sci*, 44(2):184–189, 1997.

[198] Isaac Yang and Manish K. Aghi. New advances that enable identification of glioblastoma recurrence. *Nat Rev Clin Oncol*, 6(11):648–657, Nov 2009.

[199] Terry S Yoo, Michael J Ackerman, William E Lorensen, Will Schroeder, Vikram Chalana, Stephen Aylward, Dimitris Metaxas, and Ross Whitaker. Engineering and algorithm design for an image processing API: a technical report on ITK-the insight toolkit. *Studies in health technology and informatics*, pages 586–592, 2002.

[200] Habib Zaidi and Minerva Becker. The Promise of Hybrid PET/MRI: Technical advances and clinical applications. *IEEE Signal Proc Mag*, 33(3):67–85, 2016.

[201] Habib Zaidi, Osama Mawlawi, and Colin G Orton. Point/counterpoint. Simultaneous PET/MR will replace PET/CT as the molecular multimodality imaging platform of choice. *Med Phys*, 34:1525–1528, 2007.

[202] Paolo Zanotti-Fregonara, Kewei Chen, Jeih-San Liow, Masahiro Fujita, and Robert B Innis. Image-derived input function for brain PET studies: many challenges and few opportunities. *J Cereb Blood Flow Metab*, 31(10):1986–1998, 2011.

[203] Pat Zanzonico. Positron emission tomography: a review of basic principles, scanner design and performance, and current systems. *Semin Nucl Med*, 34(2):87–111, Apr 2004.